

University of Kentucky

UKnowledge

Theses and Dissertations--Chemistry

Chemistry


2020

DESIGNING METAL-HALIDE PEROVSKITES WITH ENHANCED OPTICAL PROPERTIES AND STABILITY USING SURFACE LIGANDS

Md Aslam Uddin

University of Kentucky, md.uddin_chem@uky.edu

Author ORCID Identifier:

 <https://orcid.org/0000-0002-9780-2864>

Digital Object Identifier: <https://doi.org/10.13023/etd.2020.481>

[Right click to open a feedback form in a new tab to let us know how this document benefits you.](#)

Recommended Citation

Uddin, Md Aslam, "DESIGNING METAL-HALIDE PEROVSKITES WITH ENHANCED OPTICAL PROPERTIES AND STABILITY USING SURFACE LIGANDS" (2020). *Theses and Dissertations--Chemistry*. 133. https://uknowledge.uky.edu/chemistry_etds/133

This Doctoral Dissertation is brought to you for free and open access by the Chemistry at UKnowledge. It has been accepted for inclusion in Theses and Dissertations--Chemistry by an authorized administrator of UKnowledge. For more information, please contact UKnowledge@lsv.uky.edu.

STUDENT AGREEMENT:

I represent that my thesis or dissertation and abstract are my original work. Proper attribution has been given to all outside sources. I understand that I am solely responsible for obtaining any needed copyright permissions. I have obtained needed written permission statement(s) from the owner(s) of each third-party copyrighted matter to be included in my work, allowing electronic distribution (if such use is not permitted by the fair use doctrine) which will be submitted to UKnowledge as Additional File.

I hereby grant to The University of Kentucky and its agents the irrevocable, non-exclusive, and royalty-free license to archive and make accessible my work in whole or in part in all forms of media, now or hereafter known. I agree that the document mentioned above may be made available immediately for worldwide access unless an embargo applies.

I retain all other ownership rights to the copyright of my work. I also retain the right to use in future works (such as articles or books) all or part of my work. I understand that I am free to register the copyright to my work.

REVIEW, APPROVAL AND ACCEPTANCE

The document mentioned above has been reviewed and accepted by the student's advisor, on behalf of the advisory committee, and by the Director of Graduate Studies (DGS), on behalf of the program; we verify that this is the final, approved version of the student's thesis including all changes required by the advisory committee. The undersigned agree to abide by the statements above.

Md Aslam Uddin, Student

Dr. Kenneth R. Graham, Major Professor

Dr. Yinan Wei, Director of Graduate Studies

DESIGNING METAL-HALIDE PEROVSKITES WITH ENHANCED OPTICAL
PROPERTIES AND STABILITY USING SURFACE LIGANDS

DISSERTATION

A dissertation submitted in partial fulfillment of the
requirements for the degree of Doctor of Philosophy in the College of Arts and Sciences
at the University of Kentucky

By
Md Aslam Uddin
Lexington, Kentucky
Director: Dr. Kenneth R. Graham, Professor of Chemistry
Lexington, Kentucky
2020

Copyright © Md Aslam Uddin 2020
<https://orcid.org/0000-0002-9780-2864>

ABSTRACT OF DISSERTATION

DESIGNING METAL-HALIDE PEROVSKITES WITH ENHANCED OPTICAL PROPERTIES AND STABILITY USING SURFACE LIGANDS

Metal-halide perovskites (MHPs), with formula ABX_3 ($A = \text{methylammonium}$, formamidinium , or Cs^+ ; $B = \text{Sn}^{2+}$ or Pb^{2+} ; and $X = \text{Cl}^-$, Br^- , or I^-) are versatile and attractive materials because of their tunable optical and electronic properties. These optical and electronic properties include tunable direct band gaps, high absorption coefficients, low exciton binding energies, relatively high electron and hole mobilities, narrow emission line-widths, and high photoluminescence (PL) quantum yields (Φ_{PL}). Much of the initial excitement around organic metal-halide perovskites focused on their application in photovoltaics (PVs) based on thin polycrystalline films, whereas colloidal metal-halide perovskite nanocrystals (NCs) are now a subject of intense interest due to their highly desirable emission properties and low rate of non-radiative recombination for light emitting applications. However, both polycrystalline MHP thin films and their NC counterparts suffer from poor stability and are highly moisture sensitive. In this thesis, facile and rapid anion exchange and surface modification routes of MHP NCs are discussed using alkyltrichlorosilane, alkanethiols, and alkanethiol-aluminum trihalide combinations. In addition, similar approaches are employed to modify solution processed MHP thin films for fabricating efficient and stable photovoltaic devices.

Rapid anion exchange and surface modification reactions with MHP NCs readily proceed via coupling and/or hydrolysis reactions of the surface ligands at room temperature. Both NCs, thin films, and thin film-based PV devices demonstrate significantly enhanced performance and stability upon surface modification. It is shown that alkyltrichlorosilanes (RSiCl_3) can be used as Cl^- sources for rapid anion exchange with host CsPbBr_3 NCs during hydrolysis of alkyltrichlorosilanes in the colloidal dispersion of CsPbBr_3 NCs. Hydrolysis of alkyltrichlorosilanes leads to the formation of siloxane coated CsPbCl_3 NCs with significantly improved Φ_{PL} of up to 12% and improved long-term stability. In another study of surface modification, dodecanethiol modification of CsPbBr_3 NCs is demonstrated to significantly enhance the stability and Φ_{PL} of CsPbBr_3 NCs, with Φ_{PL} of near 100%. This surface modification can be expedited through exposure to UV light, which also induces thiol-ene reactions. A mixture of dodecanethiol (DDT) and AlX_3 ($X = \text{Cl}$, Br , I) can be used to increase the applicability of alkanethiol treatment to all NC compositions. Here, DDT and AlX_3 ($X = \text{Cl}$, Br , I) treatment transforms CsPbCl_3

nanocubes into 4-15 monolayer thick CsPbX₃ nanoplates (NPs) with high Φ_{PL} (up to 47% and 65% for violet and blue emitting NPs, respectively, near 100% for green emitting NPs, and 81% for red emitting NPs) while maintaining good long-term stability at room temperature. NC modifications do not directly translate to their thin film counterparts because of variations in surface properties. However, with some ligand engineering, thiol derived surface ligand modified polycrystalline Cs_{0.15}FA_{0.85}PbI₃ photovoltaics show power conversion efficiency of near 17% with enhanced stability. These findings will help pave the way towards efficient and stable future optoelectronic devices.

KEYWORDS: Metal-halide perovskite, colloidal nanocrystal, anion exchange, surface passivation, photoluminescence, photovoltaics

Md Aslam Uddin
(Name of Student)

11/16/2020
Date

DESIGNING METAL-HALIDE PEROVSKITES WITH ENHANCED OPTICAL
PROPERTIES AND STABILITY USING SURFACE LIGANDS

By
Md Aslam Uddin

Kenneth R. Graham

Director of Dissertation

Yinan Wei

Director of Graduate Studies

11/16/2020

Date

DEDICATION

Dedicated to the hardworking people of Bangladesh, who are struggling to build up our country and re-establish the democracy in Bangladesh.

ACKNOWLEDGMENTS

I am very grateful to all the people who helped and supported me through PhD study. Most importantly, my advisor, Dr. Kenneth R. Graham who always supported and guided me to be an independent researcher. I am always grateful to him for giving me a chance to work under him. I also thank all my fellow lab mates who worked in Dr. Graham's lab: Zhiming Liang, Alex M. Boehm, Ashkan Abtahi, So Min Park, Tuo Liu, Harindi Atapattu, Henry Pruett, Kyle Baustert, SSM Tareq Hossain, and Syed Rahmath Ullah Joy for friendly support. Special Thanks to Alex M. Boehm, Ashkan Abtahi, So Min Park, and Tuo Liu for their direct help in my research and learning different instruments and strengthening my troubleshooting skills in our lab.

I wish to thank our collaborator, Dr. Kim for allowing me to work in his lab with anytime-access and Rosemary Lynn Calabro for helping me in learning different instrumental techniques in Dr. Kim's Lab. I also like to thank our other collaborators: Dr. Jonathan T. Pham and Dr. Justin K. Mobley for important help in solving some research problems. Next, I also wish to thank all my committee members and outside examiner: Dr. John Selegue, Dr. Doo Young Kim, Dr. Matthew Beck, and Dr. Yang-Tse Cheng for their support.

I want to thank my friends- specially Shahidul Islam, Md Ariful Haque, and Ahamed Ullah living in USA and my family members- my parents, brother, and sister in Bangladesh for their continual support and having them myside during my ups and downs. Lastly, I want to thank my wonderful wife, Asia Ferdousi and my daughter-little princess, Amirah Nowaira for their continual and eternal love and support.

TABLE OF CONTENTS

ACKNOWLEDGMENTS	iii
LIST OF TABLES	vii
LIST OF FIGURES	viii
CHAPTER 1. INTRODUCTION	1
1.1 Background	1
1.1.1 Semiconducting Materials	1
1.1.2 Exciton in Semiconductors	3
1.2 Semiconducting Perovskite Materials and Their Tunable Dimensionality	5
1.2.1 Band Structure of Metal-halide Perovskite and Their Photoluminescence Properties	8
1.2.2 Compositional Tuning- Anion Exchange Reactions.....	9
1.2.3 Surface Modification of Metal-halide Perovskite Nanocrystals and Thin Films	10
1.3 Applications of Metal-halide Perovskite	13
CHAPTER 2. HALIDE EXCHANGE AND SURFACE TREATMENT OF METAL-HALIDE PEROVSKITE NANOCRYSTALS WITH ALKYLTRICHLOROSILANES	19
2.1 Introduction.....	19
2.2 Experimental Details.....	22
2.2.1 Materials and Chemicals.....	22
2.2.2 Preparation of Cs-Oleate.....	23
2.2.3 Synthesis and Purification of CsPbX ₃ Nanocrystals.....	23
2.2.4 Synthesis of PbCl ₂ assisted anion exchanged CsPbCl ₃ NCs	24
2.2.5 Synthesis of DTS assisted anion exchanged CsPbCl ₃ NCs	24
2.2.6 Stability Measurements.....	25
2.2.7 Characterization	25
2.3 Results And Discussion	27
2.4 Conclusion	37
CHAPTER 3. MECHANISTIC EXPLORATION OF DODECANETHIOL TREATED COLLOIDAL CESIUM LEAD BROMIDE NANOCRYSTALS WITH PHOTOLUMINESCENCE QUANTUM YIELDS REACHING NEAR 100%	38
3.1 Introduction.....	38
3.2 Experimental Details.....	42

3.2.1	Materials and Chemicals.....	42
3.2.2	Synthesis of CsPbBr ₃ Nanocrystals	42
3.2.3	Modification and Purification of CsPbBr ₃ NCs For Fourier Transform Infrared (FTIR), X-Ray Photoelectron Spectroscopy (XPS), and ¹ H Nuclear Magnetic Resonance (NMR) Studies.....	43
3.2.4	Preparation of CsPbBr ₃ Bulk Thin Films for XPS Measurements	43
3.2.5	Absorbance.....	44
3.2.6	Photoluminescence.....	44
3.2.6.1	Measured Using Fluorimeter.....	44
3.2.6.2	Measured Using 405 nm Laser and Fiber Optic CCD Spectrometer....	45
3.2.7	Photoluminescence Quantum Yields (Φ_{PL})	45
3.2.8	Photoluminescence Lifetimes.....	45
3.2.9	Transmission Electron Microscopy (TEM)	46
3.2.10	X-Ray Diffraction	46
3.2.11	Fourier-Transform Infrared (FTIR) Absorbance	46
3.2.12	X-Ray Photoelectron Spectroscopy (XPS)	47
3.2.13	¹ H Nuclear Magnetic Resonance (NMR)	47
3.3	Results AND Discussion.....	48
3.4	Conclusion	66
CHAPTER 4. Growth of Highly Stable and Luminescent metal-halide perovskite Nanoplates via Ligand Mediated Anion Exchange of CsPbCl ₃ Nanocubes with AIX ₃ ... 68		
4.1	Introduction.....	68
4.2	Experimental Details.....	70
4.2.1	Materials	70
4.2.2	Synthesis of CsPbX ₃ Nanocubes	71
4.2.3	Preparation of C ₁₂ H ₂₅ SH-C ₄ H ₁₀ O-AIX ₃ Solutions	72
4.2.4	Synthesis of DDT-AIX ₃ Treated NPs	72
4.2.5	Characterization Methods	74
4.2.5.1	Absorbance.....	74
4.2.5.2	Fluorescence AND Φ_{PL} Measurements	74
4.2.5.3	Photoluminescence Lifetimes.....	75
4.2.5.4	Fourier Transform Infrared (FTIR) Absorbance	75
4.2.5.5	Raman Spectroscopy.....	75
4.2.5.6	Transmission Electron Micrographs (TEM).....	76
4.2.5.7	Atomic Force Microscope (AFM) Images	76
4.2.5.8	X-Ray Diffraction	76
4.3	Results and Discussion	77
4.4	Conclusion	101

CHAPTER 5. Effects of Sulfur and Selenium-Based Surface Ligands on Photoluminescence and Photovoltaic Performance of $\text{Cs}_{0.15}\text{FA}_{0.85}\text{PbI}_3$ Metal-halide Perovskites	102
5.1 Introduction.....	102
5.2 Experimental Details.....	105
5.2.1 Materials and Chemicals.....	105
5.2.2 Device Fabrication and Characterization.....	105
5.2.3 Device Testing and Active Characterization	107
5.2.4 Thin Film Characterization.....	108
5.2.4.1 Absorbance	108
5.2.4.2 Fluorescence.....	108
5.2.4.3 Scanning Electron Microscopy (SEM).....	108
5.2.4.4 X-Ray Diffraction	109
5.2.4.5 Photoelectron Spectroscopic (PES) Measurements	109
5.3 Results and Discussion	109
5.4 CONCLUSION.....	121
CHAPTER 6. Summary and Perspective.....	122
6.1 Overall Summary of This Work	122
6.2 Future Research Plan	124
6.3 Career Research Interest	124
References.....	126
VITA.....	156

LIST OF TABLES

Table 3.1 Moles of each added surface ligand and the ratio of moles of surface ligand to moles of NCs for the fluorescence measurements.	49
Table 4.1 amounts of as-syn. NCs, hexane (volume has a minimal influence), and AlX ₃ solutions used in the treatment of CsPbCl ₃ NCs to form CsPbX ₃ NPs.	73
Table 4.2 shows the minimum Φ_{PL} , median Φ_{PL} , maximum Φ_{PL} , and average Φ_{PL} from four separate batches of DDT-AlX ₃ treated CsPbCl ₃ , CsPbCl _{3-x} Br _x , CsPbBr ₃ , and CsPbI ₃ NCs.	96
Table 4.3 Lifetimes (τ_1 & τ_2), components (B_1 & B_2), and average lifetimes (τ_{avg}) of as-synthesized CsPbCl ₃ NCs and DDT-AlX ₃ treated CsPbX ₃ NCs.	96
Table 5.1 J-V parameters from the devices described in Figure 5.3a and b measured from J_{sc} to PCE under 1 sun illumination.	112

LIST OF FIGURES

Figure 1.1 Schematic illustration of electronic energy levels of free atoms and energy bands of semiconductors consisting of a large number of atoms. It also shows the position of Fermi level with respect to the electronic energy bands (VB and CB) in a semiconductor. ²	2
Figure 1.2 (a) Coulomb interaction between a hole in VB and an electron in CB in a semiconductor, (b) a Frenkel exciton, and (c) a Wannier-Mott Exciton. ²	3
Figure 1.3 Perovskite crystal structure showing B site-cation (in blue gray color) in 6-fold coordination, surrounded by an octahedron of anions, X (in maroon color) and A site-cation (in aqua color) in 12-fold cubo-octahedral coordination.	5
Figure 1.4 Relationship between size of CsPbBr ₃ crystals and bandgap of the material. ^{34,35}	6
Figure 1.5 Simplified depiction of the bonding in APbI ₃ (adapted from ref. 62). ⁶²	8
Figure 1.6 Schematic representation of halide exchange between metal-halide perovskite and different halide-source.	9
Figure 1.7 shows a schematic representation of roles of surface ligands in maintaining stability and PL properties of metal-halide perovskites.....	11
Figure 1.8 Schematic representation of (a) post-treatment of metal-halide perovskite thin films using surface ligands and (b) depicting surface modification of perovskite photovoltaics using an inter-layer of surface ligands between perovskite and electron transporting layer (ETL).	12
Figure 1.9 (a) p-i-n structure and (b) n-i-p structure of stacking layers in fabricated photovoltaic devices.....	15
Figure 1.10 Schematic representation of (a) potential transport energetics between the perovskite layer and carrier extraction layers and (b) roles of carrier extraction layers...	16
Figure 1.11 J-V characteristics of p-i-n heterojunction of a Cs _{0.15} FA _{0.85} PbI ₃ photovoltaic device under 1 sun illumination performed in our lab.....	17
Figure 2.1 (a) Optical absorption and PL emission spectra (inset showing optical photograph of parent CsPbBr ₃ NCs under a 365 nm UV lamp), (b) high resolution TEM image, (c) XRD patterns, and (d) PL lifetime decay of parent CsPbBr ₃ NCs.	27
Figure 2.2 (a) A proposed mechanism of synthesizing DTS assisted anion exchanged NCs; (b, c) time-dependent UV-Vis absorbance (nonnormalized) and normalized PL emission spectra of DTS assisted anion exchanged NCs at 5 minute intervals; (d) time-dependent PL emission spectra showing the PL emission maxima at 5 minute intervals; (e) PL emission spectra of DTS assisted anion exchanged NCs after 30 minutes of addition of 50, 200, and 300 μ L of DTS to the 3 mL colloidal solution of parent NCs at room temperature (inset shows optical photographs of 50, 200, and 300 μ L DTS assisted anion exchanged NCs under a 365 nm UV lamp); and (f) a list of trichlorosilanes used in this study.	29

Figure 2.3 (a) Optical absorption (dashed lines) and PL emission (solid lines) spectra of DTS assisted anion exchanged CsPbCl₃ NCs (blue, 300 μL DTS + 1.2 μM*3 mL parent NC dispersion) and PbCl₂ assisted anion exchanged CsPbCl₃ NCs (violet). Inset in 2.3a shows optical photographs of PbCl₂ and 300 μL DTS assisted anion exchanged NCs under a 365 nm UV lamp; HR-TEM images of (b) 50 μL DTS assisted anion exchanged CsPbCl₃ NCs; (c) PbCl₂ assisted anion exchanged CsPbCl₃ NCs; and (d) comparison of XRD patterns of DTS and PbCl₂ assisted anion exchanged NCs. 31

Figure 2.4 (a) Time-dependent PLQYs of DTS and PbCl₂ assisted anion exchanged NCs stored in capped vials in ambient air; (b) PL intensity of PbCl₂ assisted anion exchanged NCs, and DTS assisted anion exchanged NCs as a function of time showing photobleaching; (c) time-dependent PL emission spectra showing stability of solid thin film prepared from DTS assisted anion exchanged CsPbCl₃ NCs via drop casting; (d) PL lifetime decays 2 days after anion exchange and the instrumental response function (IRF); and table showing time-dependent average lifetimes, τ of DTS assisted anion exchanged NCs and PbCl₂ assisted anion exchanged CsPbCl₃ NCs on a day-scale. 32

Figure 2.5 (a) PL spectra changes upon adding 100 μL of water to 1.2 μM*3 mL of DTS and PbCl₂ assisted anion exchanged NCs in hexane; (b) time-dependent PL emission spectra showing stability of DTS assisted anion exchange CsPbCl₃ NCs over days in exposure of 100 μL distilled water to 1.2 μM*3 mL colloidal dispersion of DTS assisted anion exchanged CsPbCl₃ NCs; (c, d) FTIR spectra of pure DTS, DTS assisted anion exchanged NCs, PbCl₂ assisted anion exchanged NCs, and host NCs; and (e) FT-IR spectra of DTS with added water and DTS exchanged NCs with added water showing the Si-O stretching mode and a peak that is suspected to arise from Si-O groups where the oxygen is coordinated with Pb..... 35

Figure 3.1 PL quantum yield of CsPbBr₃ NCs as a function of time in (a) hours and (b) days after addition of varying surface ligands and (c) days and (d) minutes after addition of alkyl thiols with varying alkyl chain lengths to the as-synthesized NC dispersions.... 50

Figure 3.2 (a) Optical absorbance and PL emission spectra with no added DDT and 10 days after DDT addition, (b) time-dependent PL spectra of CsPbBr₃ NCs after addition of DDT, (c) comparison of time-resolved PL lifetime decays of as-synthesized and DDT treated NCs, (d and e) XRD patterns of as-synthesized NCs and DDT-NCs as a function of precursor stoichiometry, HAADF-STEM images and size distributions of (f and g) as-synthesized NCs (0.25), and (h and i) DDT-NCs (0.25) with calculated squareness. In (b) the time refers to the time after DDT was added to the NC dispersion, with the t = 0 spectrum recorded immediately before DDT addition. 52

Figure 3.3 (a) FTIR spectra of sodium stearate (SS), oleic acid (OA), dodecanethiol (DDT), as-synthesized NCs, and purified DDT-NCs 12 days after DDT addition; (b & c) time-dependent FTIR spectra of as-synthesized CsPbBr₃ NCs before (t = 0 min) and after addition of DDT at different time intervals; ¹H NMR of (d) DDT, as-synthesized NCs, and purified DDT-NCs; and (e) a mixture of parent ligands and DDT without NCs added and dioctylsulfide (DOS). 55

Figure 3.4 Base and photocatalyzed thiol-ene reactions showing reactions between DDT and (a) ODE molecules, (b) OA⁻, and (c) OLA/ OLA⁺ present in the as-synthesized NCs. 56

Figure 3.5 (a) Crystal fringes of as-synthesized NCs (0.25) with crystal fringes of black dots of metallic Pb particles, (b) SAED patterns of as-synthesized NCs (0.25), (c) crystal fringes of DDT-NCs, (d) SAED patterns of DDT-NCs (0.25), (e) HAADF-STEM images of as-synthesized CsPbBr₃ NCs with Cs:Pb ratio of 0.5, and (f) EDX spectra of as-synthesized NCs (0.5) that identify the small particles as metallic Pb. 58

Figure 3.6 (a) Optical absorption & PL emission spectra of initially synthesized CsPbBr₃ NCs (insets show respective optical colors of the colloidal NC dispersion, prepared by dispersing 10 μL of as-synthesized NCs into 2 mL hexane, under a 365 nm UV lamp), (b) TEM images, and (c) time-resolved PL lifetime decays of as-synthesized NCs as a function of precursor stoichiometry. 59

Figure 3.7 TEM images showing (a) as-synthesized NCs; (b) DDT-NCs (Cs:Pb ratio of 0.25); c(i) HAADF-STEM image and c(ii-v) STEM-EDS elemental mapping images of Cs, Pb, Br, and S of purified DDT-NCs (0.25); (d) STEM-EDS elemental line scan of purified DDT-NC (scan step size was 0.061 nm along the yellow line shown in HAADF-STEM image). 60

Figure 3.8 (a) Time-dependent Φ_{PL} showing the increase in Φ_{PL} of as-synthesized NCs as a function of precursor stoichiometry after addition of DDT, (b) Φ_{PL} of as-synthesized NCs followed by Φ_{PL} of DDT-NCs (0.25) from different batches synthesized with the same conditions, (c, d, and e) time-resolved PL lifetime decays of as-synthesized NCs and DDT-NCs as a function of Cs/Pb ratios of 0.50, 0.35, and 0.20., (f) time-dependent Φ_{PL} showing the increase in Φ_{PL} of as-synthesized NCs as a standard precursor stoichiometry after addition of DDT over 25 days, (g) time-dependent Φ_{PL} of as-synthesized NCs from two different batches showing decrease in Φ_{PL} over time, and (h) time-dependent PL intensity of DOS-NCs (DOS = dioctyl sulfide). In Figure 3.8a and f-h the day refers to the time after the thiol was added to the NC dispersion to enhance the Φ_{PL} of near unity, with the t = 0 (hour/day) spectrum recorded immediately before thiol addition. 62

Figure 3.9 XPS spectra of comparison of S2p region of (a) as-synthesized NCs & purified DDT-NCs; (b) as-spin coated CsPbBr₃ & DDT/DOS-CsPbBr₃ bulk thin films; and (c) effects of DDT treatments for different Cs:Pb stoichiometries: as-spin coated CsPbBr₃ & DDT-CsPbBr₃ bulk thin films prepared as a function of different Cs:Pb ratios. Solid area and broken area indicate 2p_{3/2} and 2p_{1/2} regions, respectively. 64

Figure 3.10 (a) Time-dependent integrated PL intensity of as-synthesized NCs upon addition of DDT under basic conditions (in presence of bases) and after 30 minutes of continuous 405 nm laser irradiation, (b) time-dependent Φ_{PL} of as-synthesized NCs (0.25) from two batches after addition of DDT under a 365 nm UV light, and (c) comparison of time-resolved PL lifetime decays of as-synthesized NCs before and after UV light exposure. In Figure 3.10b, the time refers to the time after the thiol was added to the NC dispersion to enhance the Φ_{PL} of near unity, with the t = 0 (minute) spectrum recorded immediately before thiol addition. 65

Figure 3.11 NMR data showing the -CH₂-S region for (a) a solution of DDT and ODE after 30 minutes of 405 nm laser light exposure and (b) a solution of DDT and ODE with CsPbBr₃ NCs after 30 minutes of 405 nm laser light exposure. The quartet in the sample without CsPbBr₃ NCs indicates that DDT is still in the thiol form, whereas with the NCs the triplet indicates that DDT has reacted to form thioethers or disulfides. This measurement was directly done after 30 minutes of 405 nm laser light exposure without further purification of DDT-NCs. 66

Figure 4.1 (a) Anion exchange between CsPbCl ₃ and AlX ₃ in the presence of dissolved water in hexane; (b) role of excess halide ions and thiolate ions in the ligand mediated anion exchange route with AlX ₃ .	77
Figure 4.2 (a) UV-Vis absorbance & PL emission, (b) time-resolved PL lifetime decays, (c-e) TEM images, and (f) XRD patterns of as-synthesized CsPbX ₃ NCs.	78
Figure 4.3 Time-dependent PL intensity of (a) AlCl ₃ treated CsPbCl ₃ (with no DDT added in the parent CsPbCl ₃ dispersion) and (b) DDT treated CsPbCl ₃ NCs (with no AlCl ₃ added in the parent CsPbCl ₃ dispersion).	79
Figure 4.4 Time-dependent PL emission spectra of (a-c) AlX ₃ treated CsPbBr ₃ NCs & (d-f) AlX ₃ treated CsPbI ₃ NCs and time-dependent optical absorbance spectra of (g) AlCl ₃ treated CsPbI ₃ NCs & (h) AlI ₃ treated CsPbBr ₃ NCs (all spectra are nearly identical and fall on top of each other). In 4.3.4a-h, all the experiments were done with no additional DDT in the parent CsPbCl ₃ dispersion.	80
Figure 4.5 Time-dependent UV-Vis absorbance & PL intensity of DDT-AlX ₃ treated NCs: (a, b) treated CsPbCl ₃ NCs, (c, d) exchanged CsPbBr ₃ NCs, (e, f) exchanged CsPbI ₃ NCs, and (g) PL emission spectra of DDT-AlX ₃ treated NCs covering the visible spectra ranging from 410 nm to 680 nm.	81
Figure 4.6 (a) UV-Vis absorbance (dashed lines) and PL emission spectra (solid lines) of parent CsPbCl ₃ NCs (black) and treated CsPbX ₃ NCs produced from DDT-AlX ₃ treatment of parent CsPbCl ₃ nanocubes, (b) TEM image of parent CsPbCl ₃ nanocubes, and (c-e) STEM images of treated CsPbX ₃ NPs produced from DDT-AlX ₃ treatment of CsPbCl ₃ NCs. Insets in 4.6a show optical photographs of respective NC dispersions under illumination with 365 nm UV light and the inset in 4.6b shows the size distribution of parent CsPbCl ₃ NCs.	83
Figure 4.7 (a) Tapping mode AFM height image of treated CsPbCl ₃ NCs & (b) height profile from the image shown in 4.7a along the NC indicated with violet line; (c) tapping mode AFM height image of exchange CsPbBr ₃ NCs and (d) height profile from the image shown in 4.7c along the NC indicated with green line; and (e) tapping mode AFM height image of exchanged CsPbI ₃ NCs & (f) height profile from the image shown in 4.7e along the NC indicated with red line.	84
Figure 4.8 Size distributions from STEM images of: (a) treated CsPbCl ₃ , (b) exchanged CsPbBr ₃ , and (c) exchanged CsPbI ₃ NCs synthesized through DDT-AlX ₃ treatment of CsPbCl ₃ NCs.	85

Figure 4.9 (a) XRD patterns of DDT-AIX₃ treated CsPbX₃ NCs produced from DDT-AIX₃ treatment of parent CsPbCl₃ nanocubes; comparison of (b) XRD patterns of parent CsPbCl₃ & treated CsPbCl₃ NCs synthesized through DDT-AlCl₃ treatment of CsPbCl₃ NCs; (c) (200) peaks in XRD patterns of as-syn. CsPbCl₃ & treated CsPbCl₃ NCs synthesized through DDT-AlCl₃ treatment of CsPbCl₃ NCs ; (d) PL spectra of as-synthesized CsPbBr₃ & exchanged CsPbBr₃ NCs synthesized through DDT-AlBr₃ treatment of CsPbCl₃ NCs; (e) XRD patterns of as-synthesized CsPbBr₃ NCs, only DDT-AlBr₃, exchanged CsPbBr₃ NCs synthesized through only AlBr₃ treatment of CsPbCl₃ NCs, & exchanged CsPbBr₃ NCs synthesized through DDT-AlBr₃ treatment of CsPbCl₃ NCs; (f) STEM image of aged DDT treated CsPbBr₃ NCs; and (g) XRD patterns of as-synthesized CsPbBr₃ NCs & aged DDT treated CsPbBr₃ NCs (inset showing comparison of (200) diffraction peaks). In 4.9f and g, the experiments were done with no additional AIX₃ in the parent CsPbBr₃ dispersion and * indicates Cs₄PbBr₆ formation.²²¹ 86

Figure 4.10 (a) HAADF-STEM image and (b-g) STEM-EDS elemental mapping images of Cs, Pb, Br, Cl, Al, & S of a 2x washed treated CsPbBr₃ NC; and (h) STEM-EDS line scan of the 2x washed treated NC shown in the HAADF-STEM image in 4.10a. 88

Figure 4.11 (a) HAADF-STEM image of exchanged CsPbBr₃ NCs synthesized through AlBr₃ treatment of CsPbCl₃ NCs, (b) Al(OH)_nX_{3-n} precipitates resulting from the synthesis, and (c-h) STEM-EDS elemental mapping images of Cs, Pb, Br, Cl, Al, & O of the Al(OH)_nX_{3-n} precipitate shown in 4.11b. 89

Figure 4.12 (a) Raman spectra of DDT, parent CsPbCl₃ NCs, & treated CsPbCl₃ NCs synthesized through DDT-AlCl₃ treatment of CsPbCl₃ NCs; FTIR spectra of (b) DDT, Al(OH)₃, DDT-AlCl₃, parent CsPbCl₃ NCs, & treated CsPbCl₃ NCs; and (c, d) Al₂O₃, DDT-AlCl₃, Al(OH)₃, parent CsPbCl₃ NCs, & treated CsPbCl₃ NCs..... 90

Figure 4.13 A schematic presentation of self-assembly and fusion of parent NCs into NPs; (b and c) TEM images of assemblies of treated CsPbX₃ NCs showing the larger fused NPs and (c) lattice fringes of larger fused CsPbBr₃ NPs..... 92

Figure 4.14 (a-f) Time-dependent absorbance and PL (relative irradiance = RI) of treated CsPbCl₃, exchanged CsPbBr₃ NCs, and CsPbI₃ NCs after addition of DDT-AIX₃ solutions over the first 18 seconds. 94

Figure 4.15 (a) Φ_{PL} & (b) time-resolved PL lifetime decays of AIX₃ treated CsPbX₃ NCs (violet dashed line indicates lifetime decay of parent CsPbCl₃ NCs in 4.15b) and (c) time-dependent Φ_{PL} of treated CsPbX₃ NCs following DDT-AIX₃ treatment. Both Φ_{PL} and PL lifetimes in 4.15a and b were collected within 1-5 days after the DDT-AIX₃ treatment.. 97

Figure 4.16 Time-dependent optical images of CsPbCl₃ NPs, CsPbBr₃ NPs, and CsPbI₃ NPs synthesized through DDT-AIX₃ treatment of CsPbCl₃ nanocubes. 98

Figure 4.17 Time-dependent XRD patterns of: (a) treated CsPbCl₃ NCs, (b) exchanged CsPbBr₃ NCs, and (c) exchanged CsPbI₃ NCs synthesized through DDT-AIX₃ treatment of CsPbCl₃ NCs. XRD data were collected on the same day of preparation or one day after preparation. 99

Figure 4.18 Optical absorbance & PL emission spectra and TEM images of more than 6-month old (a, b) treated CsPbCl₃ NCs, (c, d) partially exchanged CsPbCl_{3-x}Br_x NCs, (e, f) exchanged CsPbBr₃ NCs, (g, h) exchanged CsPbI₃ NCs, and (i) λ_{max} vs Φ_{PL} of 6-month old treated CsPbX₃ NCs synthesized through DDT-AIX₃ treatment of CsPbCl₃ NCs. 100

Figure 5.1	Time-dependent PL Spectra of colloidal (a) CsPbCl ₃ NCs, (b) CsPbBr ₃ NCs, and (c) CsPbI ₃ NCs upon addition of dodecanethiol.	110
Figure 5.2	Schematics of (a) comparison of S and Se-based ligands and (b) p-i-n structure of fabricated perovskite photovoltaic devices with perovskite layer being modified with both S and Se-based ligands.	110
Figure 5.3	Direct and inverse scans of (a) ITO/PTAA/Cs _{0.15} FA _{0.85} PbI ₃ +5%PbI ₂ /C ₆₀ /BCP/Al and (b) ITO/PTAA/Cs _{0.15} FA _{0.85} PbI ₃ +5%PbI ₂ +Pyridine/C ₆₀ /BCP/Al photovoltaic devices.	111
Figure 5.4	Comparison of XRD patterns of perovskite thin films fabricated with and without pyridine. In Figure 5.4, CFPI = Cs _{0.15} FA _{0.85} PbI ₃ , P = perovskite, and Py = pyridine.	113
Figure 5.5	High resolution XPS small region scans of (a and b) S2p region and C1s region of S-based ligands treated Cs _{0.15} FA _{0.85} PbI ₃ thin films, (c and d) Se3d region and C1s of Se-based ligands treated Cs _{0.15} FA _{0.85} PbI ₃ thin films. In Figure 5.5a-d, CFPI = Cs _{0.15} FA _{0.85} PbI ₃ , P = perovskite, Py = pyridine, DDT = dodecanethiol, TP = thiophenol, MTP = 4-methoxythiophenol, PS = phenylselenol, PSB = phenylselenenyl bromide, and BSA = benzeneseleninic acid.....	115
Figure 5.6	Comparison of optical absorbance and PL spectra of (a and b) pristine and S-based ligands treated Cs _{0.15} FA _{0.85} PbI ₃ thin films and (c and d) pristine and Se-based ligands treated Cs _{0.15} FA _{0.85} PbI ₃ thin films. In Figure 5.6a-d, CFPI = Cs _{0.15} FA _{0.85} PbI ₃ , P = perovskite, Py = pyridine, DDT = dodecanethiol, TP = thiophenol, MTP = 4-methoxythiophenol, PS = phenylselenol, PSB = phenylselenenyl bromide, and BSA = benzeneseleninic acid.....	117
Figure 5.7	Comparison of XRD patterns of (a) pristine and S-based ligands treated Cs _{0.15} FA _{0.85} PbI ₃ thin films and (b) pristine and Se-based ligands treated Cs _{0.15} FA _{0.85} PbI ₃ thin films. In Figure 5.7a and b, CFPI = Cs _{0.15} FA _{0.85} PbI ₃ , P = perovskite, Py = pyridine, DDT = dodecanethiol, TP = thiophenol, MTP = 4-methoxythiophenol, PS = phenylselenol, PSB = phenylselenenyl bromide, and BSA = benzeneseleninic acid.	118
Figure 5.8	<i>Film morphology</i> : SEM images of (a-c) S-based ligands and (d-f) Se-based ligands modified thin films. In Figure 5.8, DDT = dodecanethiol, TP = thiophenol, MTP = 4-methoxythiophenol, PS = phenylselenol, PSB = phenylselenenyl bromide, and BSA = benzeneseleninic acid.....	119
Figure 5.9	<i>PV Statistics and Stability</i> : (a-d) performance (J _{sc} , V _{oc} , FF, and PCE) of PVs using different surface ligand treated thin films. In Figure 5.9, Con = Cs _{0.15} FA _{0.85} PbI ₃ , DDT = dodecanethiol, TP = thiophenol, MTP = 4-methoxythiophenol, PS = phenylselenol, PSB = phenylselenenyl bromide, and BSA = benzeneseleninic acid.	120

CHAPTER 1. INTRODUCTION

1.1 Background

Semiconducting materials are important types of materials in our daily life because these materials are heavily used in electrical components, electronics, and optoelectronic devices, such as transistors, diodes, photovoltaics, and so on, which enable the technological advancements and electronic devices that underpin our modern world. There are some heavily researched semiconducting materials including Si, CdTe, $\text{Cu}(\text{In}_x\text{G}_{1-x})\text{Se}_2$, CdS, CdSe, etc. These semiconductors can be processed for fabricating electronic and optoelectronic devices. In this chapter, the fundamentals of semiconductors, metal-halide perovskite as a class of semiconductors, and applications of metal-halide perovskites in optoelectronics will be discussed.

1.1.1 Semiconducting Materials

A single free atom has discrete energy levels for electrons. In contrast, when a large number of atoms come close to each other, are arranged in a periodical order, they make a solid crystal lattice. As a large number of atoms come close to form a solid crystal lattice, the wavefunctions of electrons in different atoms overlap and the atomic energy levels start splitting. When enough atoms are included in the crystals, quasi-continuous energy bands of low energy and high energy are formed. When the gap between lowest energy and highest energy bands of electronics states in materials reaches between 1.0-4.0 eV are called semiconductors.¹ The two continuous bands of electronic states that are most relevant to electronic devices are the valence and conduction band, where the valence band (VB) is the band of occupied electronic states with the highest energy and the conduction

band (CB) is the band of unoccupied electronic states with the lowest energy as depicted in **Figure 1.1**.

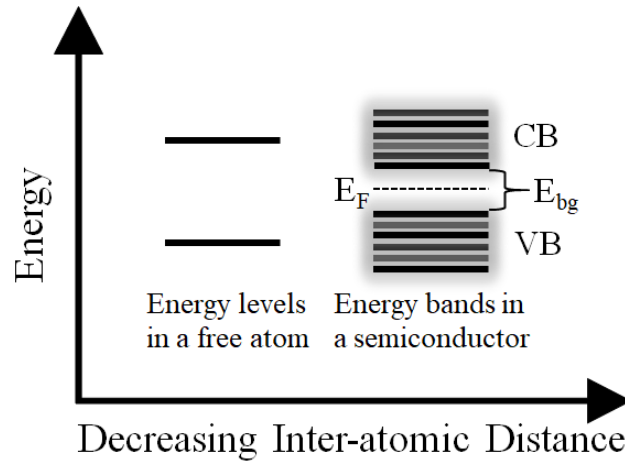


Figure 1.1 Schematic illustration of electronic energy levels of free atoms and energy bands of semiconductors consisting of a large number of atoms. It also shows the position of Fermi level with respect to the electronic energy bands (VB and CB) in a semiconductor.²

The distance between the valence band maximum (VBM) and conduction band minimum (CBM) is called a bandgap, E_{bg} and Fermi energy, E_F , indicated by a dash line lies inside the bandgap. At -273.15 °C, the probability of finding electrons having energy higher than E_F is zero. However, if semiconductors are thermally or optically excited, the probability of finding electrons having energy higher than E_F increases. Since semiconductors have smaller band gap energy compared to insulators, electrical conductivity of the semiconductors can be enhanced via thermal heating. Photoexcitation is also a common phenomenon for semiconductors, where electrons in the VB are photoexcited by absorbing photons with energy higher than the E_{bg} . As a class of semiconducting materials, perovskite materials show interesting photoexcitation behaviors which will be discussed later in this chapter and the following chapters in details.

1.1.2 Exciton in Semiconductors

Photoexcitation can generate holes in the VB and electrons in the CB in the semiconductors. These opposite charge particles can be bound through an attractive force resulting from Coulomb potential. Coulomb potential is defined by the following equation 1.1:²

$$U(r) = -\frac{e^2}{2\pi\epsilon\epsilon_0r^2} \dots\dots\dots 1.1$$

Where r is the distance between the hole and electron, ϵ is the dielectric constant of the material, and ϵ_0 dielectric constant of vacuum.² A strong Coulomb interaction will make the electron and hole to be in a bound state. This bound state of electrons and holes is called excitons as depicted in the following **Figure 1.2a**.

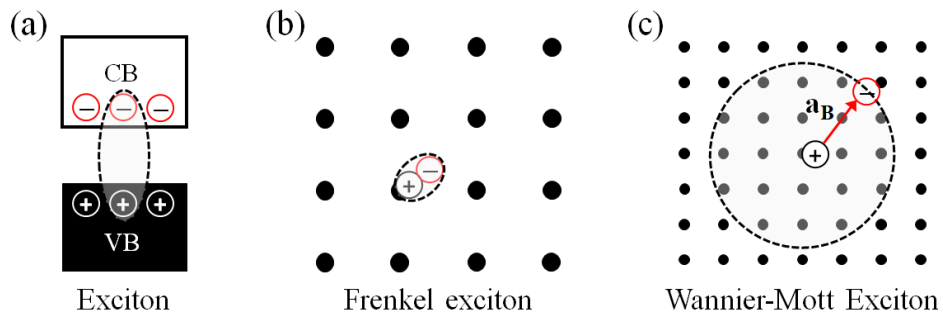


Figure 1.2 (a) Coulomb interaction between a hole in VB and an electron in CB in a semiconductor, (b) a Frenkel exciton, and (c) a Wannier-Mott Exciton.²

Depending on the Coulomb interaction, there are two types of excitons can be formed in the semiconductors: Frenkel excitons and Wannier-Mott excitons as depicted in **Figure 1.2b and c**, respectively.^{3,4} Frenkel excitons are tightly bound excitons which are generally localized at a specific atom or molecule. They can typically be found in alkali halide crystals and organic molecular materials. In these materials, Coulomb interaction between the electron and hole is strong and the exciton Bohr radius (r_B) is small due to the small dielectric constants of the semiconducting materials. On the other hand, Wannier-Mott excitons are less tightly bound because of large dielectric constant of the semiconductors. A strong dielectric screening and more delocalized electronic states reduce the Coulomb interaction between electrons and holes. Wannier-Mott excitons can be found in many semiconductors. In these semiconductors, the small effective mass of electrons favors a large r_B and thus a Wannier-Mott exciton is generally much larger than the lattice spacing. A Wannier-Mott exciton is usually delocalized, and it can move inside the materials. So, they can easily dissociate into free charges.

The exciton binding energy is primarily dictated by the material's dielectric constants as described above. In organic semiconductors, the dielectric constant is usually quite small resulting in excitons with high binding energies (>0.2 eV) that are difficult to dissociate into free charges.⁵ In contrast, crystalline silicon typically has a very high dielectric constant resulting in excitons with low binding energies (<0.015 eV) that easily dissociate into free charges because their binding energy is less than kT at room temperature.^{4,5} Metal-halide perovskite materials fall somewhere in-between the above range of binding energies. Perovskites can form Wannier-Mott type excitons and binding energies are reported in the range of 0.012-0.098 eV.^{5,6}

1.2 Semiconducting Perovskite Materials and Their Tunable Dimensionality

An interesting emerging class of semiconducting materials is perovskite. The name ‘perovskite’ was originally given to CaTiO_3 and was coined after Lev Perovski, a Russian mineralogist.⁷ The general formula of this material is ABX_3 . Metal-oxides are the common forms of this class of materials. The perovskite has the ideal crystal structure with B site-cation in 6-fold coordination, surrounded by an octahedron of anions and A site-cation in 12-fold cubo-octahedral coordination as shown in **Figure 1.3**.

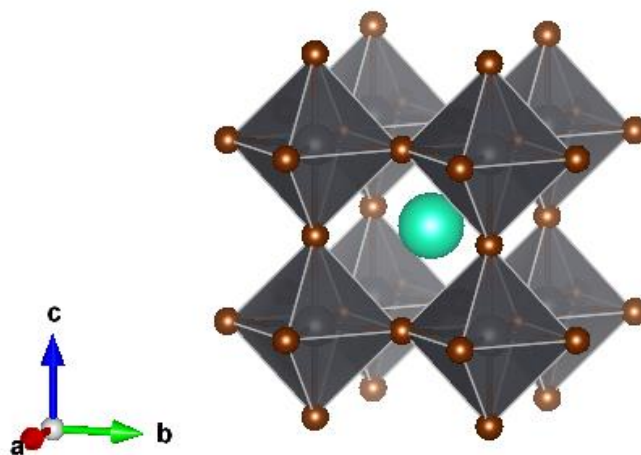


Figure 1.3 Perovskite crystal structure showing B site-cation (in blue gray color) in 6-fold coordination, surrounded by an octahedron of anions, X (in maroon color) and A site-cation (in aqua color) in 12-fold cubo-octahedral coordination.

For optoelectronic applications, halide-based perovskites are more extensively used. The general formula of this material is ABX_3 , where $\text{A} = \text{Cs}^+/\text{CH}_3\text{NH}_3^+/\text{NH}_2\text{CHNH}_2^+$, $\text{B} = \text{Pb}^{2+}/\text{Sn}^{2+}$, and $\text{X} = \text{Cl}^-/\text{Br}^-/\text{I}^-$. These materials have attractive electronic properties, such as tunable direct bandgaps,^{8,9} high absorption

coefficients,¹⁰ and balanced carrier transport,¹¹ as well as desirable optical properties, such as narrow emission line-widths and high Φ_{PL} .¹²⁻²⁰ Solution processed-bulk perovskite films have already been garnering significantly more interest for low cost photovoltaics,²¹ whereas the emergence of colloidal MHP NCs after first reported by Schmidt and her coworkers and later by Protesescu and her coworkers is broadening the interests in the metal-halide perovskite NCs.^{12,22} Perovskite nanomaterials are now attractive alternatives for light emitting diodes (LEDs) and also for photovoltaics owing to their interesting PL properties including narrow emission line-widths, low rate of non-radiative recombination, and high Φ_{PL} .²³⁻²⁷ In addition, colloidal versions of these semiconductors are more advantageous because of their facile tunable composition, size, shape, and most importantly better emission due to exciton confinement.^{12,28-33}

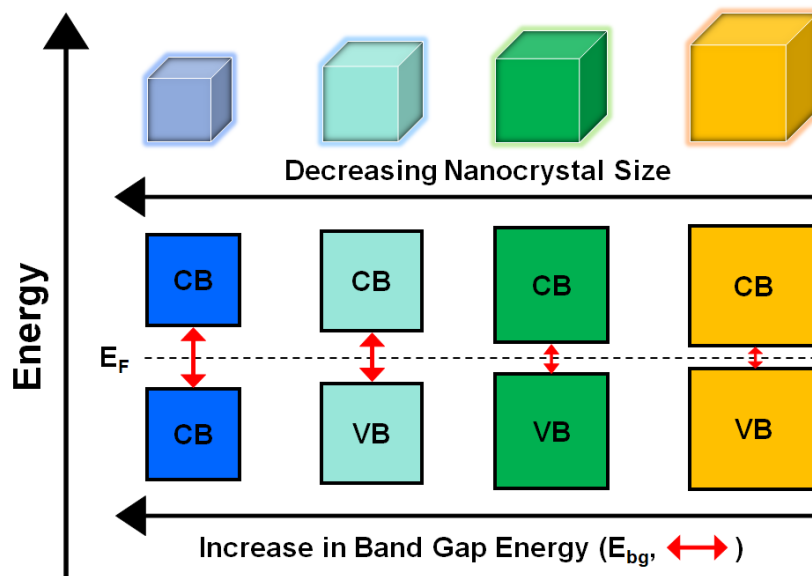


Figure 1.4 Relationship between size of CsPbBr₃ crystals and bandgap of the material.^{34,35}

During synthesis of this new class of semiconductors, one can tune the size of this semiconductors from the micrometer to nanometer range by varying capping ligands, solvents, and reaction temperature during hot-injection method or one-pot synthetic method.^{30,36} As the size of the crystal changes, their electronic and optical properties also change drastically. **Figure 1.4** shows size-dependent variation of bandgap of CsPbBr₃ crystals as an example of perovskite materials.³⁷⁻⁴⁰

In addition, low-dimensional semiconductors including perovskites are of great importance for both fundamental (photo)physics and advanced applications.⁴¹⁻⁴³ If size of any material is reduced to the nanometer scale, carrier wavefunction is considered to be finite. And this is how quantum confinement effects come in to play.^{44,45} The material system can be confined to zero dimension (0D), 1D, and 2D,⁴⁶ resulting in low-dimensional semiconductors including 0D quantum dots,⁴⁷ 1D quantum wires, and 2D quantum wells.^{42,43,48} Quantum size effects have pronounced impacts on the behavior of charge carriers in semiconductors, and dramatically manipulate the electronic and PL properties of such nanostructures.⁴⁹⁻⁵² Previously, low dimensional nanostructures are usually fabricated in solid-state fabrication by epitaxial growth,⁴² lithography, or thermal evaporation.⁴⁸ But last few decades, the solution/thermally evaporation synthesis of colloidal semiconducting quantum structures has become an alternative way to the solid-state fabrication because of facile and tunable procedures.^{43,52-54}

1.2.1 Band Structure of Metal-halide Perovskite and Their Photoluminescence Properties

This class of materials is thought to be highly defect tolerant because they constantly show high Φ_{PL} without resorting to any electronic surface passivation, whereas passivation is mandatory to achieve high Φ_{PL} for other conventional quantum dots, e.g., metal chalcogenides and metal pnictides. In MHPs, surface defects,⁵⁵ point defects in the bulk,⁵⁶ and grain boundaries^{57–60} were shown to form shallow trap states near the band edges or trap states that are resonant with the VB and CB states.⁶¹

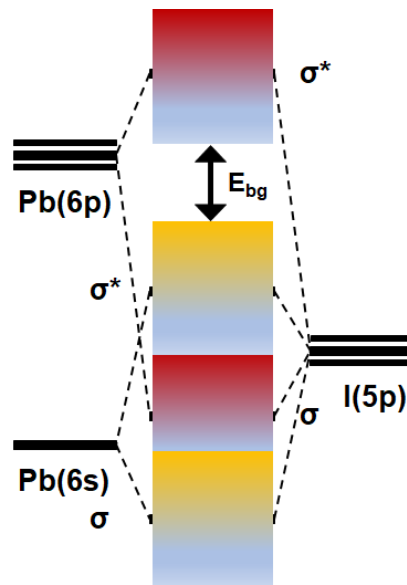


Figure 1.5 Simplified depiction of the bonding in APbI₃ (adapted from ref. 62).⁶²

Importantly, by contrast to chalcogenide and pnictide containing NCs where the band gap opens up between bonding and antibonding orbitals, the band gap in the MHPs opens up between two antibonding bands due to the mixing of a Pb lone pair ‘s orbital’

and an iodine ‘p orbital’ resulting in antibonding coupling.⁶² This is the reason, why this class of materials are defect tolerant and show high Φ_{PL} .

1.2.2 Compositional Tuning- Anion Exchange Reactions

Bandgap energies and PL emission spectra of these synthesized MHPs are easily tunable over the entire visible spectral range of 410-700 nm with Φ_{PL} of up to ~100% for certain compositions via adjusting the halide composition or taking advantage of quantum size-effects.^{12,15,28,63–67}

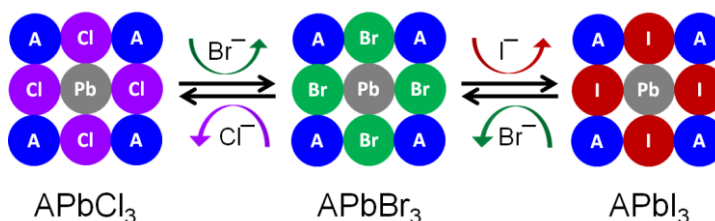


Figure 1.6 Schematic representation of halide exchange between metal-halide perovskite and different halide-source.

CsPbX_3 NCs show narrower size distributions than many other NCs, e.g., CuInS_2 , CuInSe_2 , $\text{Cu}_2\text{ZnSnS}_4$, InP , partly because of the distinct size and charge of cations and anions (Cs^+ , Pb^{2+} , and X^- ions) these metal-halide perovskite NCs consist of.^{12,68–71} The varying ion size and charge helps ensure proper order and homogeneity in the distribution of ions in the formation of respective NCs.¹² Furthermore, MHPs are more ionic in nature than chalcogenide and pnictide containing NCs, which plays a role in making MHPs

significantly less sensitive to surface states than chalcogenide and pnictide containing NCs.^{12,61,72}

In addition to the direct synthesis of MHPs with varying halide composition, these MHPs can readily undergo anion exchange reactions with various halide sources in solution to vary the halide composition post-synthesis. The ease of anion exchange reactions in MHPs is partly attributed to the dynamic surface ligand binding of oleylammonium halide and oleylammonium oleate,^{10,73} the ability of MHPs to retain their cubic structures at 40 °C due to the rigid cationic sublattice,^{28,66,74} and the high ionic diffusion afforded by the vacancy-assisted diffusion mechanism.^{28,66,75–77}

1.2.3 Surface Modification of Metal-halide Perovskite Nanocrystals and Thin Films

As the dimension of metal-halide perovskite are reduced to the nanometer range, the surface of these NCs is prone to be more reactive than that of their bulk counterparts. In addition, NCs tend to form undercoordinated B-site due to the stoichiometric imbalance used in the existing synthetic procedures.^{10,12} Thus, NCs with reactive surfaces and undercoordinated sites tend to coalesce into larger particles or dissolve into undesired by-products or starting precursors.^{10,55,78} In turn, they lose all their desired electrical and PL properties. Surface passivation comes into play through preventing these degradation pathways. To quench the reactive surface and thus stabilize the nanometer sized crystals surface modification is necessary.

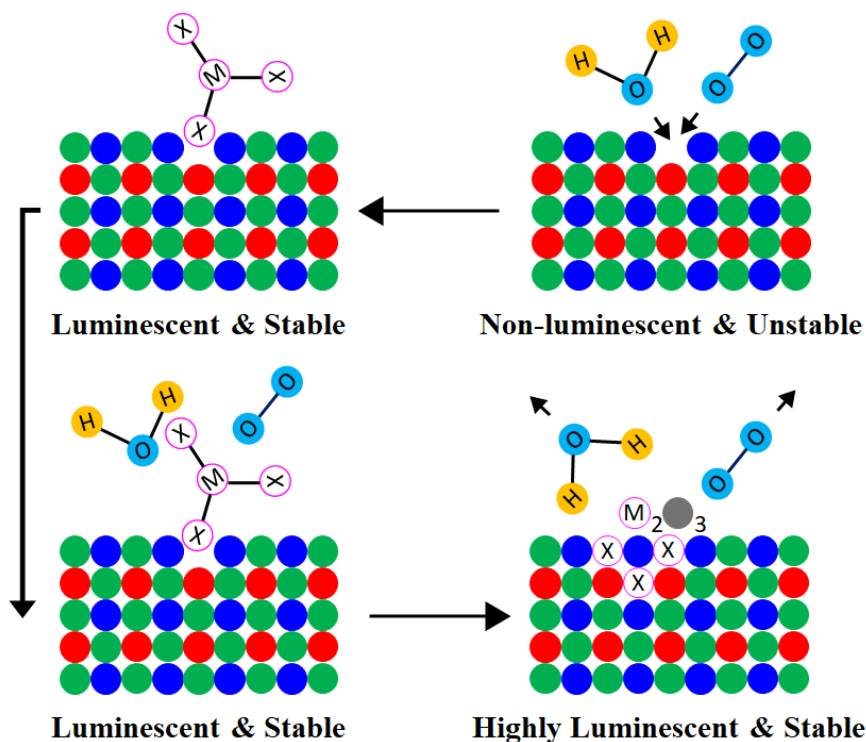


Figure 1.7 shows a schematic representation of roles of surface ligands in maintaining stability and PL properties of metal-halide perovskites.

Surface passivation can be performed on both NCs and thin films through including ligands in the precursor solution used for synthesis of NCs or thin films, or the MHPs can be treated post-synthetically through exposure to surface ligand solution. However, post-synthetic surface passivation is more popular than the in-situ synthesis route because post-treatment is more facile without altering the composition, size, and shape of the desired NCs/ thin films. Surface termination or passivation of both NCs and thin films have been investigated with different surface ligands with different binding functional groups including thiols (R/Ar-SH),^{14,36,79–86} trichlorosilane (R/Ar-SiCl₃),^{63,87–89} alkoxy silanes (R/Ar-Si(OR)₃),^{90–93} phosphonic acid (R/Ar-PO₃H₂),^{55,94–98} carboxylic acid (R/Ar-COOH),^{19,55,99–103} zwitterionic ligands (⁻OOC-R/Ar-NH₃⁺),^{16,104} ammonium ligands

(R/Ar-NH₃⁺),^{105–113} and other functional group containing or salt-like ligands (e.g., NaSCN, NH₄SCN, NaBF₄, NH₄BF₄, etc.).^{17,114}

Like NC surface modification, thin film surface modification has also great importance in terms of manipulating the materials and their applications in different optoelectronics. Surface modification of thin films can generally be done in two methods: vaporization methods and solution methods. In vaporization methods, ligands are usually thermally evaporated on the top surface of the fabricated perovskite films, whereas in the solution methods, ligands are dissolved in appropriate solvents and the ligand solution is usually spun-coated on the top of the perovskite layer as shown in **Figure 1.8a**.

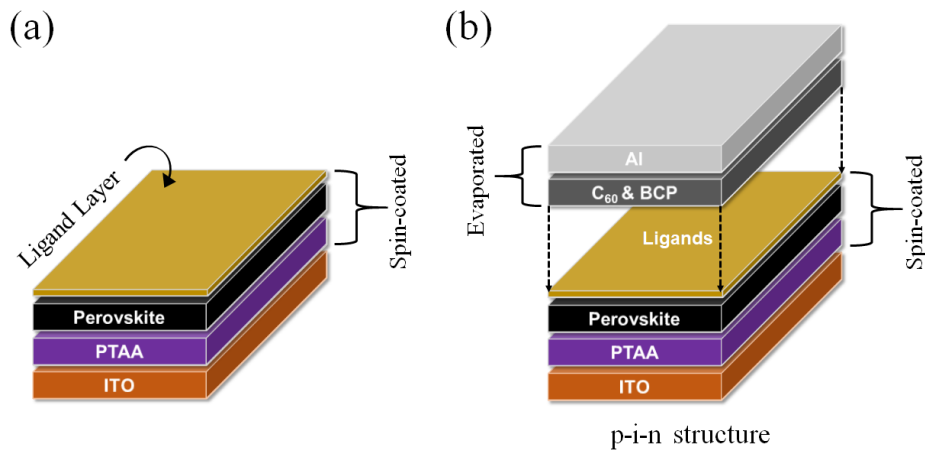


Figure 1.8 Schematic representation of **(a)** post-treatment of metal-halide perovskite thin films using surface ligands and **(b)** depicting surface modification of perovskite photovoltaics using an inter-layer of surface ligands between perovskite and electron transporting layer (ETL).

Application of surface ligands in optoelectronics, specially perovskite photovoltaics is very common because ligands are used to manipulate the device energetics to facilitate the charge transport properties of the devices. In p-i-n device structure, ligands

are applied at the interface between perovskite and electron transporting layer as shown in **Figure 1.8b**. In contrast, n-i-p structure, they are applied at the interface between perovskite and hole transporting layer.

Section 1.3 will discuss about application of metal-halide perovskite in photovoltaics: device structure, device materials, device physics, fabrication, testing, and characterization in details.

1.3 Applications of Metal-halide Perovskite

As the human population is increasing, demand and consumption of fossil fuels as well as resulting man-made environmental pollution from burning fossil fuels is increasing. To mitigate the energy crisis and reduce the impact of climate change due to the release of CO₂ from burning fossil fuels, dependence on renewable energy sources is indispensable. Over the past decade, dependence on non-renewable source has been reduced while increasing the dependence on renewable energy sources. Currently, one third of the global energy capacity is now based on renewable energy technologies which includes a 50% hydro, 24% wind, and 20% solar capacity. Solar energy is now fastest growing technology with an increase in capacity of 24% over 2018.^{115,116} Power generating capacity from solar energy technologies are booming up because of high power generating capacity, no pollution, and available light harvesting materials.

Among light harvesting materials, metal-halide perovskites have recently been receiving enormous attention because of soaring power conversion efficiencies of photovoltaics. However, CsPbX₃ perovskites are well-known as a class of perovskite materials from 1958 due to their photoconductivity nature, whereas the synthesis and crystal structures of MAPbX₃ were introduced in 1978. But the first time Br and I-based

MAPbX₃ perovskite was employed as a sensitizer to replace the common dye in a dye-sensitized solar cells by Kojima and his coworkers was 2009.²¹ The work principle of the perovskite photovoltaics they fabricated was similar to the dye-sensitized photovoltaics and PCE was 3.1% for Br-based perovskite and 3.8% for I-based perovskite. In a follow-up study, several groups pushed the frontiers of perovskite photovoltaics and made efforts to improve the PCE and stability of the PV devices. In one of the studies, Lee and his coworkers achieved a high PCE of up to 10.9% by fabricating MAPbI_{3-x}Cl_x perovskite PVs in 2012.¹¹⁷ Within a decade, the PCE of perovskite photovoltaics increases from 3.8% in 2009²¹ to more than 25.5% in 2020.¹¹⁸ This good performance was achieved with the metal-halide perovskites having tunable bandgap energies, E_{bg} of 1.43-1.86 eV.¹¹⁹⁻¹²² In addition, in fabricating solar cells, need of a decreased amount of metal-halide perovskite and solution-processability of perovskite for high throughput manufacturing of PVs make perovskites one of the important light absorbing materials for next generation optoelectronic devices compared to silicon.

Fabrication, testing, and characterization of metal-halide perovskite photovoltaics are relatively rigorous and require multiple steps. Fabrication of efficient PV devices requires the right choice of composition of the light absorber layer, charge extraction layers (hole transporting layers, HTLs and electron transporting layers, ETLs), and type of metal contacts. In fabrication of perovskite PV devices, the perovskite layer is sandwiched between HTLs and ETLs.¹²³ Depending on the stacking nature of charge extraction layers, photovoltaic devices generally are of two different structures. One is a planar regular (n-i-p) structure which is shown in **Figure 1.9a**,¹²³ and another is a planar inverted structure (p-i-n) which is shown in **Figure 1.9b**.¹²³ In a planar inverted structure of a photovoltaic

device, generally conductive metal, such as aluminum or copper is thermally evaporated over all the ETLs. In contrast, for a planar regular structure, generally a gold contact is thermally evaporated on the HTL.¹²³ This evaporated metal acts a cathode in the planar inverted structure of PV devices, whereas evaporated metal acts as an anode in the planar regular structure of the PV devices.¹²³

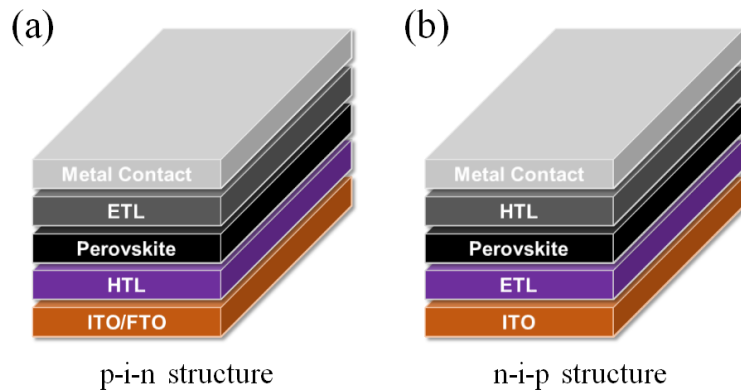


Figure 1.9 (a) p-i-n structure and (b) n-i-p structure of stacking layers in fabricated photovoltaic devices.

Performance of fabricated devices greatly depends on the energetics as depicted in **Figure 1.10a** and favorable charge transport properties of ETLs and HTLs.^{124–128} Ideal choice of these layers can minimize the loss of photogenerated charges. The most common HTLs are NiO, Poly(2,3-dihydrothieno-1,4-dioxin)-poly(styrenesulfonate) abbreviated to PEDOT:PSS, poly(triarylamine) abbreviated to PTAA, and N²,N²,N^{2'},N^{2'},N⁷,N⁷,N^{7'},N^{7'}-octakis(4-methoxyphenyl)-9,9'-spirobi[9H-fluorene]-2,2',7,7'-tetramine abbreviated to Spiro-OMeTAD, whereas common ETLs can be either organic or inorganic materials and

include C₆₀, Phenyl-C61-butyric acid methyl ester (PCBM), TiO₂, SnO₂ and so on. Over the ETL or HTL, a metal electrode is deposited to make a complete photovoltaic device.

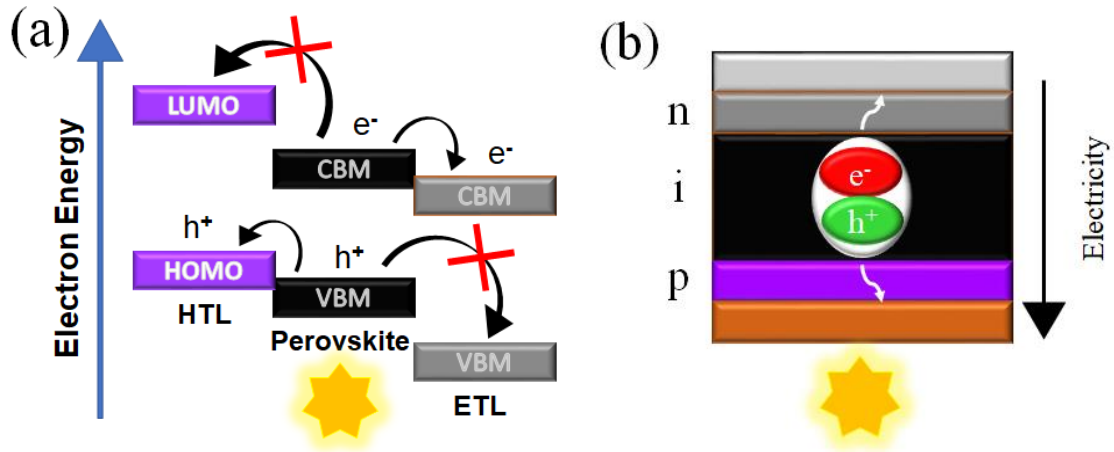


Figure 1.10 Schematic representation of (a) potential transport energetics between the perovskite layer and carrier extraction layers and (b) roles of carrier extraction layers.

When a photon of light hits the perovskite layer in the fabricated photovoltaic device, excitons are generated. The bound electrons and holes in the photogenerated excitons are separated to free charges by the carrier extraction layers and are collected to the opposite electrodes. And that is how electricity is generated. Photovoltaic devices were tested inside of a N₂-filled glove box using an ABET solar simulator at 100 mW*cm⁻² illumination (AM 1.5 G) in our lab. The solar intensity was adjusted using a calibrated photodiode (Thorlabs, FDS1010-CAL) with a KG3 Filter. To analyze the J-V curve, there are five parameters to characterize the performance of any photovoltaic devices. Five parameters: peak power (P_{max}), short-circuit current density (J_{sc}), open-circuit voltage

(V_{oc}), fill factor (FF), and power conversion efficiency (η).¹²⁹ All these parameters are determined from a J-V curve, shown in **Figure 1.11**.

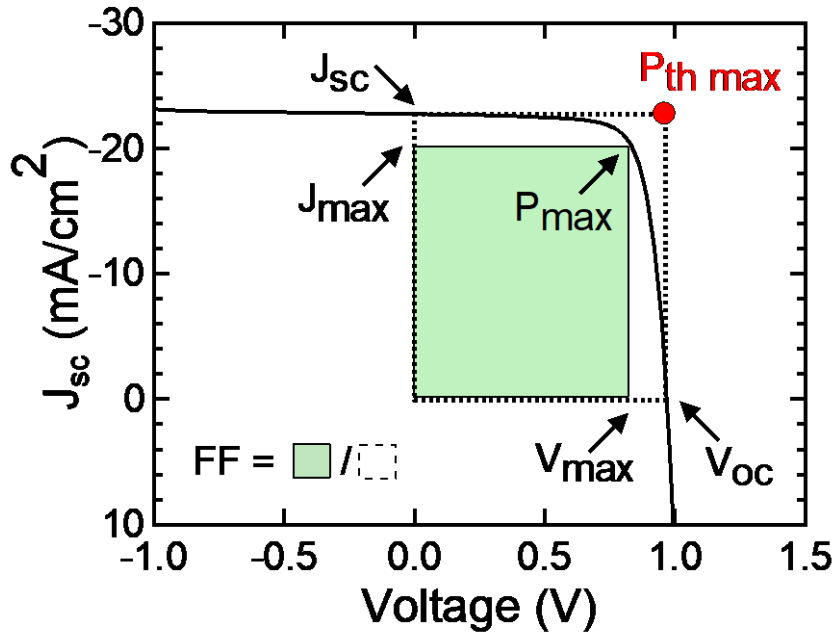


Figure 1.11 J-V characteristics of p-i-n heterojunction of a $\text{Cs}_{0.15}\text{FA}_{0.85}\text{PbI}_3$ photovoltaic device under 1 sun illumination performed in our lab.

One of the important parameters is the short-circuit current density, which is denoted by J_{sc} . It is the current at short circuit (0 V).¹²⁹ Generally, maximum current depends on the optical properties of the photovoltaics. Optical properties depend on optical absorption in the absorber layer and reflection on the absorber layer including absorption and reflections from other components in the device and interface effects. Another important parameter is the open-circuit voltage, which is denoted by V_{oc} . It is the voltage at which no current flows through the external circuit.¹²⁹ So, this is called the maximum voltage that a solar cell can deliver. It is the point where the rate of photogenerated charge-

carrier generation is equal to the recombination rate. Thus, reducing the rate of recombination leads to higher V_{oc} . The third important parameter is the Fill Factor, which is denoted by 'FF'. Fill factor is defined by the equation 1.1, the area ratio between the maximum power generated by a photovoltaic device and the product of V_{oc} with J_{sc} (called the theoretical max power point):¹²⁹

$$FF = \frac{P_{max}}{J_{sc}V_{oc}} = \frac{J_{max}V_{max}}{J_{sc}V_{oc}} \dots\dots\dots 1.1$$

Where, maximum power (P_{max}) is equal to $J_{max} \times V_{max}$. The last and most important parameter is the power conversion efficiency (PCE), which is defined by equation 1.2, the ratio between the maximum generated power and the incident power.

$$\eta = \frac{P_{max}}{I_{solar}} = \frac{J_{max}V_{max}}{I_{solar}} = \frac{(J_{sc}V_{oc})}{I_{solar}} \times FF \dots\dots\dots 1.2$$

In all the later chapters 2-5, original research work is discussed in details. And last chapter 6 summarizes this body of work with explaining the future research plan and overall career research.

CHAPTER 2. HALIDE EXCHANGE AND SURFACE TREATMENT OF METAL-HALIDE PEROVSKITE NANOCRYSTALS WITH ALKYLTRICHLOROSILANES

Adapted from “Uddin, M. A.; Calabro, R. L.; Kim, D. Y.; Graham, K. R. Halide Exchange and Surface Modification of Metal Halide Perovskite Nanocrystals with Alkyltrichlorosilanes. *Nanoscale* **2018**, *10* (35), 16919–16927. <https://doi.org/10.1039/C8NR04763D>” with permission.

2.1 Introduction

Lead-based metal-halide perovskites (MHPs) have the general chemical formula of $APbX_3$, where A is methylammonium, formamidinium, or Cs and X is Cl, Br, or I. Lead-based MHPs are direct bandgap semiconductors and have high Φ_{PL} of up to 80-100%.^{12,17,130,131} The electronic and optical properties of MHPs make these materials appealing for optoelectronic devices, such as photovoltaics (PVs),^{132–135} light emitting diodes (LEDs),^{26,27,136,137} lasers,^{8,138–140} and photodetectors (PDs).^{141–144} While the bulk materials are garnering significantly more interest for PVs, nanomaterials are more attractive for LEDs owing to their currently higher Φ_{PL} .

Metal-halide perovskite (MHP) NCs can be synthesized using low-cost precursors and relatively simple synthetic procedures.^{12,28} The most widely preferred method for synthesizing NCs is the hot-injection method, which was first used to synthesize highly luminescent and monodisperse colloidal $CsPbX_3$ NCs with 4-15 nm edge lengths.¹² Bandgap energies and PL emission spectra of these synthesized NCs are easily tunable over the entire visible spectral range of 410-700 nm with Φ_{PL} of up to 90% via adjusting the halide composition or taking advantage of quantum size-effects.¹² $CsPbX_3$ NCs show narrower size distributions than many other nanoparticles, e.g., $CuInS_2$, $CuInSe_2$, Cu_2ZnSnS_4 , partly because of the distinct size and charge of Pb^{2+} , Cs^+ , and X^- ions.^{12,68–71}

The varying ion size and charge helps ensure proper order and homogeneity in the distribution of ions in the formation of NCs.¹² Furthermore, MHPs are more ionic in nature than chalcogenide containing NCs, which plays a role in making these NCs significantly less sensitive to surface states than chalcogenide containing NCs.^{12,61,72}

In addition to the direct synthesis of NCs with varying halide composition, these NCs can readily undergo anion exchange reactions with various halide sources in solution to vary the halide composition in post-synthesis. The ease of anion exchange reactions in NCs is partly attributed to the dynamic surface ligand binding of oleylammonium halide and oleylammonium oleate,^{10,73} the ability of these NCs to retain their cubic structures at 40 °C due to the rigid cationic sublattice,^{28,66,74} and the high ionic diffusion afforded by the vacancy-assisted diffusion mechanism,^{28,66,75–77} In general, all that is needed for rapid anion exchange to occur is a source of halide ions.

Common halide ion sources for anion exchange have thus far included lithium halides (LiX),¹⁴² lead halides (PbX₂),^{28,145} oleyl/alkyl-ammonium halides (O/RAmX),^{28,146} alkyl-magnesium halides (Grignard reagents, RMgX),²⁸ and zinc halides (ZnX₂).⁶⁷ Through tuning the concentration of the halide exchange source, the PL maximum can be adjusted over the entire visible wavelength range with narrow full width at half maximum (FWHM) of 10-40 nm while maintaining Φ_{PL} of 1-90%.^{28,64,67,145–147} In addition to solution state anion exchange reactions, Guhrenz, et al. demonstrated that solid state anion exchange reactions between parent NCs and common NaX and KX salts occur and can be used to alter the NC composition and PL emission over a wide spectral range (400 nm to 700 nm).⁶⁴ In a less conventional approach, Parobek, et al. carried out anion exchange reactions via photoexcitation of CsPbX₃ NCs in a solution of dihalomethane in the absence of any

spontaneously reacting anion precursors.¹⁴⁷ However, all these methods of anion exchange reactions have their disadvantages that further complicate their synthesis and/or purification. For example, the inclusion of excess ligands in solution to help dissolve the anion exchange precursor,^{10,78} the need for laser irradiation,¹⁴⁷ or the need for post-exchange surface treatments of synthesized NCs to maintain stability.^{17,80}

A major issue that must be overcome to facilitate commercial applications for these NCs is their instability to atmospheric moisture, oxygen, and light illumination.^{148–152} One means of stabilizing colloidal NCs is to coat them with a stable and inert ligand shell.^{131,153–155} As it has been demonstrated that the most commonly used ligands with NCs, namely conjugate counterparts of oleylamine and oleic acid, bind in a highly dynamic fashion, these surface ligands are one of the reasons that NCs are typically unstable in solution. In addition, to keep the NCs as stable as possible in solution there must be an excess of oleylamine and oleic acid present. Surface ligands that have been used in place of oleylamine and oleic acid are thiols,^{80,156} thiocyanate salts,¹⁷ trioctylphosphine oxide,¹³ 2-adamantylammonium bromide,¹⁵⁷ and 3-(N,N-dimethyloctadecylammonio)propane sulfonate.¹⁶ Many of these ligands lead to higher Φ_{PL} , but few have been shown to result in colloidal NCs that are stable in solution for more than a few days. Furthermore, most of these ligands were applied to CsPbBr_3 ,^{13,17,80,154} $\text{CH}_3\text{NH}_3\text{PbBr}_3$,^{131,153,155,157} or CsPbI_3 NCs.¹⁵⁵ Herein, we report a simple, fast, and room temperature anion exchange reaction between host CsPbBr_3 NCs and alkyltrichlorosilanes. It was previously demonstrated that trichlorosilanes can be used to modify the surface of planar methylammonium lead iodide films,⁸⁸ but they have not yet been applied to perovskite NCs as surface modifiers and were not previously shown to result in halide exchange with the methylammonium lead iodide

films investigated. In our work, dodecyltrichlorosilane (DTS) is shown to react to form a hydrophobic shell around the NCs to keep them stable in solution for extended time periods, while the Cl^- is exchanged with Br^- in the CsPbBr_3 NCs to produce CsPbCl_3 NCs. In this process we suspect DTS primarily reacts with water molecules dissolved in the dispersion of NCs, while a smaller amount of DTS may also react with hydroxyl groups or water molecules on the NC surfaces, to form hydrochloric acid and dodecylsilols. These silols may then either react with undercoordinated surface lead atoms through the formation of a Pb-O bond, or react with other molecules of DTS to produce siloxane polymers and hydrochloric acid.¹⁵⁸ These liberated Cl^- ions participate in the anion exchange for Br^- , while oxygen atoms in the Si-O-Si groups of siloxane polymers may coordinate to the metal centers on the surface of CsPbCl_3 NCs. Similar to NCs coated with silsesquioxanes and SiO_2 ,^{131,155} we show that CsPbCl_3 NCs produced with DTS show significantly improved stability and increased Φ_{PL} over those of CsPbCl_3 NCs synthesized from alternative anion exchange methods reported in the literature.¹⁵⁹

2.2 Experimental Details

2.2.1 Materials and Chemicals

Cs_2CO_3 (99.9%, metal basis, Alfa Aesar), octadecene (ODE, tech. 90%, ACROS Organics), oleic acid (OA, tech.90%, Alfa Aesar), oleylamine (OLA, >40%, TCI), $\text{PbCl}_2/\text{PbBr}_2$ (puratronic 99.99%, metal basis, Alfa Aesar), dodecyltrichlorosilane (DTS, >97.0%, TCI), and hexane (ACS grade, BDH) were purchased and used as received.

2.2.2 Preparation of Cs-Oleate

0.1018 g Cs_2CO_3 , 5.0 mL ODE, and 0.39 mL OA were added to a 50 mL round bottom flask with side-arm glass stopcock. The flask was then heated to 120 °C and kept at 120 °C for 1 hour under vacuum. For dissolving Cs_2CO_3 completely and forming Cs-oleate, the reaction mixture in the flask was heated to and maintained at 150 °C under a N_2 environment for 1 hour while stirring the reaction mixture at 400 rpm.

2.2.3 Synthesis and Purification of CsPbX_3 Nanocrystals

For synthesizing CsPbCl_3 and CsPbBr_3 NCs, approximately 52.30 mg PbCl_2 (with 1 mL TOP) and 69 mg PbBr_2 , respectively, were added to 5 mL ODE in another 50 mL round bottom flask with side-arm glass stopcock for each type of NCs. Then the flask was heated to 120 °C and kept at 120 °C under vacuum while stirring the solution mixture at 400 rpm. After 15 minutes of the temperature reaching 120 °C, 1.5 mL OA and 1.5 mL OLA (for CsPbBr_3 NCs, 0.5 mL OA and 0.5 mL OLA were used) were injected in the flask successively. When the solution mixture in the flask turned clear yellow color, the flask was heated to 170 °C (for CsPbBr_3 NCs, it was 180 °C). To form NCs, the stirring speed in the PbCl_2 or PbBr_2 containing flask was reduced to 200 rpm and a preheated 0.4 mL Cs-oleate solution from the other flask was injected dropwise into the PbCl_2 or PbBr_2 containing flask with a 2 mL glass syringe. Following the Cs-oleate injection, the flask was immediately cooled down to room temperature by submerging the flask in an ice bath.

For storage and further studies of colloidal CsPbCl_3 and CsPbBr_3 NCs, 1.0 mL of crude solution in a 2 mL plastic vial was centrifuged at 10000 rpm for 5 minutes, and the colorful supernatant was discarded. Then NCs were dispersed in 300 μL hexane, and the solution was centrifuged at 10000 rpm for 5 minutes. Supernatant was collected and the pellet

discarded. Total volume of the stock NC dispersion was 2.7 mL (for CsPbBr₃ NCs, it was 1.8 mL).

2.2.4 **Synthesis of PbCl₂ assisted anion exchanged CsPbCl₃ NCs**

19.467 mg PbCl₂ along with 0.5 mL TOP was mixed with 2.5 mL ODE in a 50 mL 2-neck flask and kept under vacuum at 120 °C for more than 10 minutes while stirring at 400 rpm. OA and OLA (0.25 mL each) were injected at 120 °C under vacuum. For complete dissolution of PbCl₂, the temperature of the flask was raised to 170 °C for 10-15 minutes under a N₂ environment. After dissolution of PbCl₂, the temperature of the flask was lowered to 40 °C and CsPbBr₃ NCs (before adding, 155 μL of pure CsPbBr₃ NCs was diluted in 345 μL hexane) was injected in the dissolved PbCl₂ to initiate the anion exchange to form colloidal CsPbCl₃ NCs. Purification of this sample was also carried out in the same manner as that of colloidal CsPbX₃ NCs. Total volume of colloidal dispersion of CsPbCl₃ was 1.2 mL.

2.2.5 **Synthesis of DTS assisted anion exchanged CsPbCl₃ NCs**

Differing volumes of DTS, as specified in the text, were added to the initially purified colloidal CsPbBr₃ NC suspension. For FTIR and Raman samples, the crude solution was centrifuged at 10000 rpm for 30 minutes, and the supernatant was collected. The CsPbCl₃ NCs in the pellet were dispersed in hexane again. For time-dependent Φ_{PL} and lifetime measurements, DTS assisted anion exchanged NCs were used directly without further purification. For solid films and XRD Samples, 250 μL of stock dispersion of CsPbBr₃ NCs was diluted to 2.5 mL with hexane. Then 1 mL of DTS and 0.5 mL of distilled water were added to the NCs, respectively. Then 1 mL of crude dispersion of

CsPbCl₃ NCs was centrifuged at 10000 rpm for 30 minutes, and the supernatant was collected for preparing solid thin films. NCs in the pellet were re-dispersed in 1.2 mL of hexane and centrifuged again at 10000 rpm for 3 minutes, and the supernatant was collected and used for preparing XRD samples.

2.2.6 Stability Measurements

For PbCl₂ assisted anion exchanged NCs, 100 μ L deionized water was directly added to 3 mL of colloidal CsPbCl₃ NCs (absorbance values of ca. 0.1 at 350 nm). After inverting the capped cuvette several times, PL emission spectra were collected. A similar procedure was followed for DTS assisted anion exchanged CsPbCl₃ NCs. For thin films, DTS assisted anion exchanged NCs were deposited on a glass substrate by drop casting. After the sample was dry, time-dependent PL emission spectra were collected.

2.2.7 Characterization

Optical absorption spectra were collected using an Ocean Optics QE pro high-performance spectrometer with 80 ms integration time and 5 micron slit width. PL emission spectra were measured using a Lumina Fluorescence Spectrometer by Thermo Fisher Scientific with 20 ms integration time and 2.5 nm slit width (PL data in SI Figure 2.3.4 and 2.3.5 were collected with a Horiba Scientific Fluoromax Plus-C Fluorimeter with 1.25 and 0.5 nm slits for SI Figures 2.3.4c and 2.3.5b, respectively). For collecting PL data, NC dispersion were diluted in hexane to reach an optical absorbance of 0.05-0.1 (1.2 μ M*3-4 mL NC dispersion) at the excitation wavelength. PL emission spectra were collected by exciting the samples at 350 nm for colloidal CsPbCl₃ NCs and at 405 nm for colloidal

CsPbBr₃ NCs. For Φ_{PL} measurements, the NC dispersions were diluted in hexane to reach an optical absorbance of 0.05-0.1 at the excitation wavelength. The spectra were collected using a Horiba Scientific Fluoromax Plus-C Fluorimeter equipped with an integrating sphere by exciting the samples with a 350 nm excitation wavelength for CsPbCl₃ NCs and a 405 nm excitation wavelength for CsPbBr₃ NCs. Emission was scanned to include the Rayleigh scattering from the hexane solvent. Photoluminescence lifetimes were measured using a DeltaHubTM high throughput time correlated single photon counting (TCSPC) controller with an excitation wavelength of 393 nm generated by a pulsed NanoLED excitation source. Experimental PL lifetime results were fitted with exponential decay curves using Horiba Scientific Decay Analysis Software. FTIR data were obtained with a Thermo Scientific Nicolet IS50 FTIR Spectrometer equipped with a diamond ATR plate. A resolution of 4 cm⁻¹ and 64 scans were used in each measurement. Purified NCs were drop-cast on a glass slide and Raman spectra were obtained with a Thermo Scientific Raman Microscope DXR equipped with a 10x objective lens. Raman measurements were carried out with a laser power of 10 mW and an excitation wavelength of 532 nm. A resolution of 4 cm⁻¹ and 32 scans were used in each measurement. TEM samples were prepared on lacey carbon films supported by 300 mesh copper and TEM images were obtained using a JEOL 2010F operated at 200 kV. The X-ray diffraction patterns (θ - 2θ scans) were taken on a Bruker-AXS D8 DISCOVER diffractometer with Cu K α radiation ($\lambda = 1.5418 \text{ \AA}$) operating at 40 kV and 40 mA. Samples for XRD measurements were prepared by drop-casting perovskite NC dispersions on cleaned glass substrates and drying under vacuum.

2.3 Results and Discussion

The colloidal CsPbBr₃ NCs were synthesized by the hot-injection method described by Protesescu et al. with minor changes.¹² The NCs were purified through centrifugation, with complete procedures for synthesis and purification described in the experimental section. **Figure 2.1a** shows characteristic optical absorption and PL emission spectra of purified colloidal CsPbBr₃ NCs. The CsPbBr₃ NCs show excitonic absorption maxima at 505 nm and a PL emission maximum of 512 nm with FWHM of 17.4 nm, which is comparatively narrower than the previously reported values in the literature.^{10,13,146,157}

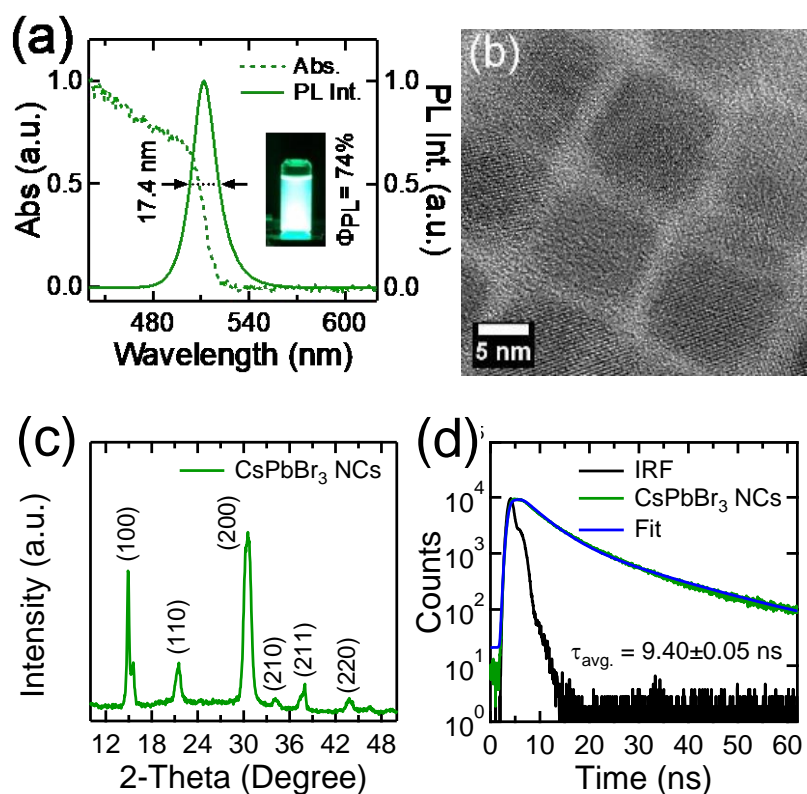


Figure 2.1 (a) Optical absorption and PL emission spectra (inset showing optical photograph of parent CsPbBr₃ NCs under a 365 nm UV lamp), (b) high resolution TEM image, (c) XRD patterns, and (d) PL lifetime decay of parent CsPbBr₃ NCs.

This narrower FWHM of the CsPbBr₃ NCs indicates that the synthesized NCs are highly monodisperse.^{10,13} The Φ_{PL} of the CsPbBr₃ NCs range from 39 to 74% and are dependent on the specific synthesis conditions. Particularly, the Φ_{PL} depends on the stoichiometric ratio of PbBr₂ and Cs₂CO₃ as well as the reaction quenching time. The same batch of purified CsPbBr₃ NCs with an initial Φ_{PL} of 74% was used for the anion exchange reaction data reported herein. The transmission electron microscope (TEM) images and X-ray diffraction (XRD) patterns of the as-synthesized CsPbBr₃ NCs shown in **Figure 2.1b and c** indicates that the NCs are cubic in shape with edge length and squareness of 11.30 ± 1.70 nm and 0.90 ± 0.12 , respectively.^{10,72,146,160} As shown in **Figure 2.1d**, these CsPbBr₃ NCs have average radiative lifetimes of 9.4 ± 0.1 ns, which is in the typical range for colloidal CsPbBr₃ NCs.^{12,17,161}

Parent CsPbBr₃ NCs were directly transformed to colloidal CsPbCl_xBr_{3-x} NCs upon addition of DTS to a solution of parent CsPbBr₃ NCs, as depicted in **Figure 2.2a** and indicated by the UV-vis absorbance and PL emission spectra presented in **Figure 2.2b and c**.

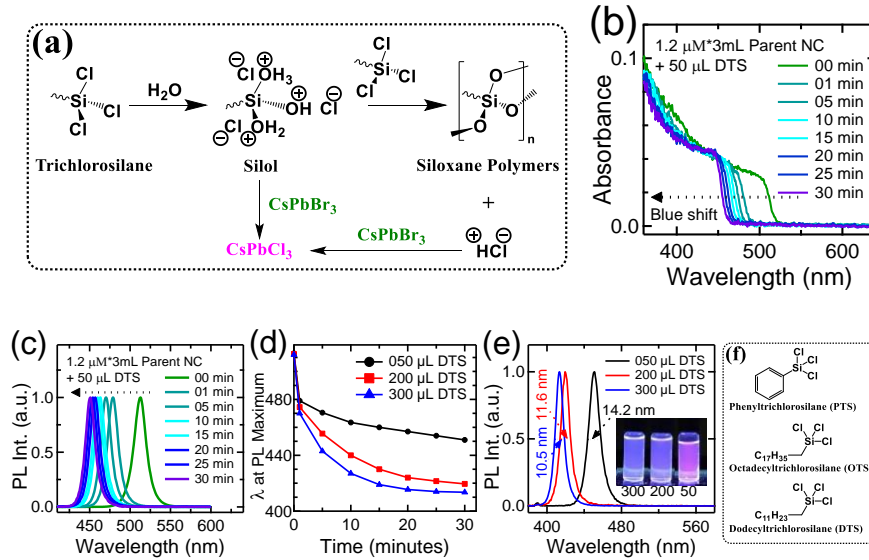


Figure 2.2 (a) A proposed mechanism of synthesizing DTS assisted anion exchanged NCs; (b, c) time-dependent UV-Vis absorbance (nonnormalized) and normalized PL emission spectra of DTS assisted anion exchanged NCs at 5 minute intervals; (d) time-dependent PL emission spectra showing the PL emission maxima at 5 minute intervals; (e) PL emission spectra of DTS assisted anion exchanged NCs after 30 minutes of addition of 50, 200, and 300 μL of DTS to the 3 mL colloidal solution of parent NCs at room temperature (inset shows optical photographs of 50, 200, and 300 μL DTS assisted anion exchanged NCs under a 365 nm UV lamp); and (f) a list of trichlorosilanes used in this study.

Figure 2.2b and c show that upon addition of 50 μL DTS to a 3 mL dispersion of CsPbBr_3 NCs in hexane (concentration ca. 1.2 μM), the first excitonic absorption maxima and PL maximum blue shift from 508 nm to 446 nm and 512 nm to 451 nm, respectively, within 30 minutes. Figure 2.2d shows that as the concentration of DTS in solution increases, the rate of reaction increases and the PL maximum plateaus at shorter wavelengths. The PL emission peaks maintain narrow FWHMs of 10.5 to 14.2 nm for all DTS concentrations investigated, as evident in Figure 2.2e, which agrees with previously reported data for CsPbCl_3 and $\text{CsPbCl}_x\text{Br}_{3-x}$.^{28,145,146} Upon anion exchange reactions the PL intensity and Φ_{PL} decrease, which is in agreement with the lower Φ_{PL} previously observed for CsPbCl_3 relative to CsPbBr_3 . Figure 2.2d and e show that the final halide composition

depends on the concentration of DTS added to the solution of CsPbBr₃ NCs. Other trichlorosilanes listed in **Figure 2.2f** were also investigated and found to yield similar results, which suggests that this procedure should be applicable to any trichlorosilane containing molecule.

To compare our method of synthesizing CsPbCl₃ NCs with other synthetic methods, we also performed the anion exchange using PbCl₂ as the Cl⁻ source using hot injection method. **Figure 2.3** shows that the CsPbCl₃ NCs synthesized with DTS as the chloride source display similar absorption and PL spectra as those synthesized using PbCl₂ as the halide source, which is a commonly used Cl⁻ source for anion exchange.^{28,146} The PL maxima for the CsPbCl₃ NCs produced through Cl⁻ exchange with DTS and PbCl₂ fall at 413 and 409 nm, respectively, and display identical FWHMs of 10.5 nm. These values are comparable to the 410 nm PL maximum reported for pure CsPbCl₃ NCs,¹² which suggests that after 30 minutes the exchange reaction is nearly complete.

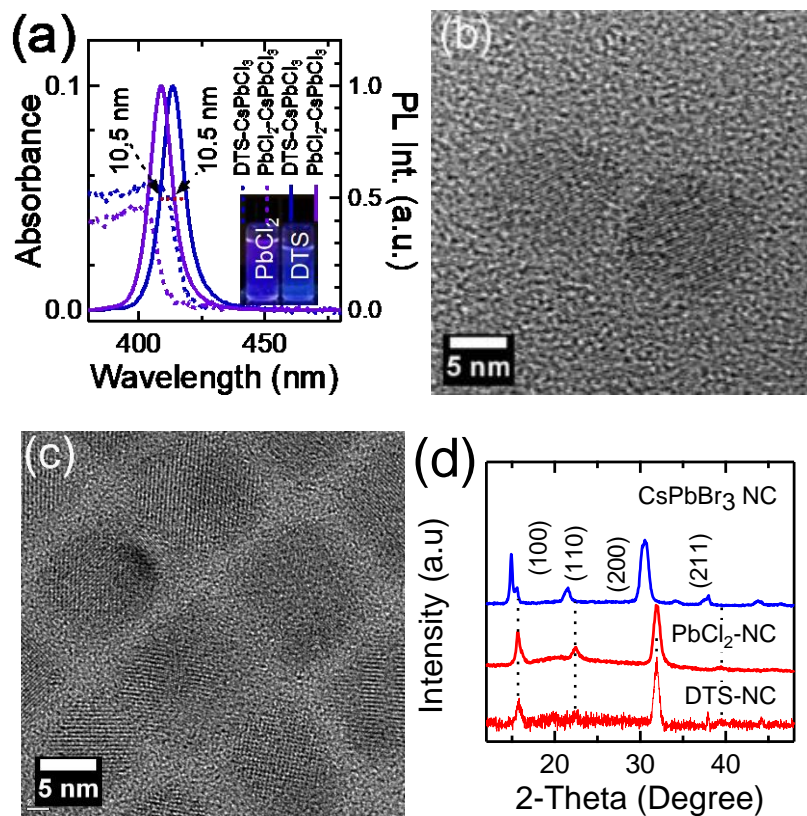


Figure 2.3 (a) Optical absorption (dashed lines) and PL emission (solid lines) spectra of DTS assisted anion exchanged CsPbCl₃ NCs (blue, 300 μL DTS + 1.2 μM*3 mL parent NC dispersion) and PbCl₂ assisted anion exchanged CsPbCl₃ NCs (violet). Inset in 2.3a shows optical photographs of PbCl₂ and 300 μL DTS assisted anion exchanged NCs under a 365 nm UV lamp; HR-TEM images of (b) 50 μL DTS assisted anion exchanged CsPbCl₃ NCs; (c) PbCl₂ assisted anion exchanged CsPbCl₃ NCs; and (d) comparison of XRD patterns of DTS and PbCl₂ assisted anion exchanged NCs.

TEM images and XRD patterns were collected on both DTS and PbCl₂ assisted anion exchanged CsPbCl₃ NCs, as shown in **Figures 2.3b-d**. The XRD spectra are consistent with the cubic perovskite structure ($Pm\bar{3}m$ space group) of CsPbCl₃ NCs.⁷² Both DTS and PbCl₂ assisted anion exchanged NCs have nearly identical average crystal sizes and squareness (9.7 ± 1.6 nm, 9.6 ± 1.5 nm, and 0.90 ± 0.11 , respectively). The nearly identical sizes and shapes of both DTS and PbCl₂ assisted anion exchanged NCs indicates that the Cl⁻ source does not affect the shape and crystal structure of these NCs. Furthermore, with

both Cl^- sources the NCs contract slightly in size while the shape remains nearly identical to the parent CsPbBr_3 NCs, which is alike to the typical halide-precursor assisted anion exchanged NCs reported in the literature.^{28,64,145}

Improving the stability of CsPbBr_3 NCs through the use of surface ligands has been a subject of recent interest,^{162–164} however, CsPbCl_3 NCs have received much less attention in this regard. With using DTS for the Cl source, we expected that a siloxane coating would stabilize the NCs. Indeed, DTS assisted anion exchanged NCs show large enhancements in stability and dispersibility over PbCl_2 exchanged NCs.

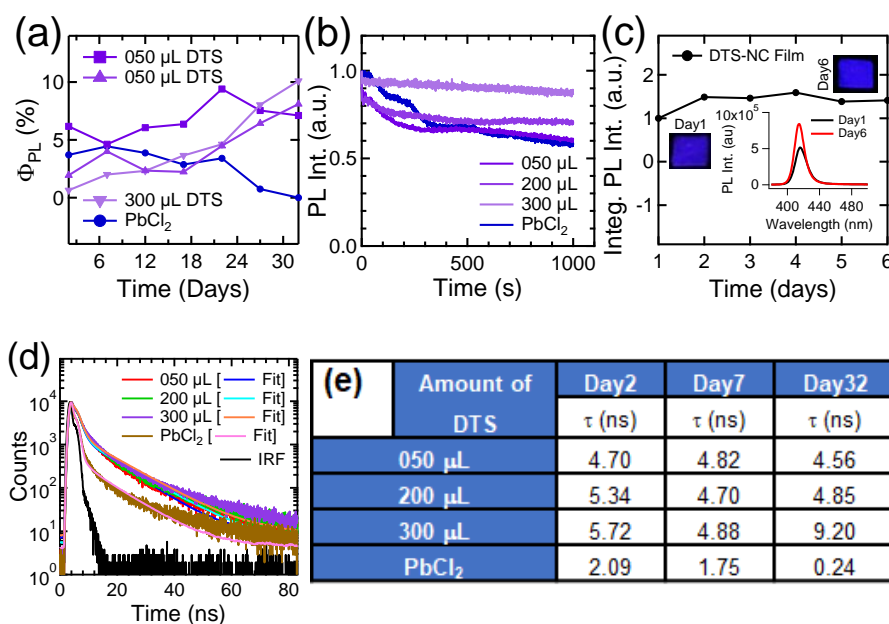


Figure 2.4 (a) Time-dependent PLQYs of DTS and PbCl_2 assisted anion exchanged NCs stored in capped vials in ambient air; (b) PL intensity of PbCl_2 assisted anion exchanged NCs, and DTS assisted anion exchanged NCs as a function of time showing photobleaching; (c) time-dependent PL emission spectra showing stability of solid thin film prepared from DTS assisted anion exchanged CsPbCl_3 NCs via drop casting; (d) PL lifetime decays 2 days after anion exchange and the instrumental response function (IRF); and table showing time-dependent average lifetimes, τ of DTS assisted anion exchanged NCs and PbCl_2 assisted anion exchanged CsPbCl_3 NCs on a day-scale.

Figure 2.4a shows that the Φ_{PL} of DTS exchanged NCs increase from starting values of 1-6% to final values of 7-10% (record 12% for a different experimental run) over a period of 1 month with storage in capped vials in ambient atmosphere. By contrast, the Φ_{PL} of PbCl_2 assisted anion exchanged NCs decrease to 0% over this same time frame. In addition, DTS assisted anion exchanged NCs show suppressed photobleaching compared to the PbCl_2 assisted anion exchanged NCs, as shown in **Figure 2.4b**. In addition, we did not observe any aggregation of DTS assisted anion exchanged NCs after one month of storage in ambient air. The stability of solid films of DTS exchanged NCs on a glass substrate were also investigated, as shown in **Figure 2.4c**. We observed similar results as for the solution measurements, i.e., the PL intensity of the DTS exchanged NC films increased up to 41% after storage in air for 6 days.

We further investigated the PL properties through measuring the PL lifetimes at varying times after anion exchange, as shown in **Figure 2.3d and e**. The PL lifetime decays of DTS and PbCl_2 assisted anion exchanged NCs are best fit with bi-exponential decays, and the average lifetimes of the NCs are within the range of previously reported values.^{12,17,165,166} Two different decay pathways in the PL lifetime decays likely arise from states within the bandgap, which may arise from surface states and/or structural distortions.^{12,17,74,165–168} We find that the PL lifetimes of the $\text{CsPbCl}_x\text{Br}_{3-x}$ NCs produced from DTS as the Cl^- source are 2 to 2.5 times longer than those with PbCl_2 as the Cl^- source at 2 and 7 days after synthesis, with values of *ca.* 2 ns for PbCl_2 and *ca.* 5 ns for DTS. We hypothesize that this longer lifetime for the DTS assisted anion exchanged NCs arises from coordination of oxygen from the O-Si groups and passivation by excess halide ions to undercoordinated surface Pb atoms. After 32 days, the Φ_{PL} of the CsPbCl_3 NCs produced

from PbCl_2 has decreased to *ca.* 0.1%, and correspondingly the PL lifetime has decreased to only 0.24 ns. By contrast, after 32 days the Φ_{PL} of the DTS exchanged NCs either remain similar to their values on day 7 (with 50 and 200 μL DTS) or show further increased lifetimes of 9.2 ns (with 300 μL DTS) as shown in **Figure 2.4e**. These PL lifetimes further support that DTS significantly improves NC stability.

To further investigate the stability of the NCs in the presence of water, 100 μL of deionized H_2O was directly added to 1.2 μM *3 mL of a colloidal solution of DTS exchanged NCs 20 minutes after initial DTS addition. As is evident in **Figure 2.5a and b**, the addition of water causes the PL intensity of the NCs with DTS to increase by a factor of more than two over 30 minutes; whereas, the PL intensity of the NCs with PbCl_2 decreases by 90% over 30 minutes.

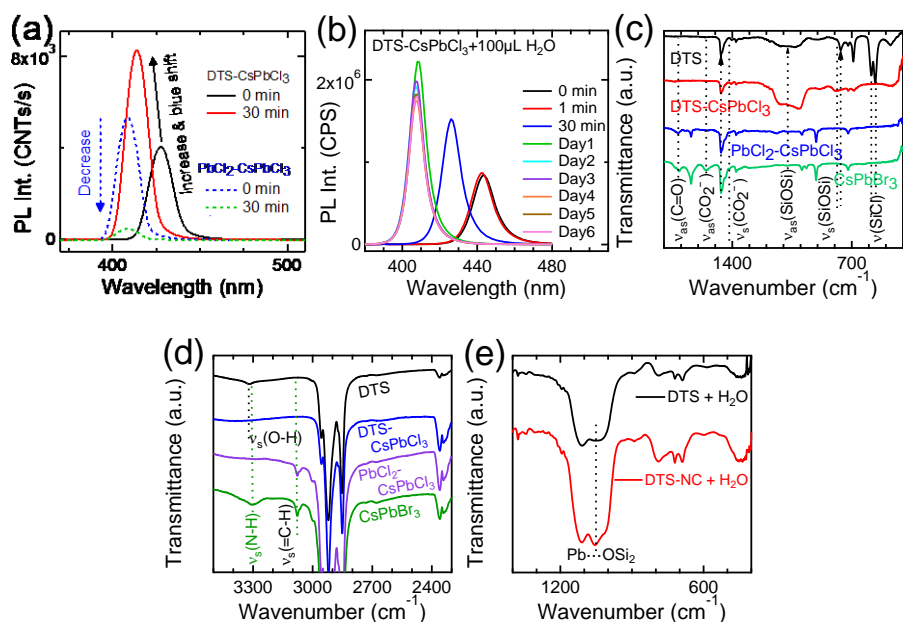


Figure 2.5 (a) PL spectra changes upon adding 100 μL of water to 1.2 μM *3 mL of DTS and PbCl_2 assisted anion exchanged NCs in hexane; (b) time-dependent PL emission spectra showing stability of DTS assisted anion exchange CsPbCl_3 NCs over days in exposure of 100 μL distilled water to 1.2 μM *3 mL colloidal dispersion of DTS assisted anion exchanged CsPbCl_3 NCs; (c, d) FTIR spectra of pure DTS, DTS assisted anion exchanged NCs, PbCl_2 assisted anion exchanged NCs, and host NCs; and (e) FT-IR spectra of DTS with added water and DTS exchanged NCs with added water showing the Si-O stretching mode and a peak that is suspected to arise from Si-O groups where the oxygen is coordinated with Pb.

The hypsochromic PL shift for the DTS exchanged NCs is suspected to result from the additional HCl generated upon water addition, i.e., the unreacted DTS molecules react with water following the mechanism in **Figure 2.2a**. The higher Cl^- concentration in solution results in further halide exchange to shift the equilibria closer to pure CsPbCl_3 NCs. The enhanced PL intensity may be attributed to the increased amount of siloxane in solution that is available to coordinate and passivate the NC surface; or, this PL increase may result from the increased concentration of Cl^- in solution, which may help to passivate defect states on the NC surfaces (e.g., undercoordinated Pb). Longer term stability measurements, as displayed in **Figure 2.5b** for a separate batch of DTS exchanged NCs,

show that the PL emission intensity reaches a maximum 1 day after water addition and decreases from that maximum by less than 20% after 6 days.

Fourier transform infrared (FTIR) absorbance and Raman scattering were used to further investigate the reactions of DTS and CsPbBr₃ NCs. **Figure 2.5c** shows the FTIR spectra of the NCs, associated organic molecules, and their conjugate counterparts. The main observations from this data are that the DTS that remains in the NC solution following purification is completely converted to siloxane, the Si-O-Si groups appear to coordinate to the NC surface, and DTS displaces the oleylamine/oleylammonium ion and oleic acid/oleate ion ligands from the NC surface as symmetric stretching modes of N-H and =C-H as well as asymmetric modes of COOH and COO⁻ ion are disappeared as shown in **Figure 2.5c and d**. In DTS assisted anion exchanged NCs, we observe the disappearance of the Si-Cl bands at 562 and 585 cm⁻¹ present in pure DTS and an increase in the Si-O-Si anti-symmetric stretching modes at ~970-1200 cm⁻¹.^{131,169,170} In addition, the absence of the Si-OH peak at 924 cm⁻¹ in the dispersion of CsPbCl₃ NCs supports that the DTS molecules form siloxane polymers or Si-O-Pb bonds, as opposed to silols.^{131,171} The symmetric stretching mode of Si-O-Si groups in DTS assisted anion exchanged NCs appears at 788 cm⁻¹, which is shifted from the sharp band at 765 cm⁻¹ of Si-O-Si groups in the siloxane polymers formed from pure DTS upon air exposure.^{131,170} This peak shift may potentially arise from the Si-O-Si groups coordinating to the Pb centers on the NC surfaces. Another peak appears at 1054 cm⁻¹ in DTS assisted anion exchanged NCs, shown in **Figure 2.5e**, which we suspect is due to Si-O-Si coordinated to Pb on the NC surface.

2.4 Conclusion

Perovskite NCs are attractive for light emitting applications, and this work provides an important step in developing methods for synthesizing highly luminescent and stable blue-emitting perovskite NCs. The alkyltrichlorosilane assisted anion exchange reactions demonstrated have several advantages compared to methods reported in the literature, including shorter reaction times, room temperature synthesis, no need for excess ligands or any exchange precursor work up, and the ability of DTS to act as both an anion source and surface modifier. The siloxanes also passivate the NC surfaces and stabilize the NCs, resulting in increased Φ_{PL} and high stability upon both storage in air and exposure to water. This discovery paves the way towards using a number of trichlorosilane derivatives as surface modifiers to further control and enhance the optical properties, electronic properties, and stability of chloride containing perovskite NCs.

CHAPTER 3. MECHANISTIC EXPLORATION OF DODECANETHIOL TREATED COLLOIDAL CESIUM LEAD BROMIDE NANOCRYSTALS WITH PHOTOLUMINESCENCE QUANTUM YIELDS REACHING NEAR 100%

Adapted from “Uddin, M. A.; Mobley, J. K.; Masud, A. Al; Liu, T.; Calabro, R. L.; Kim, D.-Y.; Richards, C. I.; Graham, K. R. Mechanistic Exploration of Dodecanethiol Treated Colloidal CsPbBr₃ Nanocrystals With Photoluminescence Quantum Yields Reaching Near 100%. *J. Phys. Chem. C* **2019**, *123* (29), 18103–18112. <https://doi.org/10.1021/acs.jpcc.9b05612>” with permission.

3.1 Introduction

Both inorganic and organic metal-halide perovskite materials, from colloidal NCs to polycrystalline thin films, are drawing much attention in the field of optoelectronics. These materials display attractive optical and electronic properties, such as tunable direct band gaps,^{8,9} high absorption coefficients,¹⁰ low exciton binding energies,^{166,172} relatively high electron and hole mobilities,¹¹ narrow emission line-widths,¹² and Φ_{PL} .^{13,16,17,173} Much of the initial excitement around organic metal-halide perovskites focused on their application in photovoltaics (PVs) based on thin polycrystalline films,^{117,174} but now colloidal metal-halide perovskite NC are a subject of intense interest due to their highly desirable emission properties for light emitting applications. For example, narrow emission line-widths of 16-25 nm with Φ_{PL} of 95% have been reported for as-synthesized CsPbBr₃ NCs in ligand mediated syntheses,^{13,16,17} with increases up to 100% through post-synthetic modification,^{17,173} and the emission wavelength can be readily adjusted by varying the halide composition between Cl, Br, and I.¹² Owing to their desirable optoelectronic properties, colloidal metal-halide perovskite NCs have been used in PVs,^{134,135,175} light emitting diodes,^{26,27,137} photodetectors,^{142,176} and lasers.^{8,138,139} Although green emitting

CsPbBr₃ NCs have reached Φ_{PL} of unity, they lack long-term colloidal stability and the sensitivity to synthesis conditions leads to a wide variation in reported Φ_{PL} values.^{10,17,78,114}

Synthesis of colloidal CsPbX₃ NCs with tunable energy gaps and PL emission spanning the visible spectrum was first reported using the hot-injection method,¹² and later followed by reports of lower temperature recrystallization based synthetic techniques.^{177,178} Synthesis and post-synthetic compositional tuning of colloidal CsPbX₃ NCs is comparatively facile,^{64,67,142,146,147,159} but maintaining stable optical properties of colloidal CsPbX₃ NCs is a huge challenge because the parent ligands are highly labile.^{10,16,78} Consequently, synthesized colloidal CsPbBr₃ NCs lose their colloidal stability, structural integrity, and PL emission intensity due to aging or dispersion of NCs in polar solvents.^{10,13,16,17,78,80,179} Commonly, purification of the NCs is limited so as to maintain a reasonable concentration of unbound ligands in the NC dispersion that can readily replace desorbed surface ligands.¹⁰ These excess ligands in the NC dispersion are helpful for maintaining colloidal stability and passivating surface defect states, but in optoelectronic device applications these excess ligands will limit charge transport. Thus, identification of strongly bound surface ligands that lead to high Φ_{PL} and stable NCs remains a priority.

Colloidal CsPbBr₃ NCs are highly defect-tolerant owing to their ionic nature;^{28,61} however, defect states with low formation energies in as-synthesized colloidal CsPbBr₃ NCs are still present and limit the Φ_{PL} from reaching unity.¹² A number of both donor and acceptor defect states may appear,^{12,180} with synthetic conditions influencing the dominant defect states that form. Recent work has suggested that the most detrimental commonly observed defect states in CsPbX₃ NCs are halide vacancies at the surface, which lead to undercoordinated surface Pb atoms.^{55,56} In CsPbBr₃ NCs, the surface bromide vacancies

result in shallow electron traps, and passivation or elimination of these shallow traps is suspected to play a primary role in enhancing Φ_{PL} . Higher dimensional defects can also be harmful, such as the precipitation of metallic Pb particles on the NC surface.^{17,60}

There is an ongoing quest to reduce the number of harmful defects present in CsPbX₃ NCs through varying the synthetic conditions or post-synthetic chemical treatments.^{17,78} For example, several novel synthetic routes use separate sources for all three precursors,^{72,181,182} which allows CsPbX₃ NCs to be produced with varying halide compositions and high Φ_{PL} . Surface ligands are also extremely important for creating highly emissive and stable CsPbX₃ NCs. In the most common synthetic routes both a carboxylic acid and an amine are necessary to stabilize the NCs, as these ligands bind as an ion pair consisting of an alkylammonium and an alkylcarboxylate.¹⁰ Adding additional surface ligands to the precursor solution can produce more stable CsPbX₃ NCs with high Φ_{PL} . For example, tri-n-butylphosphine (PBu₃), tri-n-octylphosphine oxide (TOPO), primary amines (L-type ligands),²⁰ (3-aminopropyl)triethoxysilane (APS),¹⁸³ and 3-(N,N-dimethyloctadecylammonio)-propanesulfonate (a sulfobetaine) were shown to enhance PL properties of CsPbX₃ NCs in ligand mediated syntheses.^{13,16,184}

Post-synthetic treatments also provide a means of improving PL properties and stability, with an advantage of being able to manipulate the surface chemistry without re-optimizing the synthetic conditions for each surface ligand. Ligands that have been observed to improve the Φ_{PL} when applied in a post-synthetic treatment include thiocyanate salts,¹⁷ thiols,⁸⁰ tetrafluoroborate salts,¹¹⁴ alkyltrichlorosilanes,⁶³ aminopropyltriethoxysilane,¹⁸⁵ phosphonates,⁵⁵ sulfonates,⁵⁵ trialkylphosphines,^{55,184} carboxylates,⁵⁵ and di-dodecyldimethylammonium bromide.¹⁸⁶ Koscher and coworkers

demonstrated that post-synthetic treatments of colloidal CsPbBr₃ NCs by thiocyanate salts improved Φ_{PL} to near 100% due to the removal of shallow electron traps within the band gap.¹⁷ Ruan and coworkers showed that 1-octanethiol can passivate surface defects and enhance the PL intensity of the NCs in post-synthetic surface treatment when applied in a multistep ligand exchange and using a Pb²⁺ ion filling process.⁸⁰ By contrast to the increased PL intensity observed by Ruan, et al., Liu, et al. observed that thiols, and particularly dithiols, can lead to decreased PL intensities when amines are present due to the degradation of CsPbBr₃ NCs to Cs₄PbBr₆ NCs.⁸¹ Currently, few surface ligands produce NCs with long-term stability while maintaining high Φ_{PL} .

Through experimental and theoretical means the community is beginning to develop an understanding of how different defect states, surface states, and surface ligands influence the optical properties, electronic properties, and stability of these metal-halide perovskites. Further building this understanding will be necessary to enable the future design of novel metal-halide perovskite nanomaterials with targeted properties to enable high-performance applications. In this work, we present a systematic investigation of how various surface ligands influence the stability and Φ_{PL} of colloidal CsPbBr₃ NCs. We find that thiols, largely through formation of thioethers and likely thiolates, lead to near unity Φ_{PL} and highly stable CsPbBr₃ NCs. The improvement in Φ_{PL} observed upon thiol treatment is attributed to thioether and/or thiolate coordination to surface lead atoms and inhibited formation of metallic Pb particles, while the improved stability is attributed to the stronger binding affinity of thioethers and thiolates relative to carboxylates. Thioether formation and NC surface modification is hypothesized to be photocatalyzed by the

CsPbBr₃ NCs, as exposure to blue or UV light in the presence of the NCs is shown to rapidly accelerate thioether formation and Φ_{PL} improvement.

3.2 Experimental Details

3.2.1 Materials and Chemicals

Cs₂CO₃ (99.9%, metal basis, Alfa Aesar), octadecene (ODE, tech. 90%, ACROS Organics), oleic acid (OA, tech. 90%, Alfa Aesar), oleylamine (OLA, >40%, TCI), CsBr and PbBr₂ (puratronic 99.99%, metals basis, Alfa Aesar), hexane (ACS grade, BDH), anhydrous toluene (Tol, 99.8%, Alfa Aesar), dimethyl sulfoxide (DMSO, 99.9%, SeccoSolv[®]), N,N-dimethylmethanamide (DMF, 99.9%, SeccoSolv[®]), 1-butanethiol (BT, >97%, TCI), 1-octanethiol (OT, >95%, TCI), 1-dodecanethiol (DDT, >95%, TCI), NH₄SCN (99.99%, Sigma-Aldrich), tetradecyldimethyl(3-sulfopropyl)ammonium hydroxide inner salt (SB, >98%, TCI), tri-n-octylphosphine oxide (TOPO, 98%, Alfa Aesar), tri-n-octylphosphine (TOP, ≥97%, Alfa Aesar), sodium dodecyl sulfate (SDS, ≥98.5%, Sigma-Aldrich), and coumarin 153 (99%, Sigma-Aldrich) were purchased and used as received.

3.2.2 Synthesis of CsPbBr₃ Nanocrystals

Synthesis and Purification of CsPbBr₃ nanocrystals were carried out following the similar procedure discussed in 2.2.2 and 2.2.3 sections in **Chapter 2**.

3.2.3 Modification and Purification of CsPbBr₃ NCs For Fourier Transform Infrared (FTIR), X-Ray Photoelectron Spectroscopy (XPS), and ¹H Nuclear Magnetic Resonance (NMR) Studies

40.0 μmoles of DDT were directly added to 100 μL of purified crude NC dispersion (48 nmoles). 30 minutes later, the NC dispersion was centrifuged at 10000 rpm for 30 minutes. Supernatant was discarded and DDT-NCs were dispersed in 1.5 mL of hexane for further studies. To avoid aggregation of DDT-NCs in this process, the DDT-NC dispersion was sonicated for 10-20 seconds.

3.2.4 Preparation of CsPbBr₃ Bulk Thin Films for XPS Measurements

35 wt% (Cs/Pb = 0.25), 38 wt% (Cs/Pb = 0.50), and 28 wt% (Cs/Pb = 1.00) CsPbBr₃ solutions were prepared from a mixture of CsBr and PbBr₂ in a mixture of DMSO and DMF in a volume ratio of 4:1. The mixture was stirred at 1000 rpm at 70 °C over night to get a clear solution. Concentration of the Cs/Pb = 1.00 solution is lower because of the low solubility of CsBr. Even with the reduced concentration, the Cs/Pb = 1.00 solution had to be heated to 180 °C for precursor dissolution. Before depositing perovskite solution on ITO, ITO substrates were cleaned with successive sonication in a detergent solution, deionized (DI) water, acetone, and isopropanol baths for 10 minutes. The substrates were then treated with UV-ozone for 10 minutes. In the next step, 100 μL of perovskite solution was spin-coated on the cleaned ITO substrate at 100 rpm for 5s followed by 3000 rpm for 80s. After spinning for 15s, 200 μL of degassed toluene as an antisolvent was drop-cast to promote formation of a smooth and uniform thin film. Then the CsPbBr₃ films were annealed at 100 °C on a preheated hot plate. After 5 minutes of annealing, the films were

cooled down to room temperature. When the films were at room temperature, 200 μL of a ligand solution (made from DEE, DDT/DOS, and toluene in a molar ratio of 1:0.1:5.52) was drop-cast on the perovskite film with the same spinning rate. After this last step, the perovskite film was rinsed with 200 μL of degassed toluene 3 times with the same spinning rate. Film fabrication and solution preparation were done in an N_2 filled glove box (typically <0.1 ppm O_2 and H_2O). The films were directly loaded into the XPS analysis system without air exposure.

3.2.5 Absorbance

Optical absorption spectra were collected using the same conditions described in **section 2.2.7**. Optical absorption spectra were also obtained using a Thermo Scientific Evolution 201 UV-Visible Spectrophotometer with 100 ms integration time and 2 nm slit widths.

3.2.6 Photoluminescence

3.2.6.1 Measured Using Fluorimeter

PL emission spectra were collected using the same instruments and conditions described in **section 2.2.7**. But for this project, to the 1.2 μL *4 mL NC dispersion, 14.0 to 23.0 μmoles of surface ligand were added during the time-dependent PL measurements. Minimal variation in PL properties were observed when the surface ligand concentrations were adjusted within this 14.0-23.0 μmole range.

3.2.6.2 Measured Using 405 nm Laser and Fiber Optic CCD Spectrometer

PL spectra were also collected using a 405 nm laser (Thorlabs, CPS405, 4.5 mW) and an Ocean Optics QE pro high-performance spectrometer with 1000 ms integration time and 25 micron slit width. Photoluminescence was measured at a 90° angle relative to the excitation laser path.

3.2.7 Photoluminescence Quantum Yields (Φ_{PL})

Φ_{PL} of as-synthesized CsPbBr₃ NC and surface ligand treated CsPbBr₃ NCs were collected using the same conditions described in **section 2.2.7**.

3.2.8 Photoluminescence Lifetimes

Photoluminescence lifetimes were measured using a custom-built microscopy setup with an Olympus IX83 inverted microscope. The excitation wavelength was 488 nm, generated from an NKT Supercontinuum laser at a repetition rate of 19.4 MHz. Excitation light directed through a 488/10x (Chroma) filter was focused into the solution using a 60x, 1.2 NA water immersion objective. The excitation power was 0.33 μW at the back aperture of the objective. Fluorescence was directed through a 100 μm pinhole, followed by a 500LP (Chroma) filter and toward an avalanche photodiode (APD) detector. A Picoquant time correlated single photon counting (TCSPC) module (PicoHarp 300) was employed to log photon arrival times with respect to the sync pulse. Symphotime 64 software was used to generate histograms of arrival times and to fit the data. Fluorescence lifetimes were

extracted by exponential fitting of lifetime histograms using a calculated instrument response function (IRF) as reference.

3.2.9 **Transmission Electron Microscopy (TEM)**

TEM samples were prepared on a lacey carbon film supported by 300 mesh copper and TEM images were obtained using a JEOL 2010F and FEI Talos F200X operated at 200 kV. Energy dispersive X-ray spectroscopy measurements were recorded in STEM mode with 4 super energy dispersive spectroscopy (EDS) detectors on the FEI Talos F200X operated at 200 kV.

3.2.10 **X-Ray Diffraction**

Glass substrates were cleaned with successive sonication in a detergent solution, deionized (DI) water, acetone, and isopropanol baths for 10 minutes. The cleaned substrates were treated with UV-ozone for 10 minutes for enhanced wettability. Samples for XRD measurements were prepared by drop-casting the samples on cleaned glass substrates and drying under vacuum. The X-ray diffraction patterns (θ - 2θ scans) were taken on a Bruker-AXS D8 DISCOVER diffractometer with Cu K- α radiation ($\lambda = 1.5418$ Å) operating at 40 kV and 40 mA.

3.2.11 **Fourier-Transform Infrared (FTIR) Absorbance**

12.0 μ moles of each ligand or 3 μ L (~1.4 nmoles) of as-synthesized NCs or undiluted DDT-NCs was directly put onto a diamond attenuated total reflectance (ATR) plate. Then the sample was left on the diamond ATR for ~1 minute to evaporate the solvent.

After drying the sample completely, FTIR data were obtained with a Thermo Scientific Nicolet IS50 FTIR Spectrometer equipped with a diamond ATR plate. A resolution of 4 cm^{-1} and 64 scans were used in each measurement.

3.2.12 X-Ray Photoelectron Spectroscopy (XPS)

For depositing both as-synthesized CsPbBr₃ NC and surface ligand treated CsPbBr₃ NC films on ITO substrates, ITO substrates were cleaned using the same procedure described above. Then samples were drop-cast on the clean ITO substrates. After drop-casting, substrates were dried under vacuum. Then XPS spectra were collected with Thermo Scientific K- α XPS system and analyzer using a monochromated Al K- α source (1486.6 eV) for excitation and a pass energy of 200 eV for survey and 50.0 eV for small region scans. For spin-coated CsPbBr₃ bulk thin film study, XPS spectra were obtained with PHI 5600 system and analyzer using a non-monochromated Mg K- α source (1253.6 eV) for excitation and a pass energy of 187.75 eV for survey and 58.7 eV for small region scans.

3.2.13 ¹H Nuclear Magnetic Resonance (NMR)

12.0 μmoles of each ligand or 1.4-4.8 nmoles of NC (hexane was completely evaporated) were added in 600 μL of chloroform-d to make NMR samples. Then NMR was performed on a Bruker 400 NEO (Billerica, MA) using CDCl₃ and standard proton parameters.

3.3 Results AND Discussion

We synthesized colloidal CsPbBr₃ NCs in a standard precursor stoichiometry following the procedure reported by Protesescu and coworkers with minor changes.¹² Depending on the batch of NCs, the Φ_{PL} ranged from 39 to 79%, with an average Φ_{PL} of $56 \pm 16\%$ for all batches. Through much of the paper we present data from the same batch of CsPbBr₃ with a Φ_{PL} of 54% and synthesized with a Cs:Pb ratio of 0.25. We treated these CsPbBr₃ NCs with several different molecular and ionic ligands, some of which are reported in the literature,^{13,16,17,80,184} to compare their effects on PL properties of as-synthesized NCs. The molecular ligands we investigated herein include dodecanethiol (DDT), TOPO, and tri-n-octylphosphine (TOP), and the ionic ligands include ammonium thiocyanate (NH₄SCN), tetradecyldimethyl(3-sulfopropyl)ammonium hydroxide inner salt (abbreviated SB for sulfobetaine), and sodium dodecyl sulfate (SDS). For time-dependent PL intensity and optical absorbance measurements, 7-10 μL of stock as-synthesized NC dispersion (i.e., the synthesized crude NCs after two purification cycles) was diluted in 4 mL of hexane resulting in NC dispersions with absorbance of *ca.* 0.1 at 405 nm (NC concentration of *ca.* 1.2 μM) and time-dependent PL intensity and optical absorbance were collected for minutes, hours, and days after adding between 14 and 23 μmoles of a ligand to the diluted as-synthesized NC dispersion.¹⁰ As shown in **Table 3.1**, these ligand and NC concentrations correspond to 2-4 ligands per potential Pb atom on the NC surface, assuming that the NC surface is based on CsPbBr₃ unit cells. For absolute Φ_{PL} and time-resolved PL lifetime measurements additional hexane was typically added to keep the absorbance below 0.09 at 405 nm.

Table 3.1 Moles of each added surface ligand and the ratio of moles of surface ligand to moles of NCs for the fluorescence measurements.

Ligand	Amount of ligand (μmol)	Amount of NCs (nmol)	Ratio of Ligand to NC	Ratio of Ligand to Potential Pb surface site*
DDT	20.0	3.3	6.1E+03	3.5
OT	17.3	3.3	5.2E+03	2.9
BT	20.0	3.3	6.1E+03	3.4
DOS	16.3	3.3	4.9E+03	2.7
SDS	17.3	3.3	5.2E+03	2.9
NH ₄ SCN		3.3		
N	22.7		6.9E+03	3.8
TOP	13.5	3.3	4.1E+03	2.3
TOPO	16.3	3.3	4.9E+03	2.7

*Calculations of total number of potential Pb surface sites are based on square NCs with edge lengths of 10.5 nm.

The time-dependent Φ_{PL} of as-synthesized NCs upon addition of different surface ligands is presented in **Figure 3.1**. This time-dependent PL data shows that TOPO, TOP, and SDS decrease the Φ_{PL} of as-synthesized NCs, whereas NH₄SCN, SB, and DDT enhance the Φ_{PL} of the NCs. Previously, both TOP and PBU₃ were shown to provide significant improvements in Φ_{PL} ,^{55,184} but in our experiments TOP did not result in higher Φ_{PL} . We noticed similar Φ_{PL} enhancement of as-synthesized CsPbBr₃ NCs with NH₄SCN and SB as previously reported by Koscher, et al. and Krieg, et al., respectively.^{16,17} However, CsPbBr₃ NCs treated with NH₄SCN and SB show decreases in Φ_{PL} after 1 and 5 days, respectively. We suspect that the reduced Φ_{PL} and stability observed for NH₄SCN is due to our use of non-anhydrous and non-degassed hexane as the solvent, whereas

Koscher, et al. used dried and degassed solvents. On the other hand, DDT shows the highest enhancement in Φ_{PL} while maintaining stability even after 10 days. The time-dependent PL measurements, shown in **Figure 3.1b**, show that the PL intensity of the DDT treated NCs 10 days after treatment is 76% higher than the as-synthesized NCs. Shorter alkanethiols were also investigated, as shown in **Figure 3.1c and d**. These shorter alkanethiols result in similarly high Φ_{PL} after 1 day, but they are not as stable as DDT treated NCs.

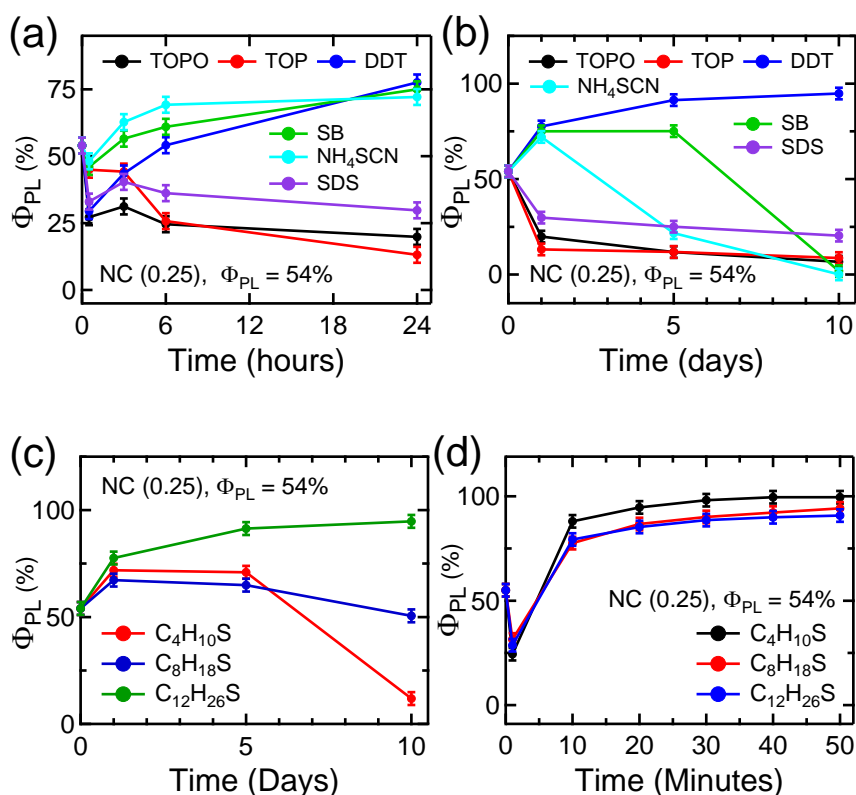


Figure 3.1 PL quantum yield of CsPbBr₃ NCs as a function of time in **(a)** hours and **(b)** days after addition of varying surface ligands and **(c)** days and **(d)** minutes after addition of alkyl thiols with varying alkyl chain lengths to the as-synthesized NC dispersions.

Ten days following addition of DDT to the CsPbBr₃ NCs, a pronounced blue shift in the optical absorption edge and PL maxima of the NCs is evident, as shown in **Figure 3.2a**. As-synthesized CsPbBr₃ NCs show a first excitonic absorption maxima at 508 nm and PL maximum at 514 nm with a Φ_{PL} of 54%. After 10 days, the first excitonic absorption maxima and PL maxima of DDT-NCs shift to 501 nm and 507 nm, respectively, with a Φ_{PL} of 98%. The blue shift in PL emission correlates with the change in Φ_{PL} . For example, as displayed in **Figure 3.2b**, at 0.5 hours, 6 hours, and 5 days following DDT addition the PL maxima are 514, 512, and 507 nm, while the Φ_{PL} are 29, 54, and 91%.

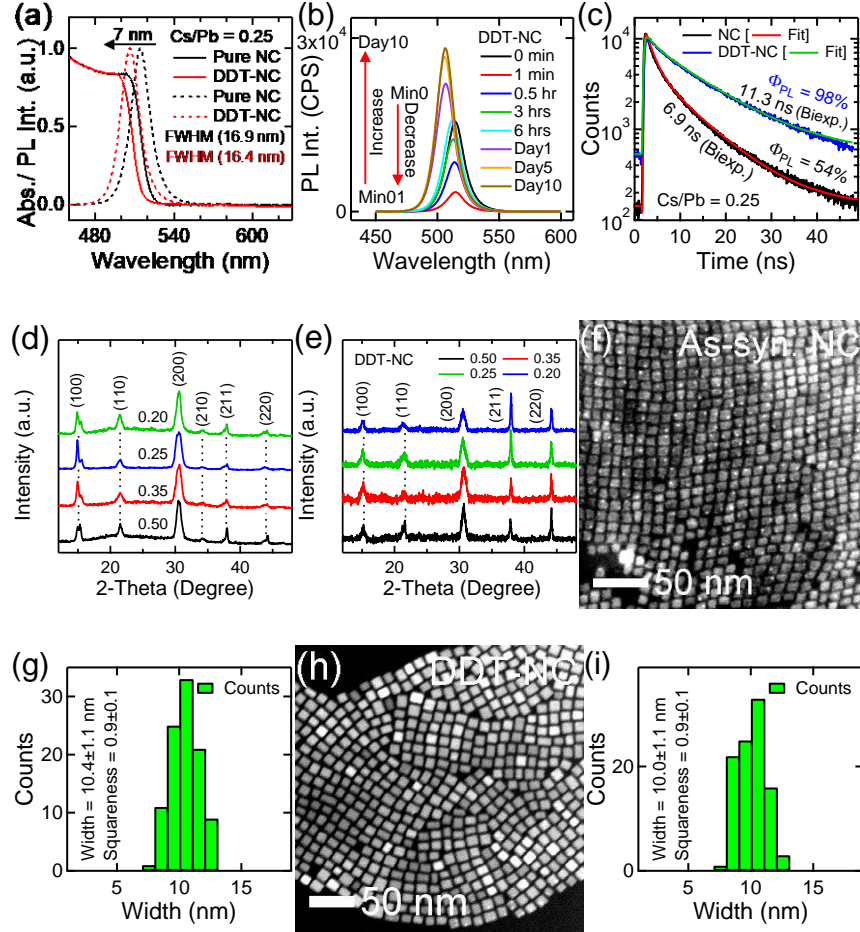


Figure 3.2 (a) Optical absorbance and PL emission spectra with no added DDT and 10 days after DDT addition, (b) time-dependent PL spectra of CsPbBr₃ NCs after addition of DDT, (c) comparison of time-resolved PL lifetime decays of as-synthesized and DDT treated NCs, (d and e) XRD patterns of as-synthesized NCs and DDT-NCs as a function of precursor stoichiometry, HAADF-STEM images and size distributions of (f and g) as-synthesized NCs (0.25), and (h and i) DDT-NCs (0.25) with calculated squareness. In (b) the time refers to the time after DDT was added to the NC dispersion, with the $t = 0$ spectrum recorded immediately before DDT addition.

The blue shift in emission likely results from a perturbation in the crystalline structure induced by the binding of thiol-derived species.^{18,173,187,188} This structural change is evident in the XRD data presented in **Figure 3.2d and e**, where DDT addition appears to reduce the fraction of NCs in the orthorhombic phase.^{173,188} Scanning transmission electron microscopy (STEM) analysis reveals minimal change in the NC size following

DDT treatment, as shown in **Figure 3.2f-j**. Here, the NCs have shorter edge lengths of 10.4 ± 1.1 and 10.0 ± 1.0 nm with squareness values of 0.9 for the as-synthesized and DDT treated NCs, respectively. Corresponding with the increased Φ_{PL} , time-resolved PL lifetime decays show an increase in the PL lifetime from 6.9 to 11.3 ns following DDT addition, as shown in **Figure 3.2c**. The as-synthesized NCs and DDT-NCs show bi-exponential decays; however, the PL decay of DDT-NCs is dominated by the long-lived component. Furthermore, there is a reproducible decrease in the FWHM of 0.2 to 2 meV (*ca.* 5% of FWHM) following DDT treatment. **Figure 3.2b** displays an interesting trend in the time-dependent measurements of PL intensity, whereby a significant drop in intensity is observed immediately upon DDT addition. Following this initial drop, the PL intensity begins to increase and continues increasing over multiple days. The initial drop in PL intensity lasts for approximately 1 minute if a 405 nm laser (4.5 mW) is used for excitation as compared to multiple hours if a standard fluorimeter is used for excitation at 405 nm, as shown in **Figure 3.1a and d**. As the excitation light intensity is *ca.* 750 times less intense than the 4.5 mW laser intensity, it is apparent that the reactions occurring to improve the Φ_{PL} can be photoinitiated.¹⁸⁹

To determine what reactions may be occurring to cause these changes in PL intensity following addition of DDT to the NC dispersion, we collected FTIR and ¹H NMR spectra of the different ligands, ligand mixtures, as-synthesized NCs, and purified DDT-NCs. Based on this series of data, we propose a mechanism whereby initial addition of DDT results in protonation of oleate ions with deprotonation of DDT and desorption of oleate ions and oleylammonium ions from the NC surface. The OA molecules do not coordinate to undercoordinated Pb atoms, as OA^- does,^{10,55} and thus the electron trap states

resulting from undercoordinated Pb are unpassivated and the Φ_{PL} temporarily drops. The thiolates generated upon deprotonation of DDT either bind the NC surface or catalyze thiol-ene reactions,¹⁹⁰ where thiol-ene reactions occur with remaining ODE, OA, and OLA. We suspect that the generated thiolates and/or thioethers are primarily what bind to the CsPbBr₃ NCs. The temporary drop in PL intensity following alkanethiol addition may arise from the protonation and desorption rate of OA⁻ exceeding the binding or generation rate of thiolates and thioethers. Another possibility is that a photo-induced reaction leads to this initial decrease, as will be expanded upon later.

Figures 3.3a show the FTIR spectra of sodium stearate (SS), OA, DDT, as-synthesized NCs, and purified DDT-NCs. The as-synthesized NCs show a weak band at around 1710 cm⁻¹, which is from the asymmetric stretching mode of C=O of COOH moieties in OA. Most OA molecules are in the oleate form, as the bands from the asymmetric and symmetric stretching modes of CO₂⁻ at 1556 and 1419 cm⁻¹, respectively, are more intense than the C=O stretching mode from the acidic form. After addition of DDT the C=O stretching mode from oleic acid increases considerably, whereas the bands at 1556 and 1419 cm⁻¹ from CO₂⁻ modes decrease. Additionally, the intensity of the O-H stretching mode of COOH groups at ~3475 cm⁻¹ increases after addition of DDT, as evident in **Figure 3.3c**. This data indicates that oleate ions are being protonated to form oleic acid following DDT addition, which is similar to the mechanism proposed to occur upon addition of an ammonium bromide salt.¹⁸⁶ Similarly, FTIR and ¹H NMR data indicate desorption of oleylammonium (NH₃⁺) ions and partial deprotonation to form the amine. In **Figure 3.3c**, we observe a broad band at 3296 cm⁻¹ in DDT-NCs, which is assigned to the

stretching mode of N-H bonds in NH_2 . This data is supported by the triplet peak of α -H of free OLA at ~ 2.7 ppm in ^1H NMR of purified DDT-NC shown in **Figure 3.3d**.

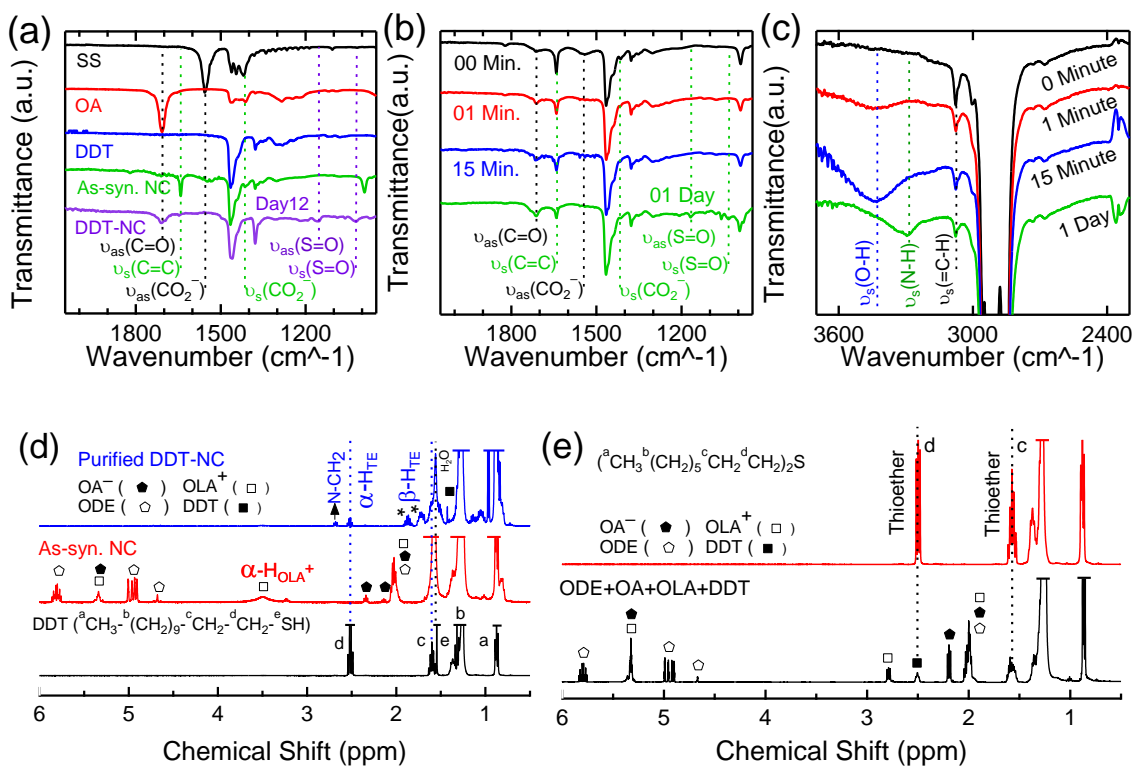


Figure 3.3 (a) FTIR spectra of sodium stearate (SS), oleic acid (OA), dodecanethiol (DDT), as-synthesized NCs, and purified DDT-NCs 12 days after DDT addition; (b & c) time-dependent FTIR spectra of as-synthesized CsPbBr₃ NCs before ($t = 0$ min) and after addition of DDT at different time intervals; ^1H NMR of (d) DDT, as-synthesized NCs, and purified DDT-NCs; and (e) a mixture of parent ligands and DDT without NCs added and dioctylsulfide (DOS).

The second major conclusion that can be reached upon analysis of the FTIR and ^1H NMR data presented in **Figures 3.3** is that the thiol-ene reaction is occurring, as illustrated in **Figure 3.4**.

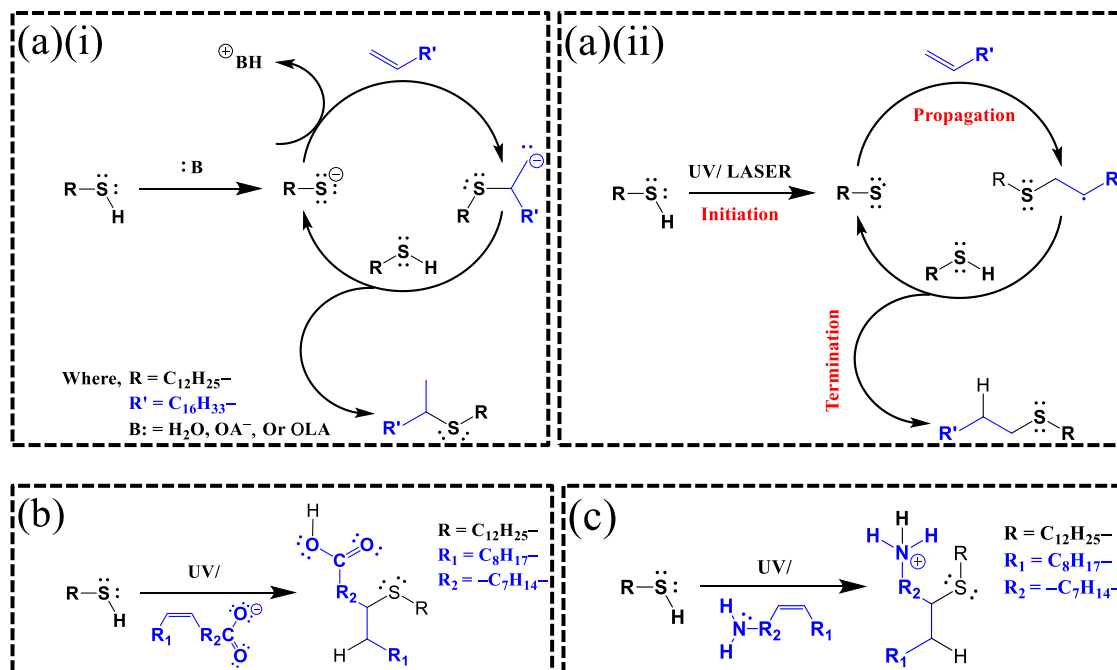


Figure 3.4 Base and photocatalyzed thiol-ene reactions showing reactions between DDT and (a) ODE molecules, (b) OA^- , and (c) OLA/ OLA^+ present in the as-synthesized NCs.

In this reaction, the thiol reacts with one carbon in a $C=C$ bond, followed by protonation of the other carbon. The thiol-ene reaction favors terminal alkenes (e.g., octadecene), but will also occur with internal alkenes, such as OLA and OA species.¹⁹⁰ This proposed mechanism is supported in that following DDT addition the number of $C=C$ bonds present in the ligand and residual parent solvent mixture decreases drastically. Here, the peak at 1641 cm^{-1} arising from the symmetric $C=C$ stretching mode changes from being one of the most pronounced peaks in the as-synthesized NC dispersion to being barely apparent in the NC dispersion following DDT addition. The disappearance of the $C=C$ double bonds is confirmed by 1H NMR data, where the $HC=CH_2$ proton signatures of ODE at 5.0 and 5.8 ppm as well as $HC=CH$ proton signatures at 5.4 ppm (OA and OLA) disappear following DDT addition. Time-dependent FTIR data were recorded to probe how the reaction products change with time and help in understanding the initial decrease in PL

intensity. These FTIR measurements were recorded on aliquots placed directly on an attenuated total reflectance cell, with the measurements started after the sample dried for *ca.* 1 minute. The FTIR data in **Figure 3.3b** show that only 1 minute after DDT addition, the vibrational modes associated with COOH have increased while those associated with COO⁻ have decreased. Additionally, an immediate decrease in the intensity of the C=C stretching mode is observed.

To gain insight into the mechanism by which DDT addition leads to an increase in the PL quantum yield, we present a series of transmission electron microscopy (TEM) data of CsPbBr₃ NCs before and after DDT treatment. Prior to DDT treatment, many batches of NCs display small (1-3 nm) dark spots on most NCs. These darker particles are apparent in multiple publications,^{45,191–193} with reports claiming the darker particles are either unreacted PbBr₂ particles, PbBr₂ attached to CsPbBr₃ particles, metallic Pb particles, or a mixture of Pb and PbBr₂ particles.^{45,191} Other reports have claimed these darker particles are metallic Pb particles formed by electron irradiation damage of CsPbBr₃ NCs occurring during the TEM measurement.^{192,193} We cannot completely rule out the possibility of forming these darker particles by electron beam irradiation, but there exists substantial literature support for the formation of metallic Pb from Pb-halide precursors and on Pb-halide perovskite surfaces without high-energy electron exposure.^{194–198} For example, metallic Pb particles have been shown to form in the presence of visible light excitation.^{198,199} Interestingly, upon DDT treatment these dark nanoparticles disappear. Thus, we suspect that elimination of these particles is associated with increased Φ_{PL} .

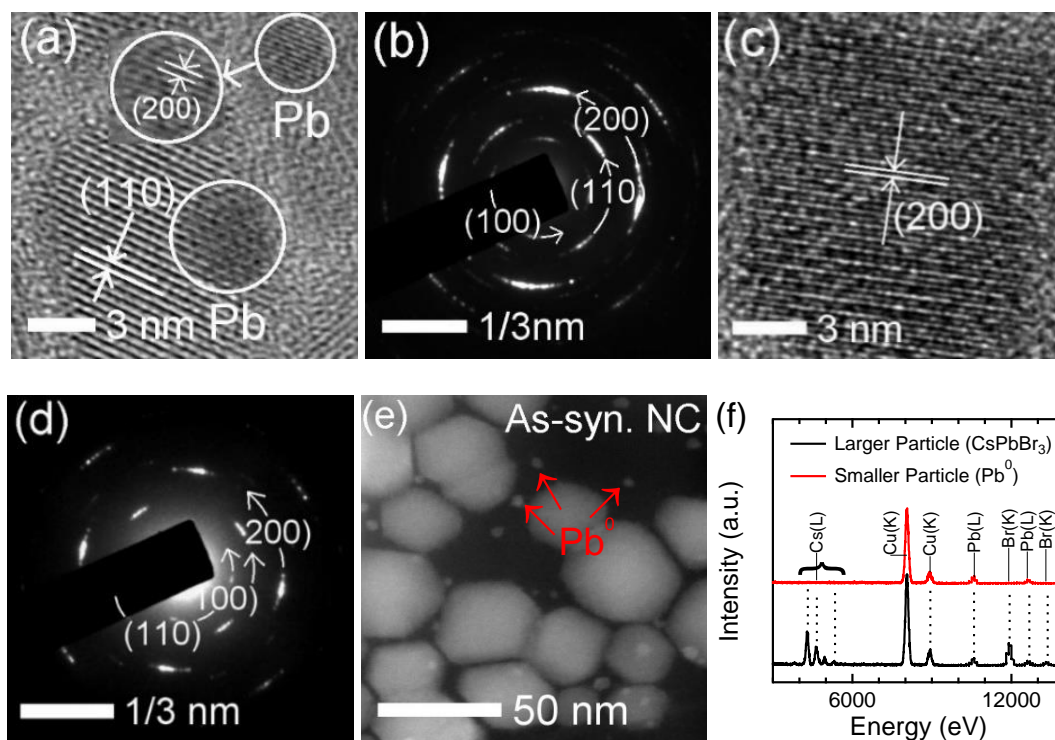


Figure 3.5 (a) Crystal fringes of as-synthesized NCs (0.25) with crystal fringes of black dots of metallic Pb particles, (b) SAED patterns of as-synthesized NCs (0.25), (c) crystal fringes of DDT-NCs, (d) SAED patterns of DDT-NCs (0.25), (e) HAADF-STEM images of as-synthesized CsPbBr₃ NCs with Cs:Pb ratio of 0.5, and (f) EDX spectra of as-synthesized NCs (0.5) that identify the small particles as metallic Pb.

To identify the composition of the darker particles, we collected high resolution images of the lattice fringes, selected area electron diffraction (SAED) patterns, and energy dispersive X-ray (EDX) spectra of the CsPbBr₃ NCs and darker particles, as shown in **Figure 3.5**. Based on the high resolution images of the lattice fringes and the SAED patterns, the lattice spacing values of ca. 2.5 Å correspond with the (002) reflections of metallic Pb particles (2.47 Å).²⁰⁰ Further analysis of CsPbBr₃ NCs synthesized from a 0.5 Cs:Pb ratio shows small darker particles that do not overlap with CsPbBr₃ NCs (**Figure 3.5e**) and can thus be probed directly by EDX without seeing the signal from the CsPbBr₃ NCs. The EDX spectra of the small dark particles show the presence of only Pb, as shown

in **Figure 3.5f**, thereby supporting that these dark spots are metallic Pb, which agrees with previous reports.^{201,202} We cannot say definitively if these Pb particles are present prior to the TEM measurements, as XRD patterns of CsPbBr₃ NCs synthesized from all Cs:Pb ratios do not show diffraction peaks from metallic Pb. However, these metallic Pb particles are on the scale of 1-3 nm, making up between 0.1 and 0.5% of the sample by volume relative to CsPbBr₃, and the intensities of their X-ray scattering peaks are likely below our detection limits. Furthermore, the most intense diffraction peak from Pb (31.3 degrees) overlaps with one of the most intense diffraction peaks from the CsPbBr₃ NCs (30.7 degrees). If present on the as-synthesized NCs, these metallic Pb particles will lead to additional pathways for non-radiative decay, and thus their elimination upon DDT addition may be a major factor leading to the enhanced Φ_{PL} .

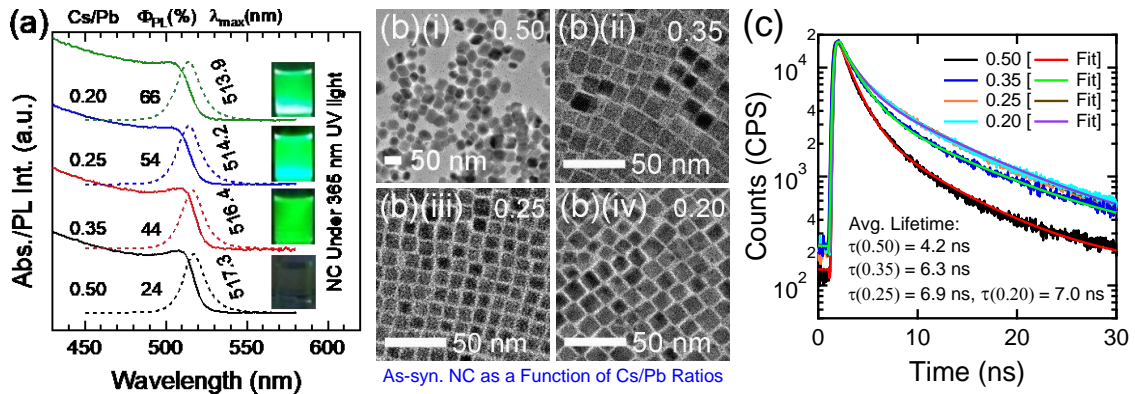


Figure 3.6 (a) Optical absorption & PL emission spectra of initially synthesized CsPbBr₃ NCs (insets show respective optical colors of the colloidal NC dispersion, prepared by dispersing 10 μ L of as-synthesized NCs into 2 mL hexane, under a 365 nm UV lamp), (b) TEM images, and (c) time-resolved PL lifetime decays of as-synthesized NCs as a function of precursor stoichiometry.

Several batches of NCs at each of four different precursor ratios, Cs:Pb of 0.2-0.5, were synthesized, as mentioned earlier, to determine if the formation of metallic Pb

particles depends strongly on the ratio of precursors. **Figure 3.6** shows optical absorption & PL emission spectra, TEM images, XRD patterns, and time-resolved PL lifetime decays of as-synthesized NCs as a function of precursor stoichiometry. The TEM images in **Figure 3.6 and 3.7a** show that the darker particles are not always present. We observed that at more Pb rich conditions (Cs:Pb ratios of 0.2 and 0.25) we were less likely to see the darker particles, or see fewer of the particles, as compared to the 0.35 and 0.5 ratios. However, we did synthesize several batches of NCs with Cs:Pb ratios of 0.2 and 0.25 that showed darker particles on nearly every NC (e.g., **Figure 3.7a**). The Φ_{PL} of the CsPbBr₃ NCs decreases as the Cs:Pb ratio increases, which correlates with the increasing occurrence of metallic Pb particles with increasing Cs:Pb ratios.

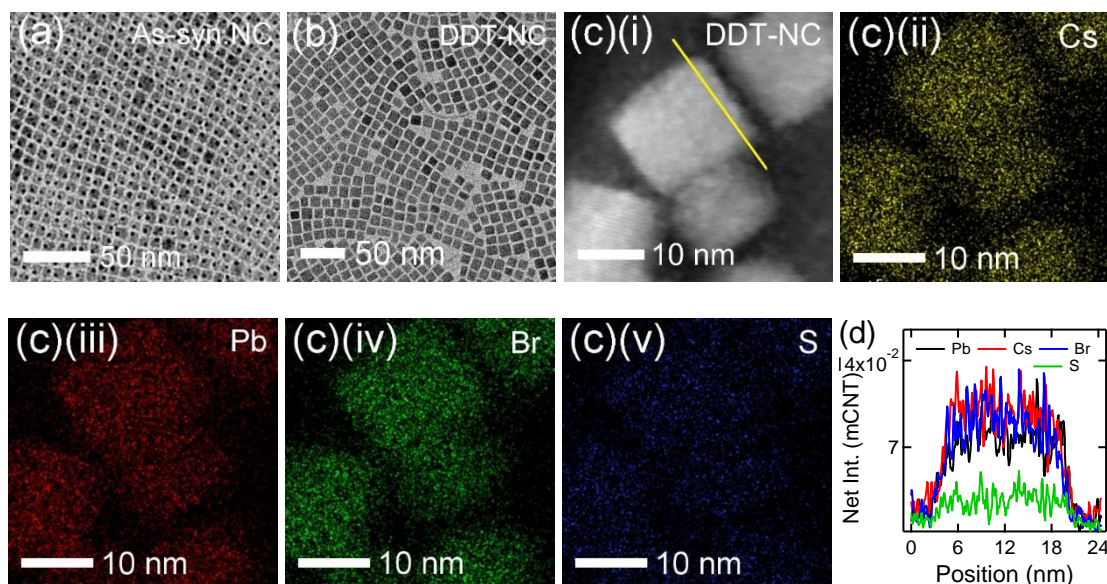


Figure 3.7 TEM images showing (a) as-synthesized NCs; (b) DDT-NCs (Cs:Pb ratio of 0.25); c(i) HAADF-STEM image and c(ii-v) STEM-EDS elemental mapping images of Cs, Pb, Br, and S of purified DDT-NCs (0.25); (d) STEM-EDS elemental line scan of purified DDT-NC (scan step size was 0.061 nm along the yellow line shown in HAADF-STEM image).

DDT treatment was applied to CsPbBr₃ NCs synthesized at all four precursor stoichiometries and we find that DDT increases the Φ_{PL} of all samples to between 80 and 99%, as shown in **Figure 3.8a**. **Figure 3.8b** shows that DDT treatment is also highly reproducible, as multiple NC batches synthesized with the same 0.25 Cs:Pb ratio all reached near unity Φ_{PL} . The time-resolved PL lifetime decays of the NCs as a function of Cs/Pb ratio, as shown in **Figure 3.8c-e**, show that the PL lifetimes increase from between 4.2 and 7.2 ns for the as-synthesized NCs to between 9.6 and 11.6 ns for the DDT-NCs. The increase in Φ_{PL} for all compositions is impressive, as even CsPbBr₃ NCs with low Φ_{PL} of 24% can be treated with DDT to increase the Φ_{PL} by over 3-fold to 80%. For the CsPbBr₃ NCs synthesized with Cs:Pb precursor ratios of 0.20, 0.25, and 0.35, the Φ_{PL} reaches 90-99%, and the high Φ_{PL} can remain for over 25 days as shown in **Figure 3.8f** when stored in capped vials in ambient atmosphere with non-anhydrous and non-degassed hexanes as the solvent. As a comparison, the Φ_{PL} of non-DDT treated CsPbBr₃ NCs decays to less than 1% over 10 days storage in identical conditions, as shown in **Figure 3.8g**. Thus, DDT treatment provides a robust approach to increasing the Φ_{PL} and stability of CsPbBr₃ NCs.

An important question is the importance of thioethers in the surface passivation process. To determine if thioethers alone could carry out a similar function as DDT, we treated as-synthesized NCs with dioctylsulfide (DOS). As shown in **Figure 3.8h**, DOS treatment results in an increase in the PL intensity of the CsPbBr₃ NCs by *ca.* 20%, corresponding to an increase in the Φ_{PL} from 62% to 74%.

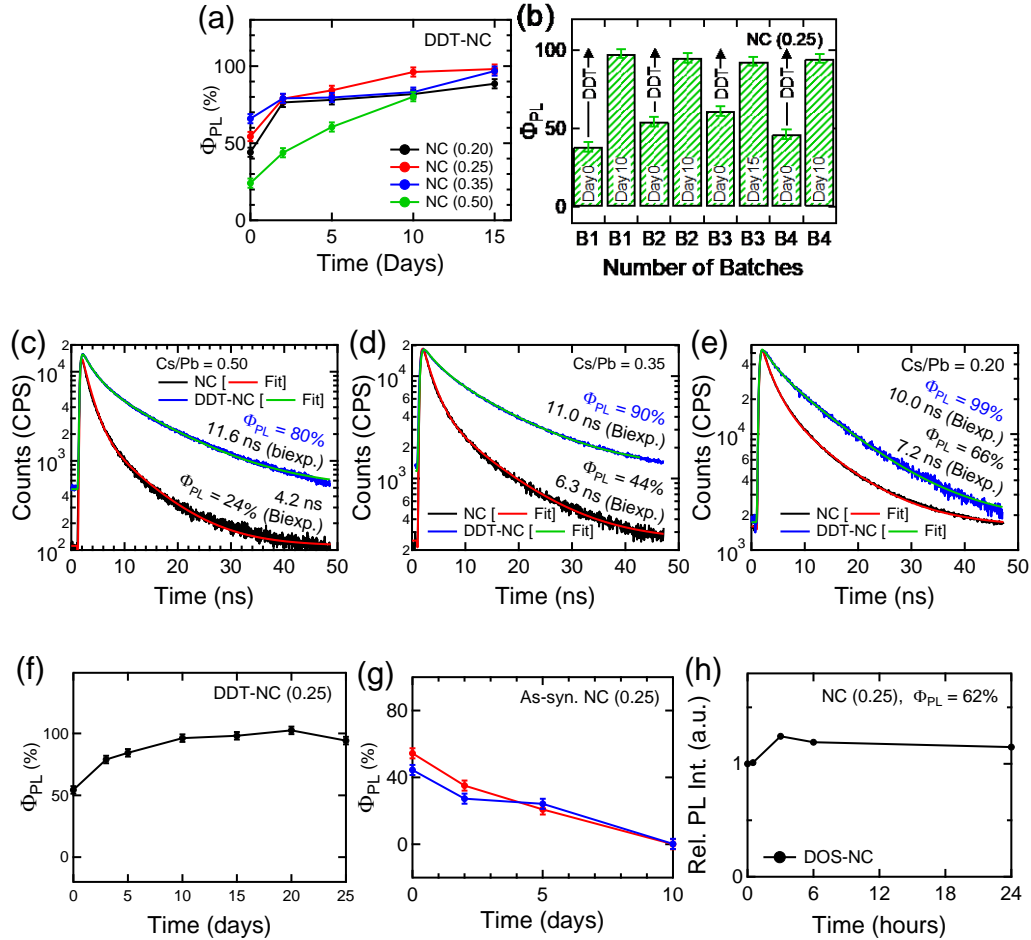


Figure 3.8 (a) Time-dependent Φ_{PL} showing the increase in Φ_{PL} of as-synthesized NCs as a function of precursor stoichiometry after addition of DDT, (b) Φ_{PL} of as-synthesized NCs followed by Φ_{PL} of DDT-NCs (0.25) from different batches synthesized with the same conditions, (c, d, and e) time-resolved PL lifetime decays of as-synthesized NCs and DDT-NCs as a function of Cs/Pb ratios of 0.50, 0.35, and 0.20., (f) time-dependent Φ_{PL} showing the increase in Φ_{PL} of as-synthesized NCs as a standard precursor stoichiometry after addition of DDT over 25 days, (g) time-dependent Φ_{PL} of as-synthesized NCs from two different batches showing decrease in Φ_{PL} over time, and (h) time-dependent PL intensity of DOS-NCs (DOS = dioctyl sulfide). In **Figure 3.8a and f-h** the day refers to the time after the thiol was added to the NC dispersion to enhance the Φ_{PL} of near unity, with the $t = 0$ (hour/day) spectrum recorded immediately before thiol addition.

Furthermore, the PL intensity increases more rapidly than when DDT is applied and an initial decrease in the PL intensity is not observed. Thus, DOS treatment supports that the thioether plays a role in improving the Φ_{PL} of these particles, but thioether addition alone cannot reproduce the high Φ_{PL} produced upon DDT addition. We propose that the

NC surfaces are decorated with both thioethers and thiolates, with the less bulky thiolates able to passivate surface sites that may be inaccessible to the bulkier thioethers. Furthermore, thiol addition may also be more effective than thioether addition alone due to the ability of thiols to protonate and inhibit binding of the dynamic OA^- ligands.

X-ray photoelectron spectroscopy and STEM-EDS confirm that sulfur is present on the DDT treated NCs. STEM-EDS mapping and line scans in **Figure 3.7c and d** clearly show the presence of thiol derived products on the washed DDT-NC surface. XPS measurements of DDT-NCs ($\text{Cs:Pb} = 0.25$) and CsPbBr_3 thin films with varying Cs:Pb ratios are shown in **Figure 3.9**, with both NCs and thin films showing the presence of sulfur. To reduce the concentration of unbound thiols on the thin film surface, the films were washed with toluene three times following DDT or DOS treatment. Even after rinsing, both DDT and DOS treatment of the thin films results in the presence of multiple sulfur species on the surface. Furthermore, sulfur is only observed on the surface when an excess of Pb is used for fabricating the thin films, as films processed with a 1:1 ratio of Cs to Pb do not show any sulfur. Interestingly, two to three distinct sulfur species appear on the surface, which are tentatively assigned to bound thiolates, bound thioethers, and bound oxidized sulfur species (sulfoxides and sulfones). The presence of oxidized sulfur species are also supported by the FTIR data, where the absorbance features at $1022\text{-}1050\text{ cm}^{-1}$ and 1150 cm^{-1} are suspected to be due to stretching of $\text{S}=\text{O}$ bonds in sulfoxides and sulfones.²⁰³

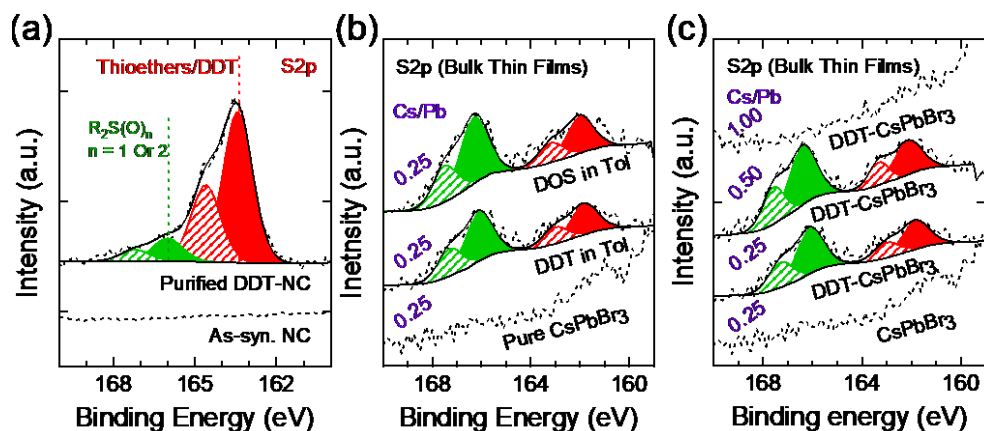


Figure 3.9 XPS spectra of comparison of S2p region of (a) as-synthesized NCs & purified DDT-NCs; (b) as-spin coated CsPbBr₃ & DDT/DOS-CsPbBr₃ bulk thin films; and (c) effects of DDT treatments for different Cs:Pb stoichiometries: as-spin coated CsPbBr₃ & DDT-CsPbBr₃ bulk thin films prepared as a function of different Cs:Pb ratios. Solid area and broken area indicate 2p_{3/2} and 2p_{1/2} regions, respectively.

The thiol-ene reaction is also known to be activated by exposure to UV light. Based on the assumption that thioethers likely play a role in enhancing the Φ_{PL} of CsPbBr₃ NCs, UV light exposure following DDT addition to a CsPbBr₃ dispersion should result in a more rapid increase in the Φ_{PL} . Indeed, we notice a rapid enhancement of PL properties of as-synthesized NCs under UV light and 405 nm laser light after addition of DDT to the NC dispersion. **Figure 3.10a** shows that the PL intensity increases more than 96% in one hour under continuous laser illumination, whereas under ambient conditions, it takes more 24 hours to increase its PL intensity by 44%. Under 365 nm UV light, as-synthesized NCs with Φ_{PL} of 46 and 79% show Φ_{PL} of 98% (in 90 minutes) and 94% (in 30 minutes), respectively, as shown in **Figure 3.10b**. **Figure 3.10c** show that the increased Φ_{PL} corresponds with an increase in the PL lifetime from 6.9 ns for the as-synthesized NCs to 9.6 ns for the DDT-NCs.

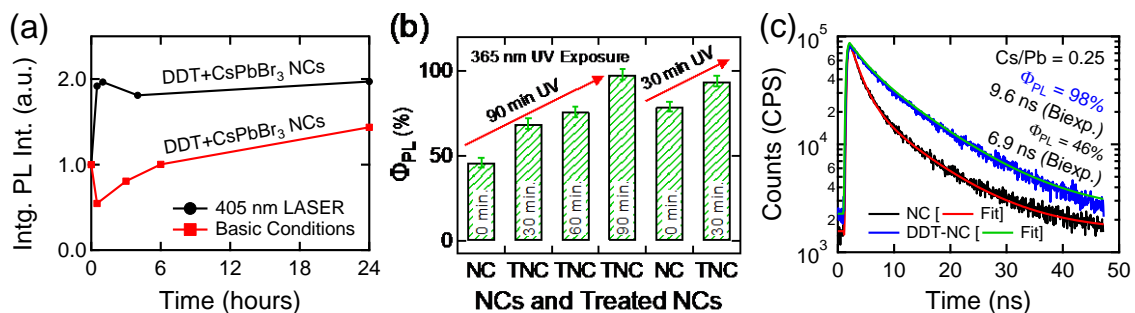


Figure 3.10 (a) Time-dependent integrated PL intensity of as-synthesized NCs upon addition of DDT under basic conditions (in presence of bases) and after 30 minutes of continuous 405 nm laser irradiation, (b) time-dependent Φ_{PL} of as-synthesized NCs (0.25) from two batches after addition of DDT under a 365 nm UV light, and (c) comparison of time-resolved PL lifetime decays of as-synthesized NCs before and after UV light exposure. In **Figure 3.10b**, the time refers to the time after the thiol was added to the NC dispersion to enhance the Φ_{PL} of near unity, with the $t = 0$ (minute) spectrum recorded immediately before thiol addition.

Further comparison highlighting the influence of 405 nm laser light exposure (4.5 mW) is evident in the large increase in PL intensity that occurs after only 5-10 minutes of 405 nm laser light exposure. A similar increase takes 5-10 days without UV light or blue laser exposure. We performed a series of experiments to determine if the presence of the CsPbBr₃ NCs were playing a role in catalyzing the formation of thioethers upon exposure to 405 nm laser light.

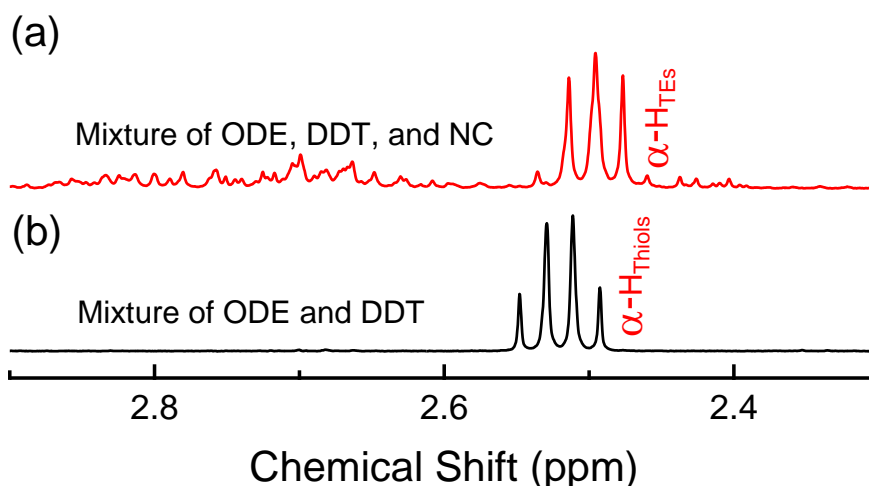


Figure 3.11 NMR data showing the $-\text{CH}_2\text{-S}$ region for (a) a solution of DDT and ODE after 30 minutes of 405 nm laser light exposure and (b) a solution of DDT and ODE with CsPbBr_3 NCs after 30 minutes of 405 nm laser light exposure. The quartet in the sample without CsPbBr_3 NCs indicates that DDT is still in the thiol form, whereas with the NCs the triplet indicates that DDT has reacted to form thioethers or disulfides. This measurement was directly done after 30 minutes of 405 nm laser light exposure without further purification of DDT-NCs.

As shown in **Figure 3.11**, without CsPbBr_3 NCs there is no evidence of appreciable thioether formation when DDT and ODE are combined in a hexane solution. However, when CsPbBr_3 NCs are added, nearly all the DDT is converted to thioethers or disulfides. Photo-induced reactions involving CsPbBr_3 NCs are only beginning to be investigated,¹⁸⁹ and these photo-initiated reactions appear to play an important role in improving the Φ_{PL} of CsPbBr_3 NCs.

3.4 Conclusion

Out of a series of surface ligand treatments for improving the optical properties of CsPbBr_3 NCs, DDT produces NCs with the highest Φ_{PL} and greatest long-term stability. Previously reported surface ligands, such as ammonium thiocyanate and a sulfobetaine result in improved Φ_{PL} , but the NCs are less stable than with DDT treatment. Mechanistically, DDT

treatment leads to protonation of OA^- ions, thiolate and thioether formation, and removal (or inhibited formation) of metallic Pb particles that are commonly observed to be present on the CsPbBr_3 NCs. Coordination of thiolates and thioethers to both metallic Pb and undercoordinated Pb at the CsPbBr_3 NC surfaces leads to passivation of trap states and a reduction in non-radiative decay pathways, which enables near unity PL quantum yields to be reached. Blue or UV light exposure can be applied to more rapidly increase the Φ_{PL} of the as-synthesized NCs. Moving forward it will be important to uncover how effective thiols, thiolates, or thioethers are at passivating trap states and improving the Φ_{PL} of other metal or organic metal halide perovskites of varying compositions. From a mechanistic standpoint, photo-initiated reactions with metal halide NCs and how they influence optical properties and surface chemistry is an area that we are continuing to pursue.

CHAPTER 4. GROWTH OF HIGHLY STABLE AND LUMINESCENT METAL-HALIDE PEROVSKITE NANOPlates VIA LIGAND MEDIATED ANION EXCHANGE OF CsPbCl₃ NANOCUBES WITH ALX₃

Adapted from “Uddin, M. A.; Glover, J. D.; Park, S. M.; Pham, J. T.; Graham, K. R. Growth of Highly Stable and Luminescent CsPbX₃ (X = Cl, Br, and I) Nanoplates via Ligand Mediated Anion Exchange of CsPbCl₃ Nanocubes with AlX₃. *Chem. Mater.* **2020**, 32 (12), 5217–5225. <https://doi.org/10.1021/acs.chemmater.0c01325>” with permission.

4.1 Introduction

Metal-halide perovskite NCs based on CsPbX₃ (X = Cl, Br, or I) are promising materials for optoelectronic applications, including photovoltaics,²⁰⁴ lasers,¹³⁸ and light emitting diodes (LEDs).¹³⁷ This genre of perovskite NCs is a subject of much attention because of their attractive and tunable optical properties, such as direct bandgaps,⁸ narrow emission line widths,¹² and high Φ_{PL} .^{13,16,17,173} After Protesescu, et al. reported the initial synthesis of CsPbX₃ NCs (X = Cl, Br, or I),¹² follow up studies based on post-synthetic compositional tuning of colloidal CsPbX₃ NCs through anion exchange reactions have been successfully demonstrated with both inorganic and organic halide salts as anion sources.^{64,67,142,145–147,159} These anion exchange reactions can be carried out in either the liquid or solid state with minimal changes to the NC size and shape.^{64,67,142,145–147,159} Inorganic halide salts include lithium halides (LiX),¹⁴² sodium halides (NaX),⁶⁴ potassium halides (KX),⁶⁴ zinc(II) halides (ZnX₂),⁶⁷ and lead(II) halides (PbX₂),^{145,159} while organic halide salts include oleyl/alkylammonium halides (O/RAmX),^{146,159} dihalomethane (H₂CX₂),¹⁴⁷ alkyltrichlorosilane,⁶³ trimethylsilyl halide,²⁰⁵ and benzoyl halide.¹⁸¹ However, though these synthetic routes yield highly luminescent CsPbBr₃ (emitting near 510 nm) and CsPbI₃ NCs (emitting near 680 nm) with Φ_{PL} of 70-98%^{67,146,159,181} and 14-55%,^{67,146,159,181} respectively, exchanged CsPbCl₃ NCs (emission near 410 nm) show

significantly lower Φ_{PL} of 1-12%.^{67,146,159,181} In general, the primary reason for the lower Φ_{PL} of CsPbCl₃ NCs are that deep trap states from Cl vacancies and resulting distortion of [PbCl₆]⁴⁺ octahedra are observed in CsPbCl₃ NCs,^{55,206} whereas only shallow trap states are observed in both CsPbBr₃ and CsPbI₃ NCs.^{55,206}

Apart from variations in stability and Φ_{PL} of anion exchanged NCs using different anion exchange precursors, PL properties of as-synthesized CsPbX₃ NCs are dependent on size and morphology. The unique applications of 1D and 2D perovskite NCs in photodetectors,²⁰⁷ LEDs,^{29,208–211} and lasers²¹² has spurred research interest in 1D and 2D perovskite NCs. Specifically, 2D perovskite nanoplates (NPs) have blue-shifted absorption and narrow emission line-widths, high absorption cross sections, and high radiative recombination rates.²¹³

CsPbX₃ NPs have been synthesized using hot injection methods,^{29,36,209,214,215} solid state crystallization methods,^{208,213} microwave-assisted methods,²¹⁶ as well as high temperature-and-pressure methods.^{31,217} The size and thickness of the perovskite NPs can be tuned via changing the synthesis temperature in hot injection methods and high temperature-and-pressure methods, although it is difficult to obtain a narrow size distribution of perovskite NPs with these methods.^{29,31,209,214,215,217} Synthesized perovskite NPs in most of the aforementioned methods also have low Φ_{PL} compared to their 3D counterparts.^{31,214} Reported Φ_{PL} of 2D perovskite NPs in hot injection methods or high temperature-and-pressure methods are 1-5% for violet and <30% for red emitters.^{31,217} Only green emitters show higher Φ_{PL} of 50-94%.^{211,215,218–222}

To address the low Φ_{PL} for blue-violet and red emitters and improve the stability of CsPbX₃ NCs and NPs, we report a new ligand mediated anion exchange route that involves

treating as-synthesized CsPbX₃ NCs with DDT and AlX₃. This treatment results in anisotropic NC formation with most NCs having a plate-shaped morphology (4-15 monolayers thick, where a monolayer indicates one layer of PbX₆ octahedra), high Φ_{PL} , and good long-term stability when CsPbCl₃ nanocubes are used as the starting material. The synthesized NPs show Φ_{PL} up to 50-65% for violet-blue emitting NPs ($\lambda_{\text{max}} = 410$ nm for violet emitters and 450-465 nm for blue emitters), near unity for green emitting NPs ($\lambda_{\text{max}} = 511$ nm), and 81% for red emitting NPs ($\lambda_{\text{max}} = 682$ nm). The reaction byproducts, including [Al(OH)_nX_{3-n}], thiolate ions, displaced halide ions, and excess X⁻ from hydrolysis are all shown to passivate the treated NP surface based on infrared absorbance spectra and scanning transmission electron microscopy–energy dispersive X-ray spectroscopy (STEM-EDS) imaging of the treated NPs.

4.2 Experimental Details

4.2.1 Materials

Cs₂CO₃ (99.9%, metals basis, Alfa Aesar), PbX₂ (99.9%, metals basis, Alfa Aesar), octadecene (ODE, tech. 90%, ACROS Organics), oleic acid (OA, tech. 90%, Alfa Aesar), oleylamine (OLA, >40%, TCI), tri-n-octylphosphine (TOP, ≥97%, Alfa Aesar), hexane (ACS grade, BDH), anhydrous toluene (Tol, 99.8%, Alfa Aesar), diethyl ether (DEE, 99.99%, SeccoSolv[®]), 1-dodecanethiol (DDT, >95%, TCI), anhydrous AlX₃ (99.99%, metal basis, Alfa Aesar), α -phase Al₂O₃ (99.9%, metal basis, Alfa Aesar), and Al(OH)₃ (Al₂O₃ content 50-57%, Aldrich) were purchased and used as received.

4.2.2 Synthesis of CsPbX₃ Nanocubes

0.1018 g Cs₂CO₃, 5.0 mL ODE, and 0.39 mL OA were added to a 50 mL round bottom flask with side-arm glass stopcock. The flask was then heated to 120 °C and kept at 120 °C for 1 hour under vacuum. For dissolving Cs₂CO₃ completely and forming Cs-oleate, the reaction mixture in the flask was heated to and maintained at 150 °C under a N₂ environment for 1 hour while stirring the reaction mixture at 400 rpm.

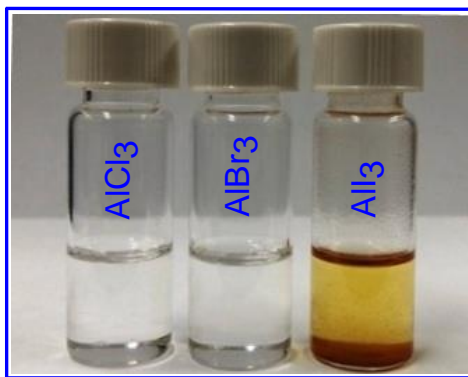
For synthesizing CsPbX₃, approximately 52.30 mg PbCl₂ (with 1 mL TOP), 69 mg PbBr₂, and 86.67 mg PbI₂ were used. An appropriate amount of lead(II) salt was added to 5 mL ODE in a different 50 mL round bottom flask with side-arm glass stopcock for synthesizing Cl-, Br-, and I-based NCs. Then the flask was heated to 120 °C and kept at 120 °C under vacuum while stirring the solution mixture at 400 rpm. After 15 minutes of the temperature reaching 120 °C, 1.5 mL, 0.5 mL, and 0.7 mL each of OA and OLA were injected in the flask successively for synthesizing Cl-, Br-, and I-based NCs, respectively. When the solution mixture in the flask turned a clear yellow color, the flask was heated to 170 °C (CsPbCl₃) or 180 °C (CsPbBr₃ and CsPbI₃ NCs). To form NCs, the stirring speed in the PbX₂ containing flask was reduced to 200 rpm and a preheated 0.4 mL Cs-oleate solution from the other flask was injected dropwise into the PbX₂ containing flask with a 2 mL glass syringe. Following the Cs-oleate injection, the flask was immediately cooled down to room temperature by submerging the flask in an ice bath.

For storage and further studies of colloidal CsPbX₃, 1.0 mL of crude solution in a 2 mL plastic vial was centrifuged at 10000 rpm for 5 minutes, and the colorful supernatant was discarded. Then NCs were dispersed in 300 µL hexane, and the solution was centrifuged at 10000 rpm for 5 minutes. Supernatant was collected and the pellet discarded. Total

volume of the stock NC dispersion was 2.7 mL of CsPbCl₃, 1.8 mL of CsPbBr₃, and 2.1 mL of CsPbI₃.

4.2.3 Preparation of C₁₂H₂₅SH-C₄H₁₀O-AIX₃ Solutions

These solutions are prepared by mixing diethyl ether, dodecanethiol, and aluminum trihalide in toluene at a molar ratio of 1-1-0.33-10 (and 3-3-0.33-10) at room temperature. Though two compositions were made, throughout the manuscript mostly a molar ratio of 1-1-0.33-10 was used (as noted in **Table 4.1** in section 4.1.4).



Though two compositions were made, throughout the manuscript mostly a molar ratio of 1:1:0.33:10 was used.

4.2.4 Synthesis of DDT-AIX₃ Treated NPs

The synthesized nanocubes were then treated with DDT-AIX₃ solutions through simple solution mixing. First, the stock CsPbCl₃ solution was diluted with hexane according to **Table 4.1**. Following dilution, the prepared DDT-AIX₃ solutions were added according to the values shown in **Table 4.1**. For most measurements, no additional purification was performed after DDT-AIX₃ addition. However, in the case of the DDT-AlBr₃ NC samples made for STEM-EDS analysis, exchanged CsPbBr₃ NCs were purified via 2x centrifugation of crude exchanged CsPbBr₃ NCs in hexane. In this process, 50 μ L

DDT-AlBr₃ (1-1-0.33-10) solution was added to 250 μL parent NC dispersion (100 μL parent NC stock solution was mixed with 150 μL hexane) to get exchanged CsPbBr₃ NCs. Two days following treatment the exchanged NCs were centrifuged at 10000 rpm for 30 minutes and the precipitate was collected. Collected NC precipitate was again dispersed in 300 μL hexane and the resulting NC dispersion was centrifuged one more time with the same spin conditions and the precipitate was again collected. The whole process was done primarily to remove unbound thiols, thiolates, and/or thioethers.

Table 4.1 amounts of as-syn. NCs, hexane (volume has a minimal influence), and AlX₃ solutions used in the treatment of CsPbCl₃ NCs to form CsPbX₃ NPs.

Treated NCs	Amount of CsPbCl ₃ NC Stock (μL)	Amount of Hexane (mL)	Absorbance of NC dispersion at 350 nm	Approx. Conc. of NCs (μM)	Amount of DDT-AlX ₃ solution (μL)
CsPbCl ₃	10	3.980	≤0.1	1.2-1.5	5 to10 (1-1-0.33-10)
CsPbCl _{3-x} Br _x	100	1.897/3.897	≤1.0	12.0-15.0	2.9 (1-1-0.33-10)
	50	3.948	≤0.5	6.0-7.5	2.2 (3-3-0.33-10)
CsPbBr ₃	10	3.980	≤0.1	1.2-1.5	5 to 10 (1-1-0.33-10)
	100	1.850/3.850	≤1.0	12.0-15.0	50 (1-1-0.33-10)
CsPbI ₃	50	3.944	≤0.5	6.0-7.5	6 to10 (1-1-0.33-10)
	50	3.941	≤0.5	6.0-7.5	9 (3-3-0.33-10)

Note: Mol ratio of AlX₃ to NC is approximately in the range of 1933:1 to 2416:1.

4.2.5 Characterization Methods

4.2.5.1 Absorbance

UV-Vis absorption spectra were obtained using a Thermo Scientific Evolution 201 UV-Visible Spectrophotometer with 50 ms integration time and 2 nm slit widths. For the fast UV-Vis absorption spectra that are presented for the first 18 seconds following DDT-AIX₃ addition, the spectra were collected using an Ocean Optics QE pro high-performance spectrometer with a 10 ms integration time and 25 micron slit width.

4.2.5.2 Fluorescence AND Φ_{PL} Measurements

Photoluminescence spectra were measured using a Lumina Fluorescence Spectrometer by Thermo Fisher Scientific with 20 ms integration time and 2.5 nm slit width with an excitation wavelength of 350 nm. Photoluminescence spectra were also collected using a 405 nm laser (Thorlabs, CPS405, 4.5 mW) and an Ocean Optics QE pro high-performance spectrometer with 300 ms integration time and 100 micron slit width. Photoluminescence was measured at a 90° angle relative to the excitation laser path. Time-dependent PL data for the first 18 seconds were collected following the addition of DDT-AIX₃ to the CsPbCl₃ NC dispersion using the Ocean Optics QE pro high-performance spectrometer. The amounts of as-synthesized NCs, hexane, and AIX₃ used to synthesize the NCs are listed in **Table 4.1**.

For Φ_{PL} measurements, the same samples were used as in the PL spectra measurements, but the samples were diluted in hexane to keep the absorbance between 0.05 and 0.1 at the excitation wavelength. PL spectra were collected using a Horiba Scientific FluoroMax Plus-C fluorimeter equipped with an integrating sphere by exciting the CsPbCl₃ NCs with

a 350 nm laser while the CsPbCl_{3-x}Br_x, CsPbBr₃, & CsPbI₃ NCs were excited with a 405 nm laser. The Φ_{PL} was calculated using the Horiba Scientific FluorEssence™ software, as described in our recent manuscript.¹⁴

4.2.5.3 Photoluminescence Lifetimes

Photoluminescence lifetimes were measured using a DeltaHub™ high throughput time correlated single photon counting (TCSPC) controller with an excitation wavelength of 393 nm generated by a pulsed NanoLED excitation source. Experimental PL lifetime results were fit with exponential decay curves using Horiba Scientific Decay Analysis Software.

4.2.5.4 Fourier Transform Infrared (FTIR) Absorbance

Each sample was directly dropped from solution onto a diamond attenuated total reflectance (ATR) plate. Then the sample was left on the diamond ATR for \approx 1 minute to evaporate the solvent. After drying, FTIR data were obtained with a Thermo Scientific Nicolet IS50 FTIR Spectrometer equipped with a diamond ATR plate. A resolution of 4 cm⁻¹ and 64 scans were used in each measurement.

4.2.5.5 Raman Spectroscopy

Samples were drop cast on a glass microscope slide and Raman spectra were obtained with a Thermo Scientific Raman Microscope DXR equipped with a 10x objective lens. Raman measurements were carried out with a laser power of 2.5 mW for each organic

molecule and 10 mW for NC dispersions using an excitation wavelength of 532 nm. A resolution of 4 cm^{-1} and 32 scans were used in each measurement.

4.2.5.6 **Transmission Electron Micrographs (TEM)**

TEM samples were prepared on lacey carbon films supported by 300 mesh copper and TEM images were obtained using a FEI Talos F200X operated at 200 kV. Energy dispersive X-ray spectroscopy measurements were recorded in STEM mode with 4 super energy dispersive spectroscopy (EDS) detectors on the FEI Talos F200X operated at 200 kV.

4.2.5.7 **Atomic Force Microscope (AFM) Images**

AFM samples were made by spin-coating 20 μL of 12-15 μM NC dispersions on cleaned glass ($1.25 \times 1.25\text{ cm}^2$) or freshly cleaved mica substrates at 1000 rpm for 30 seconds. Samples were then dried under vacuum overnight. AFM images were acquired employing a HQ:NSC15/AI BS cantilever (40 N/m stiffness) on a JPK Nanowizard 4a microscope.

4.2.5.8 **X-Ray Diffraction**

Samples for XRD measurements were prepared by drop casting the samples on glass substrates and drying under vacuum. The X-ray diffraction patterns (θ - 2θ scans) were taken on a SIEMENS D500 and DISCOVER diffractometer as well as Bruker-AXS D8 and ADVANCE diffractometer with Cu $K\alpha$ radiation ($\lambda = 1.5418\text{ \AA}$) operating at 40 kV and 40 mA. XRD data were collected on the same day of preparation or one day after preparation.

4.3 Results and Discussion

AlX_3 , with $X = \text{Cl}, \text{Br}, \text{or I}$, are extremely hygroscopic Lewis acids. One mole of AlX_3 vigorously reacts with three moles of water to liberate three moles of HX and 1 mole of $\text{Al}(\text{OH})_3$ with an enthalpy change (ΔH) of $\leq -303.1 \text{ kJ} \cdot \text{mol}^{-1}$.²²³ This liberated heat energy from the hydrolysis reaction helps easily overcome the activation energy of anion exchange reactions between 3 moles of HX and 1 mole of parent CsPbCl_3 nanocubes ($E_A = 24.1\text{-}28.0 \text{ kJ} \cdot \text{mol}^{-1}$).¹⁵⁹

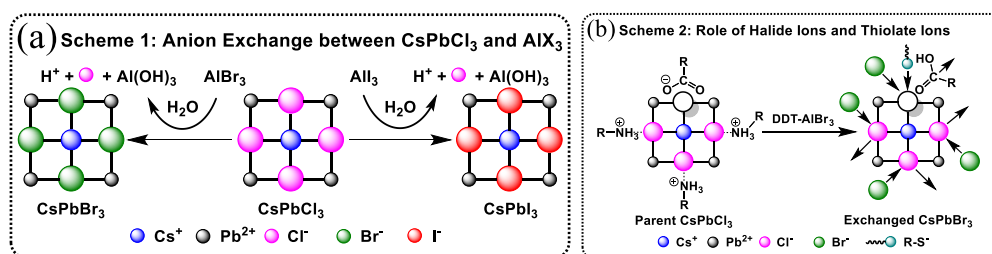


Figure 4.1 (a) Anion exchange between CsPbCl_3 and AlX_3 in the presence of dissolved water in hexane; (b) role of excess halide ions and thiolate ions in the ligand mediated anion exchange route with AlX_3 .

As a result, anion exchange reactions with AlX_3 are rapid and occur at room temperature, resulting in the formation of CsPbX_3 , where X is the halide that was originally bound to Al. **Figure 4.1a** highlights the anion exchange reaction induced by adding AlX_3 to CsPbCl_3 NCs. To observe the anion exchange between CsPbX_3 NCs and AlX_3 in solution, first, CsPbX_3 NCs were synthesized following a previously detailed procedure.¹² **Figure 4.2a** shows characteristic optical absorbance and PL emission spectra of as-synthesized CsPbX_3 NCs. The as-synthesized CsPbCl_3 NCs display a much lower Φ_{PL} of $<1\%$ and a shorter PL lifetime of 1.3 ns than the CsPbBr_3 and CsPbI_3 NCs (**Figure 4.2b**). This low Φ_{PL} and short lifetime of CsPbCl_3 NCs indicates that non-radiative decay

processes are dominant over radiative routes, which is most likely attributed to deep trap states resulting from Cl vacancies in CsPbCl₃ NCs.^{55,206} All as-synthesized CsPbX₃ NCs appear primarily cubic in shape with average edge lengths ranging from 8.7 to 10.0 nm as shown in **Figure 4.2c-e**. XRD patterns shown in **Figure 4.2f** confirm the cubic crystal structure of CsPbX₃ NCs.

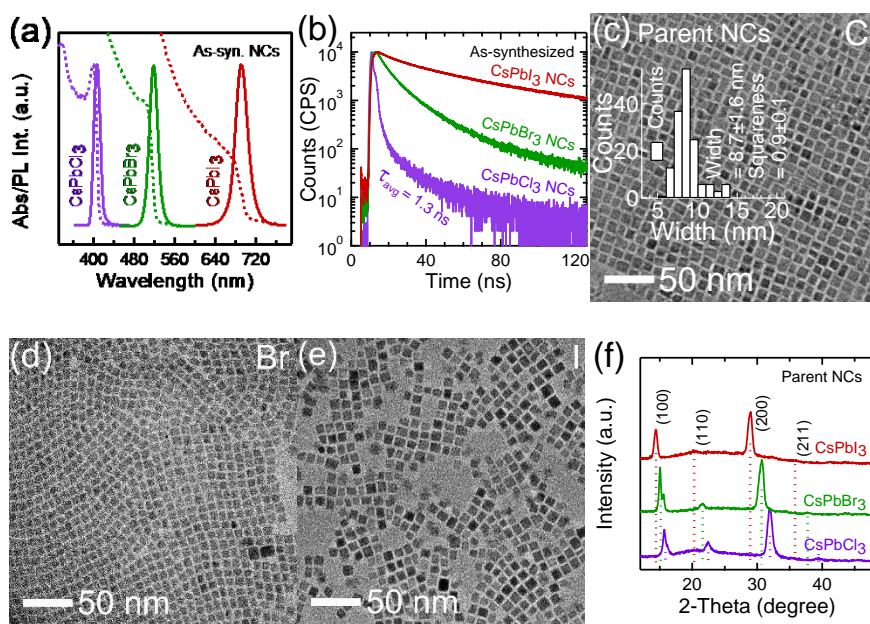


Figure 4.2 (a) UV-Vis absorbance & PL emission, (b) time-resolved PL lifetime decays, (c-e) TEM images, and (f) XRD patterns of as-synthesized CsPbX₃ NCs.

After verifying PL properties and crystallinity of CsPbX₃ NCs, we treated fresh as-synthesized CsPbCl₃ NCs with freshly prepared AlX₃ solutions. Treatment with AlX₃ only, i.e., no additional surface ligands, in diethyl ether leads to a rapid enhancement in PL intensity and anion exchange in the CsPbX₃ NCs. Treatment of the as-synthesized CsPbCl₃ NCs with AlCl₃ increases the PL intensity of CsPbCl₃ NCs by a factor of 21, as shown in **Figure 4.3a**, but these treated NCs suffer from poor stability. Here, the PL intensity reaches a maximum 30 minutes after treatment, followed by a 57% decrease by the one-day mark.

This decrease likely occurs because AlX_3 solutions in diethyl ether lead to an increase in solution acidity that results in protonation and desorption of oleate ligands and destabilization of the colloidal NCs.¹⁴

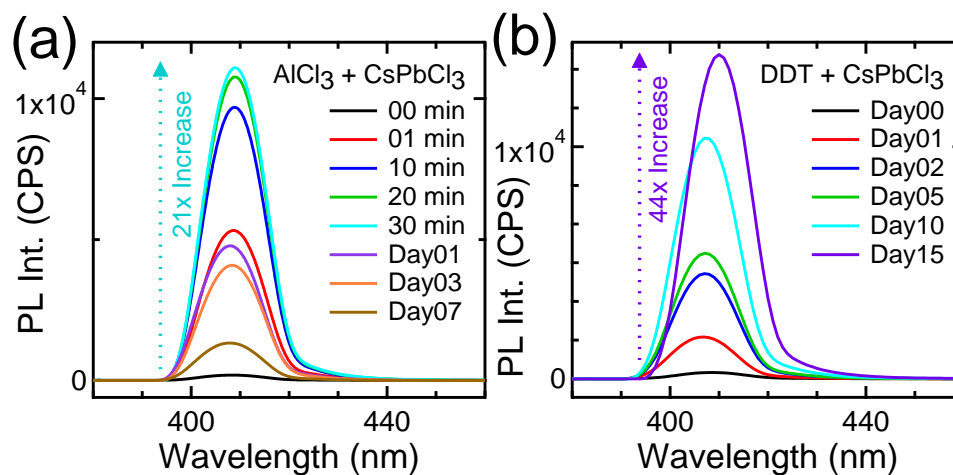


Figure 4.3 Time-dependent PL intensity of (a) AlCl_3 treated CsPbCl_3 (with no DDT added in the parent CsPbCl_3 dispersion) and (b) DDT treated CsPbCl_3 NCs (with no AlCl_3 added in the parent CsPbCl_3 dispersion).

We also explored treatment of CsPbBr_3 and CsPbI_3 parent NCs with AlX_3 only, but the PL of the treated NCs drastically decreases within a few minutes of treatment, as shown in **Figure 4.3a-f**. This decrease in PL does not arise from CsPbBr_3 or CsPbI_3 NC dissolution, as evident in the UV-Vis absorbance spectra in **Figure 4.4g & h**. Thereby, we suspect the decrease in PL intensity is due to the penetration and doping of small Al^{3+} ions in the parent CsPbBr_3 or CsPbI_3 NCs, which is supported by previous reports that doping of small trivalent cations decreases the Φ_{PL} of CsPbBr_3 NCs.^{224,225} Thus, the remainder of this work focuses on CsPbCl_3 as the parent NCs.

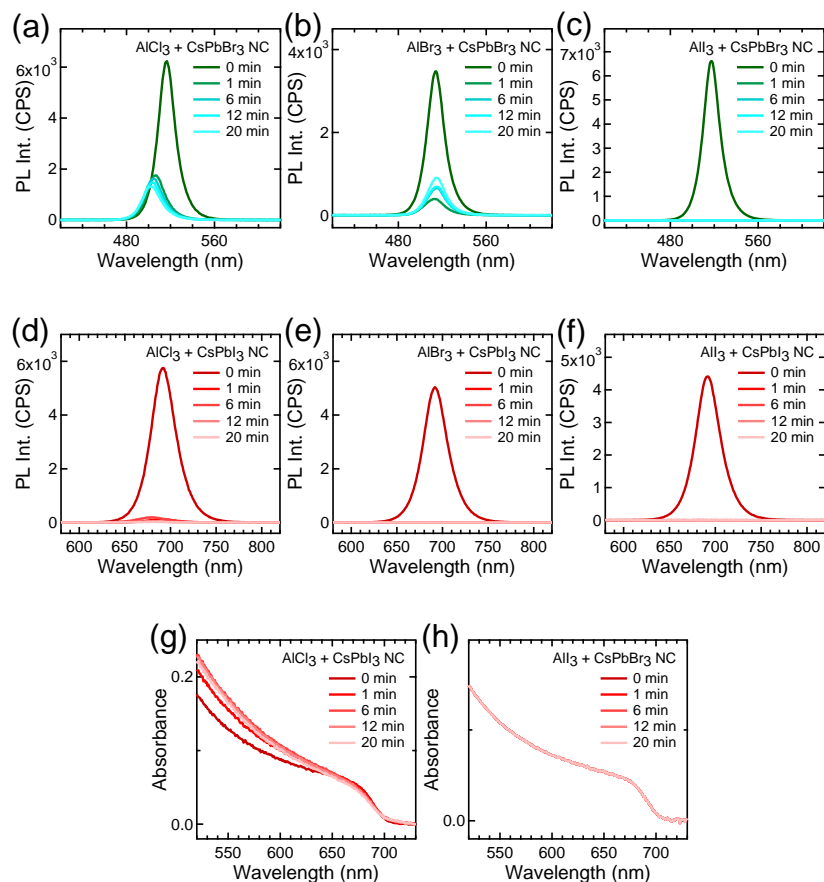


Figure 4.4 Time-dependent PL emission spectra of (a-c) AlX_3 treated CsPbBr_3 NCs & (d-f) AlX_3 treated CsPbI_3 NCs and time-dependent optical absorbance spectra of (g) AlCl_3 treated CsPbI_3 NCs & (h) AlI_3 treated CsPbBr_3 NCs (all spectra are nearly identical and fall on top of each other). In 4.3.4a-h, all the experiments were done with no additional DDT in the parent CsPbCl_3 dispersion.

Encouraged by our recent work demonstrating that DDT can stabilize CsPbBr_3 NCs,¹⁴ we applied DDT to as-synthesized CsPbCl_3 NCs (i.e., no AlCl_3 was added). This DDT treatment results in an enhancement in PL intensity (44x increase in PL intensity) and improved stability of CsPbCl_3 NCs, as shown in **Figure 4.3b**. Mechanistically, it is likely that dodecanethiolates and thioethers are created and bind to undercoordinated lead after desorption of parent oleate ions, as depicted in **Figure 4.1b**.¹⁴ When a combined DDT- AlCl_3 solution is added to as-synthesized CsPbCl_3 NCs, the PL intensity increase is

even greater, with a 74 times increase in the PL intensity over that of parent NCs after 10- days of treatment, as shown in **Figure 4.5**.

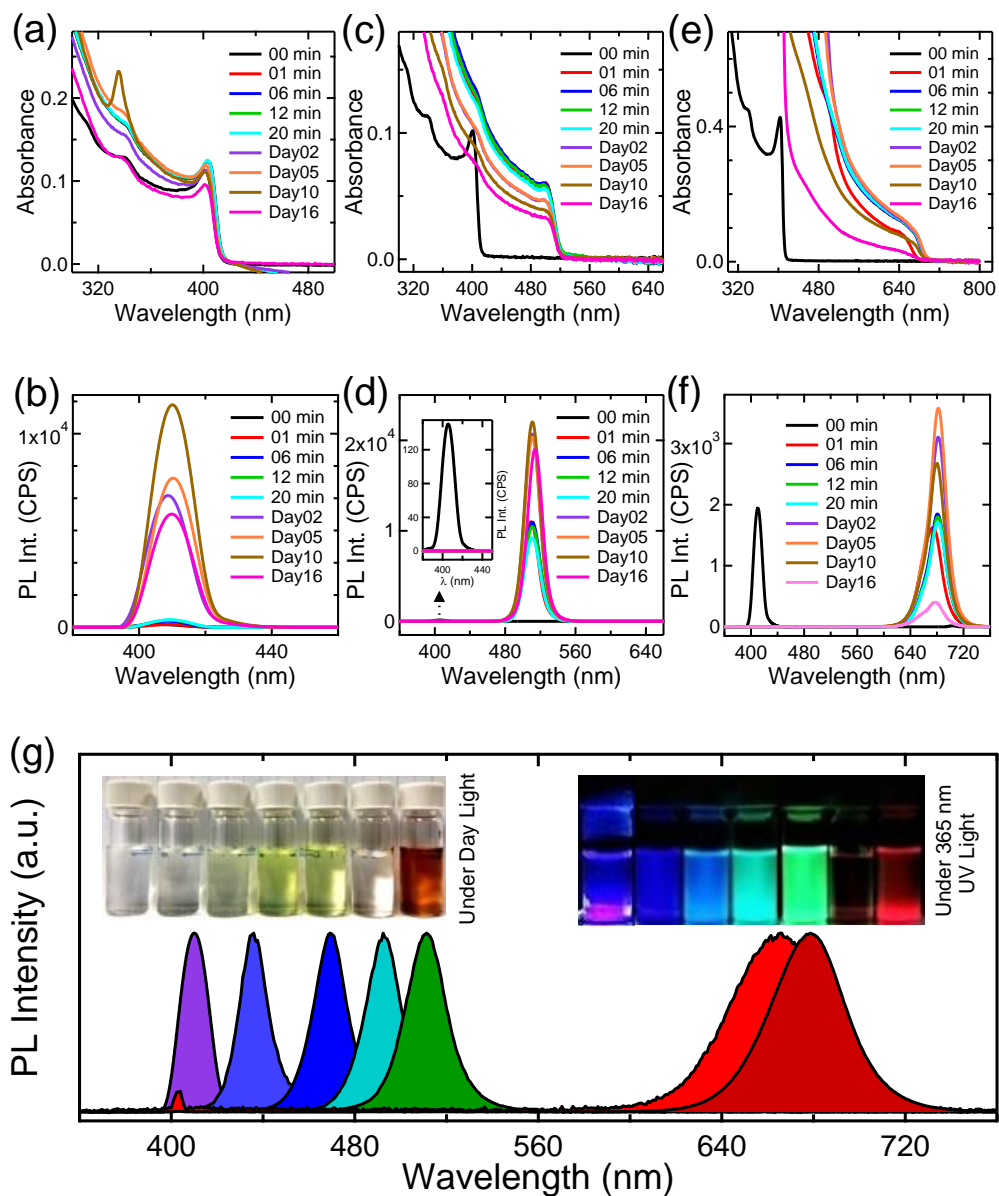


Figure 4.5 Time-dependent UV-Vis absorbance & PL intensity of DDT-AIX₃ treated NCs: (a, b) treated CsPbCl₃ NCs, (c, d) exchanged CsPbBr₃ NCs, (e, f) exchanged CsPbI₃ NCs, and (g) PL emission spectra of DDT-AIX₃ treated NCs covering the visible spectra ranging from 410 nm to 680 nm.

The absorbance and PL of parent CsPbX₃ NCs can be readily tuned throughout the visible region by varying both the halide in AlX₃ and the amount of DDT-AlX₃ solution added, as shown in **Figure 4.5g and 4.6a**. As expected, when DDT-AlBr₃ and DDT-AlI₃ solutions are added, both the center of the absorption edge and PL maxima rapidly shift to 502 & 511 nm and 677 & 682 nm, respectively. Anion exchange occurs within a few seconds of DDT-AlX₃ addition to parent CsPbCl₃ NCs at room temperature, as shown in **Figure 4.5g and 4.6a**, showing that the NC emission can be readily tuned by varying the amount of DDT-AlBr₃ added with respect to the amount of CsPbCl₃ NCs (see **Table 4.1**).

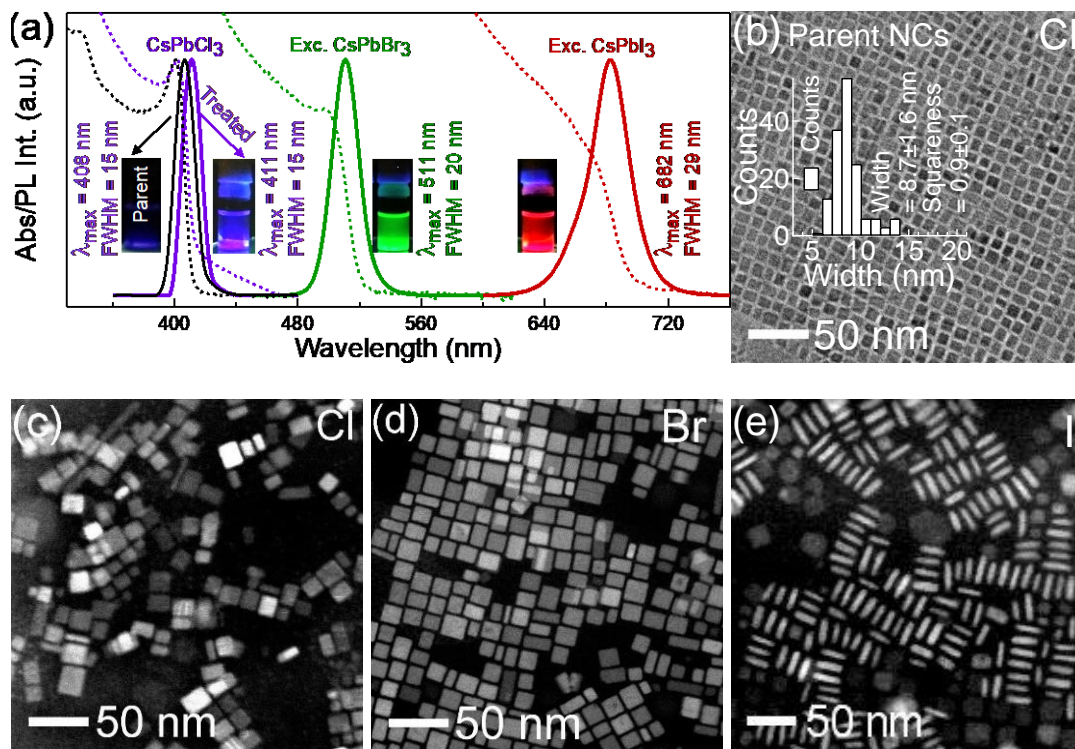


Figure 4.6 (a) UV-Vis absorbance (dashed lines) and PL emission spectra (solid lines) of parent CsPbCl₃ NCs (black) and treated CsPbX₃ NCs produced from DDT-AIX₃ treatment of parent CsPbCl₃ nanocubes, (b) TEM image of parent CsPbCl₃ nanocubes, and (c-e) STEM images of treated CsPbX₃ NPs produced from DDT-AIX₃ treatment of CsPbCl₃ NCs. Insets in 4.6a show optical photographs of respective NC dispersions under illumination with 365 nm UV light and the inset in 4.6b shows the size distribution of parent CsPbCl₃ NCs.

The DDT-AIX₃ treated CsPbX₃ NCs differ from the as-synthesized CsPbCl₃ NCs in size and shape, as evident from a combination of scanning transmission electron microscopy (STEM) images (Figure 4.6b-e) and atomic force microscopy (AFM) images (Figure 4.7a, c, and e). The DDT-AIX₃ treated NCs are plate-shaped, with two of the dimensions increasing following treatment and the other dimension decreasing.

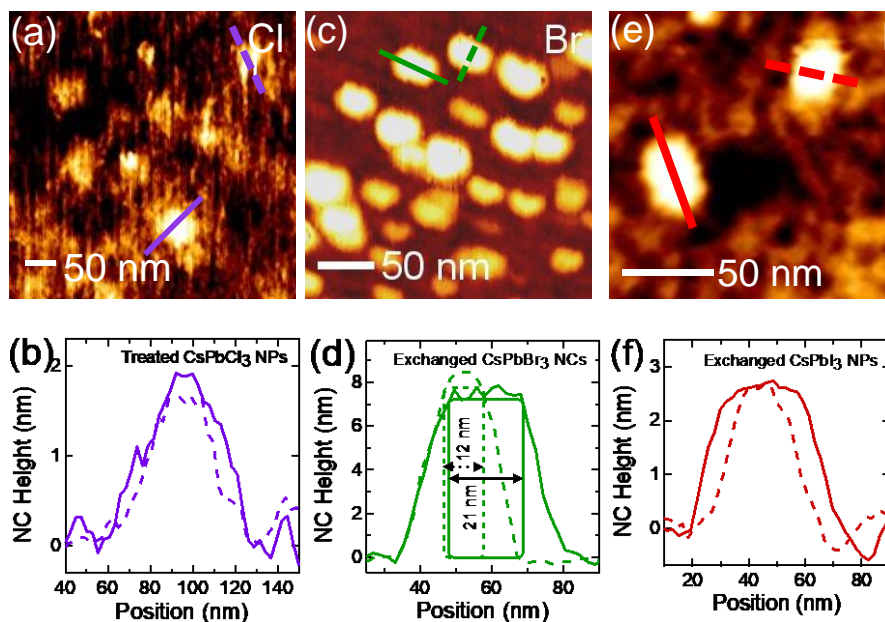


Figure 4.7 (a) Tapping mode AFM height image of treated CsPbCl₃ NCs & (b) height profile from the image shown in 4.7a along the NC indicated with violet line; (c) tapping mode AFM height image of exchange CsPbBr₃ NCs and (d) height profile from the image shown in 4.7c along the NC indicated with green line; and (e) tapping mode AFM height image of exchanged CsPbI₃ NCs & (f) height profile from the image shown in 4.7e along the NC indicated with red line.

STEM images of CsPbI₃ (Figure 4.6e) show what appear to be NPs with both vertical and horizontal orientations on the TEM grid. Such a distinct distribution is not as apparent with CsPbCl₃ and CsPbBr₃ (Figure 4.6c and d), but the treated NCs are clearly more anisotropic than the parent CsPbX₃ NCs. Atomic force microscopy reveals that the imaged DDT-AlX₃ treated CsPbX₃ NCs display particle heights of *ca.* 2 nm for CsPbCl₃ (Figure 4.7a and b), 5-9 nm for CsPbBr₃ (Figure 4.7c and d), and *ca.* 3 nm for CsPbI₃ (Figure 4.7e and f), which supports a NP morphology for all treated NCs. These AFM measured thicknesses correspond with 4, 15, and 5 monolayers, respectively, although this is from a smaller sample size. Since STEM is able to more rapidly capture larger sets of 2D images than AFM, we used AFM to primarily verify the 3D shape. Based on the

combination of STEM and AFM images, it appears that for CsPbCl₃ and CsPbBr₃ most NCs are laying flat in the STEM image, while for CsPbI₃ there appear to be many NCs that are standing up. The STEM images show average lateral edge lengths of 13 nm for both CsPbCl₃ and CsPbBr₃, and 22 nm for CsPbI₃, as determined from the histograms in **Figure 4.8**. The average thickness of the CsPbI₃ NCs as calculated from the standing up particles in the TEM and STEM images is 5±1 nm, which corresponds to 9 monolayers.

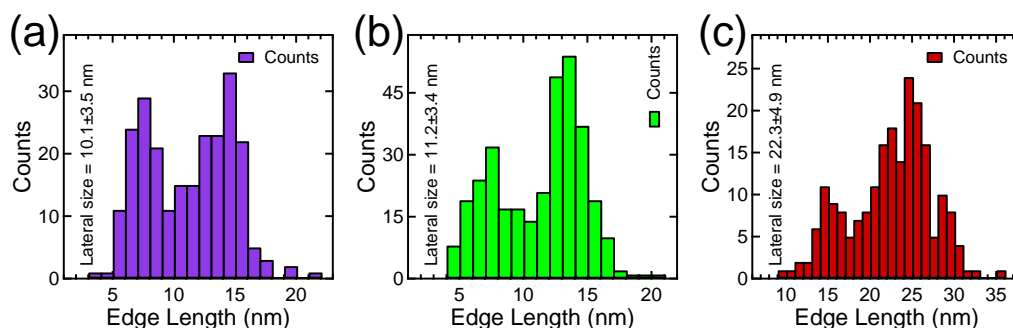


Figure 4.8 Size distributions from STEM images of: **(a)** treated CsPbCl₃, **(b)** exchanged CsPbBr₃, and **(c)** exchanged CsPbI₃ NCs synthesized through DDT-AIX₃ treatment of CsPbCl₃ NCs.

X-ray diffraction data provides further support for the formation of NPs. From the comparison of XRD patterns of parent CsPbCl₃ NCs and treated CsPbX₃ NPs, as shown in **Figure 4.9**, it can be seen that the {100} and {200} peak intensity remains high while the {110} peak intensity drops significantly upon DDT-AIX₃ treatment (**Figure 4.9a and b**). This drastic reduction in the {110} peak intensity and minimal change in the {100} and {200} diffraction peak intensities is attributed to exfoliation of the NCs along the (001) plane and fusion of these exfoliated NCs along the (010) and (100) planes during anion exchange reactions.^{31,226–229} Narrowing of the {200} diffraction peak shown in **Figure 4.9c**

further supports the increase in size of the treated NCs due to fusion of NCs in the lateral directions.

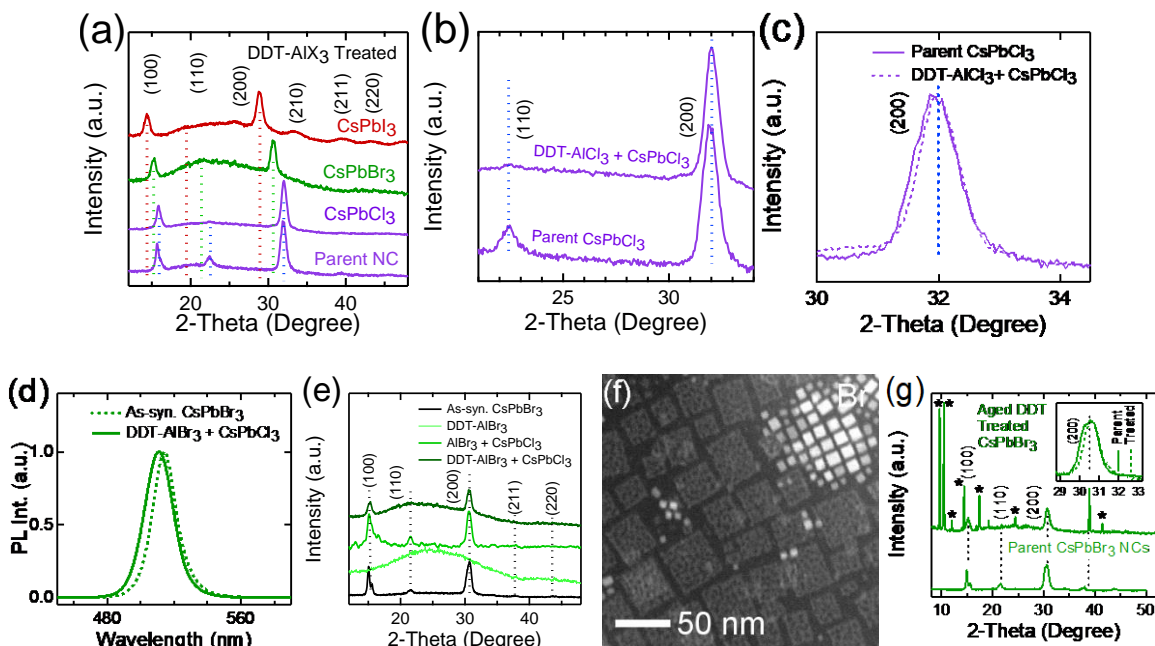


Figure 4.9 (a) XRD patterns of DDT-AIX₃ treated CsPbX₃ NCs produced from DDT-AIX₃ treatment of parent CsPbCl₃ nanocubes; comparison of (b) XRD patterns of parent CsPbCl₃ & treated CsPbCl₃ NCs synthesized through DDT-AlCl₃ treatment of CsPbCl₃ NCs; (c) (200) peaks in XRD patterns of as-syn. CsPbCl₃ & treated CsPbCl₃ NCs synthesized through DDT-AlCl₃ treatment of CsPbCl₃ NCs; (d) PL spectra of as-synthesized CsPbBr₃ & exchanged CsPbBr₃ NCs synthesized through DDT-AlBr₃ treatment of CsPbCl₃ NCs; (e) XRD patterns of as-synthesized CsPbBr₃ NCs, only DDT-AlBr₃, exchanged CsPbBr₃ NCs synthesized through only AlBr₃ treatment of CsPbCl₃ NCs, & exchanged CsPbBr₃ NCs synthesized through DDT-AlBr₃ treatment of CsPbCl₃ NCs; (f) STEM image of aged DDT treated CsPbBr₃ NCs; and (g) XRD patterns of as-synthesized CsPbBr₃ NCs & aged DDT treated CsPbBr₃ NCs (inset showing comparison of (200) diffraction peaks). In **4.9f** and **g**, the experiments were done with no additional AlX₃ in the parent CsPbBr₃ dispersion and * indicates Cs₄PbBr₆ formation.²²¹

To gain insight into the reactions taking place upon DDT-AIX₃ treatment, we collected Raman spectra, Fourier transform infrared absorbance (FTIR) spectra, and STEM-EDS elemental mapping images and line scans of untreated and treated CsPbX₃

NCs. This combination of measurements shows that oleate ligands desorb from the surface and Al containing species (e.g., $\text{Al}(\text{OH})_3$, $\text{Al}(\text{OH})_2\text{X}$, $\text{Al}(\text{OH})\text{X}_2$, etc.), thiol-derived species (i.e., thiolates and thioethers), and excess halide ions passivate the NC surfaces. The STEM-EDX elemental mapping images of CsPbBr_3 NCs presented in **Figure 4.10** confirm that Cs, Pb, and Br are present on the treated NCs. The presence of Cl in the NC region indicates that the exchange reaction does not result in complete exchange of Br^- for Cl^- . However, Cl^- is likely only passivating the surface and is not distributed throughout the bulk of the crystal, as the PL maximum ($\lambda_{\text{max}} = 511 \text{ nm}$) in treated NCs is similar to that for pure as-synthesized CsPbBr_3 NCs ($\lambda_{\text{max}} = 514 \text{ nm}$), as shown in **Figure 4.9d**. The surface adsorption of Cl^- is likely to reduce the presence of surface halide vacancies, particularly when combined with DDT passivation, thus helping to explain the large increase in PL intensity. The XRD spectra of as-synthesized CsPbBr_3 NCs and exchanged CsPbBr_3 NCs, as shown in **Figure 4.9e**, further support that Cl^- ions remain only at the treated NC surface.

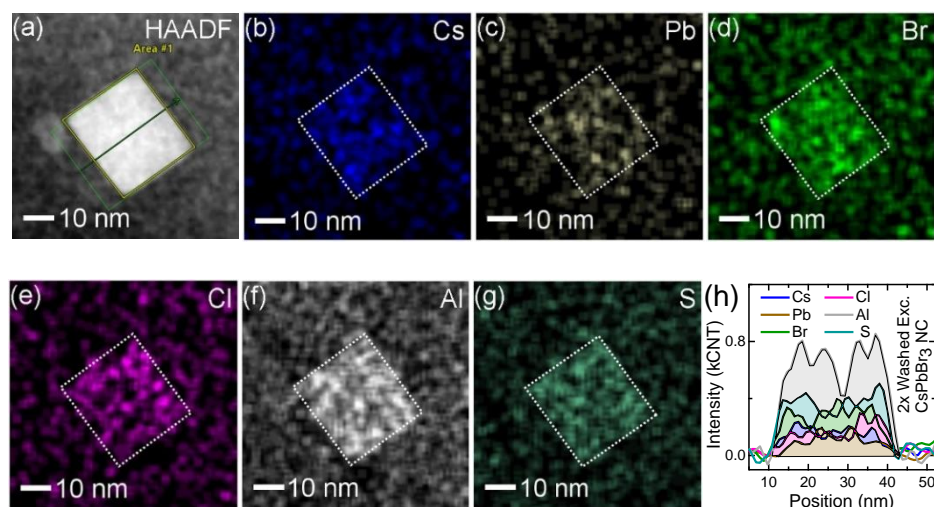


Figure 4.10 (a) HAADF-STEM image and (b-g) STEM-EDS elemental mapping images of Cs, Pb, Br, Cl, Al, & S of a 2x washed treated CsPbBr₃ NC; and (h) STEM-EDS line scan of the 2x washed treated NC shown in the HAADF-STEM image in 4.10a.

Figure 4.10f clearly show the presence of aluminum on the treated NCs, likely originating from adsorbed Al-containing species on the treated NC surfaces. Notably, most of the Al(OH)₃ precipitates out during the anion exchange reaction, which is supported by STEM-EDS elemental mapping images of these precipitates as shown in **Figure 4.11**.

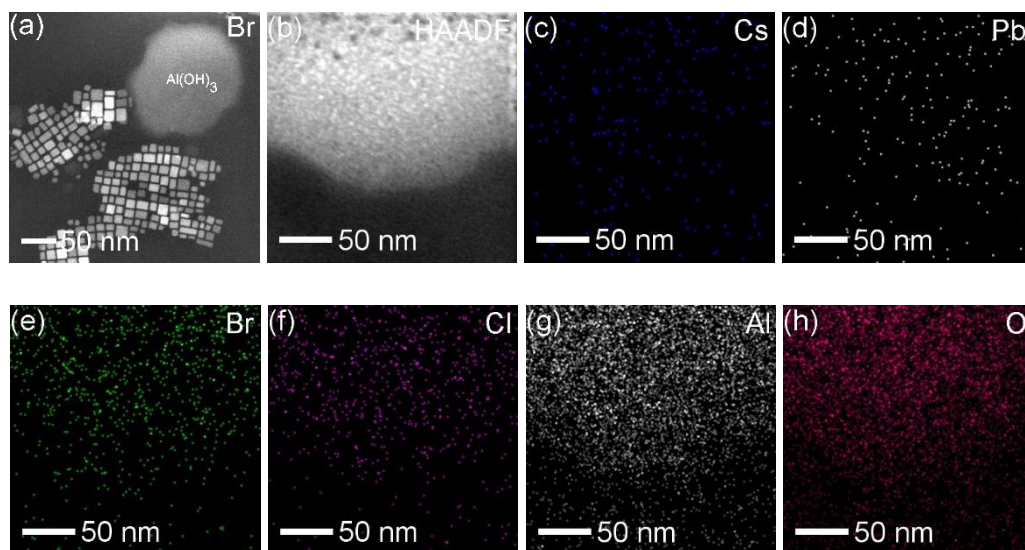


Figure 4.11 (a) HAADF-STEM image of exchanged CsPbBr₃ NCs synthesized through AlBr₃ treatment of CsPbCl₃ NCs, (b) Al(OH)_nX_{3-n} precipitates resulting from the synthesis, and (c-h) STEM-EDS elemental mapping images of Cs, Pb, Br, Cl, Al, & O of the Al(OH)_nX_{3-n} precipitate shown in **4.11b**.

It is not clear what form of the aluminum complex is binding to the surface. At the least, Al³⁺ ions are not doping the treated NCs during anion exchange reactions, as Al³⁺-doped CsPbBr₃ NCs would show blue-shifted PL spectra ($\lambda_{\text{max}} = 460$ nm) and sometimes dual PL emission spectra ($\lambda_{\text{max}} = 460$ nm and 515 nm).^{224,225} The STEM-EDS elemental mapping (**Figure 4.10g**) and STEM-EDS line scans (**Figure 4.10h**) of unwashed and 2x washed treated NCs show that sulfur is present on the treated NCs, as also observed in our previous work.¹⁴ Raman spectra shown in **Figure 4.12a** confirm the presence of this DDT species in the form of thiolate ions or thioethers with the disappearance of the S-H stretching mode after treatment of CsPbCl₃ NCs with DDT-AlX₃ solutions.

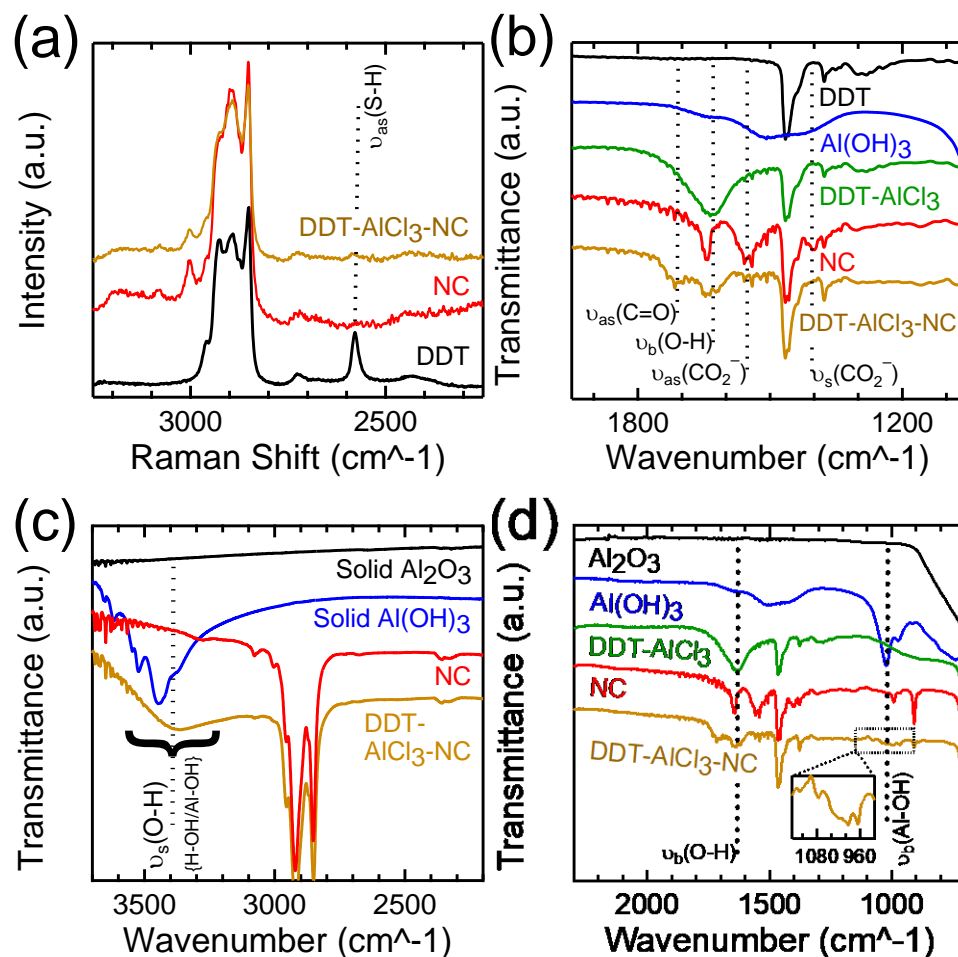


Figure 4.12 (a) Raman spectra of DDT, parent CsPbCl₃ NCs, & treated CsPbCl₃ NCs synthesized through DDT-AlCl₃ treatment of CsPbCl₃ NCs; FTIR spectra of (b) DDT, Al(OH)₃, DDT-AlCl₃, parent CsPbCl₃ NCs, & treated CsPbCl₃ NCs; and (c, d) Al₂O₃, DDT-AlCl₃, Al(OH)₃, parent CsPbCl₃ NCs, & treated CsPbCl₃ NCs.

The FTIR data shows that Al(OH)_nX_{3-n} is formed and oleate ligands are protonated following DDT-AlX₃ treatment. To clearly assign the hydroxyl group of Al(OH)_nX_{3-n} formed upon hydrolysis, FTIR spectra of Al₂O₃, Al(OH)₃, as-synthesized NCs, and treated NCs are compared in **Figure 4.12b-d**. Broad bands show up near 1000 and 3400 cm⁻¹ that are assigned to the bending and stretching modes of the HO-Al groups from Al(OH)_nX_{3-n} formation.^{230,231} Both of these bands also show up in the spectra of the DDT-AlCl₃ treated NCs, indicating clearly that Al(OH)_nX_{3-n} species are being formed and are not removed

during NC purification. Based on the STEM-EDS data, we suspect these $\text{Al(OH)}_n\text{X}_{3-n}$ species are coordinated to the NC surface. The conversion of carboxylate groups to carboxylic acid groups upon DDT- AlCl_3 treatment is evident from the disappearance of the 1404 and 1542 cm^{-1} peaks from the symmetric and asymmetric stretching modes of oleate ions and the emergence of a peak from the COOH mode at 1710 cm^{-1} . This protonation of the COO^- groups may be attributed to either reactions with DDT or H^+ produced via hydrolysis of AlX_3 .¹⁴

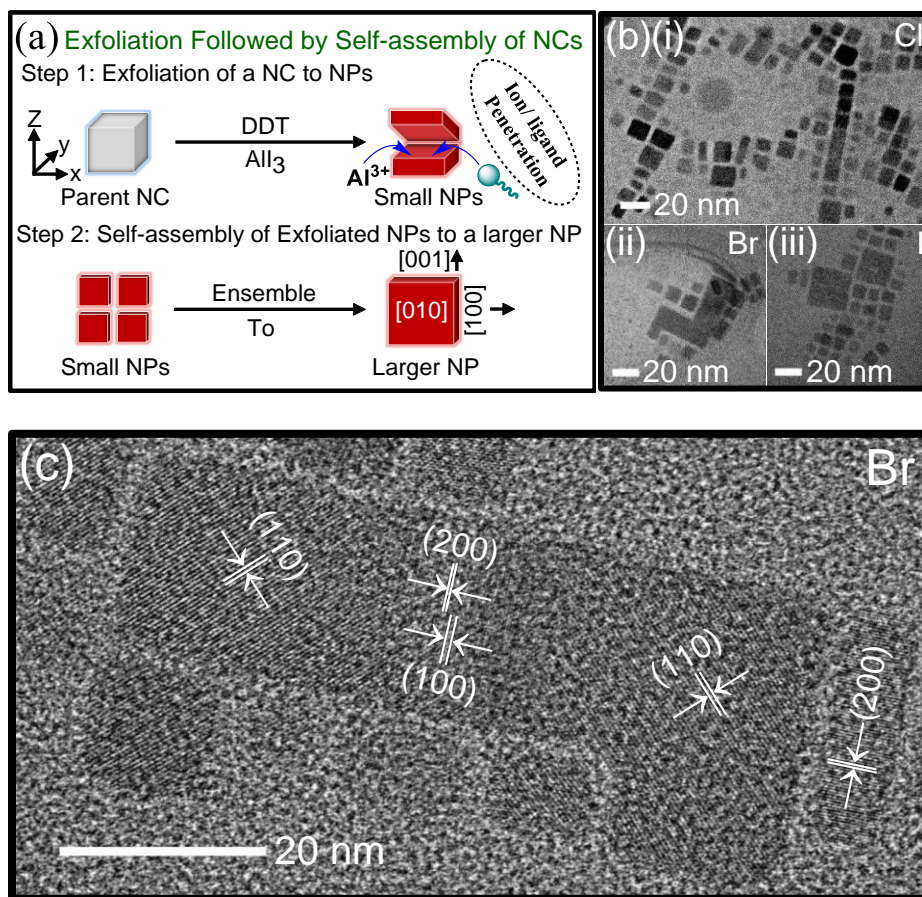


Figure 4.13 A schematic presentation of self-assembly and fusion of parent NCs into NPs; **(b and c)** TEM images of assemblies of treated CsPbX₃ NCs showing the larger fused NPs and **(c)** lattice fringes of larger fused CsPbBr₃ NPs.

As anion exchange reactions and desorption of parent ligands appear to occur simultaneously, we propose that NP formation occurs through exfoliation, followed by assembly and fusion, as illustrated in **Figure 4.13a**. This proposed mechanism is largely based upon TEM images, as shown in **Figure 4.13b and c**, and time-dependent absorbance and emission spectra, as shown in **Figure 4.14**. The time-dependent absorbance and emission spectra rule out the formation of NPs via dissolution and recrystallization processes occurring during DDT-AlX₃ treatment. If dissolution and recrystallization did occur, we would expect to see a rapid decrease in absorbance followed by an increase in

absorbance, but the absorbance upon DDT-AlX₃ addition does not decrease, see **Figure 4.14**. The TEM images in **Figure 4.13b** and **c** suggest that the NCs self-assemble and then fuse together, thereby forming larger NPs. In **Figure 4.13c** different lattice fringes are apparent in different areas of the large NP, which could originate from the fusion of the different particles.

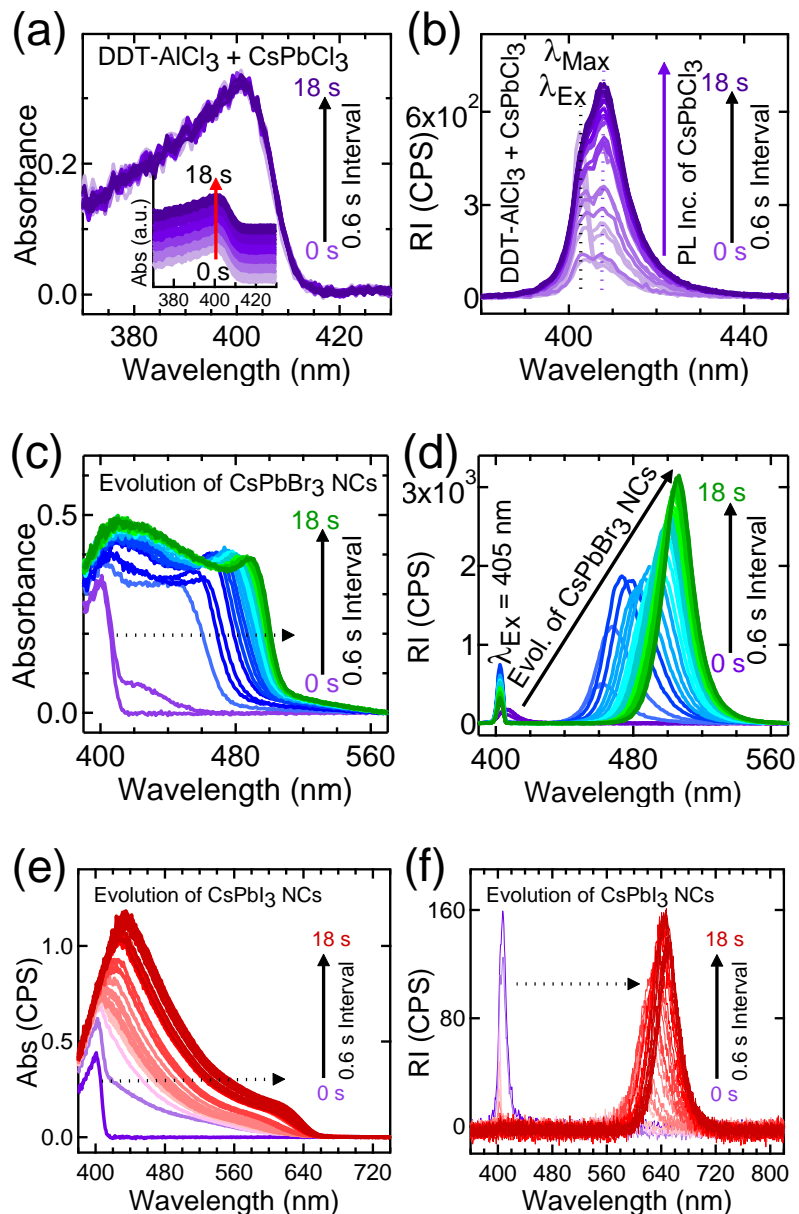


Figure 4.14 (a-f) Time-dependent absorbance and PL (relative irradiance = RI) of treated CsPbCl₃, exchanged CsPbBr₃ NCs, and CsPbI₃ NCs after addition of DDT-AIX₃ solutions over the first 18 seconds.

Interestingly, based on aging studies of CsPbBr₃ nanocubes with only DDT added to them (i.e., no AIX₃), these particles also form NPs, although over a much longer time frame. From the STEM image of 3-month to one-year old DDT treated CsPbBr₃ NCs (with no AIX₃ added) in **Figure 4.9f**, it is clearly seen that most of the parent CsPbBr₃ nanocubes

turn into NPs. The large image contrast between the original nanocubes and the formed NPs supports the thin nature of the NPs. Self-assembly followed by NC fusion is strongly supported in **Figure 4.9f**, where thinner NPs with *ca.*50 nm edge length can be observed alongside of close-packed parent CsPbBr₃ NCs with edge lengths of *ca.*10 nm. Comparison of XRD patterns of untreated and old DDT treated CsPbBr₃ NCs as shown in **Figure 4.9g** further confirms the formation of NPs as the {110} diffraction peak almost disappears after one-year storage of NCs with DDT surface ligands. We suspect that the rapid halide exchange after adding DDT-AIX₃ solution into the parent NC dispersions increases the reactivity of the NCs and increases the opportunity for DDT penetration and NC exfoliation into plate-shaped NCs.^{228,229,232}

Freshly treated NCs with freshly made DDT-AIX₃ solutions show high Φ_{PL} of up to 47% for violet emitters and 65% for blue emitters ($\lambda_{\text{max}} = 410$ nm for violet emitters and 450-460 nm for blue emitters), near 100% for green emitters, and 81% for red emitters, as displayed in **Figure 4.15a**. These Φ_{PL} values are significantly higher than previously reported record Φ_{PL} values for CsPbCl₃ and CsPbI₃ NPs of 2%³¹ and 12%,³¹ respectively, and slightly higher than previous reports for CsPbBr₃ NPs of 28-94%,^{31,215,217,220–222,233} To gauge the reproducibility of Φ_{PL} , we synthesized and characterized four separate batches of DDT-AIX₃ treated CsPbCl₃, CsPbCl_{3-x}Br_x, CsPbBr₃, and CsPbI₃ NCs, as detailed in **Table 4.2**. The average Φ_{PL} values are 22±4% for violet emitters, 54±8% for blue emitters, 91±13% for green emitters, and 75±6% for red emitters.

Table 4.2 shows the minimum Φ_{PL} , median Φ_{PL} , maximum Φ_{PL} , and average Φ_{PL} from four separate batches of DDT-AIX₃ treated CsPbCl₃, CsPbCl_{3-x}Br_x, CsPbBr₃, and CsPbI₃ NCs.

Treated NCs	Min. Φ_{PL} (%)	Median Φ_{PL} (%)	Max. Φ_{PL} (%)	Avg. Φ_{PL} (%)
CsPbCl ₃ on 1-5 Days	15	21	28	22±4
CsPbCl ₃ after 10 Days	30	39	47	38±8
CsPbCl _{3-x} Br _x on 1-5 Days	43	50	65	54±8
CsPbBr ₃ on 1-5 Days	69	97	98	91±13
CsPbI ₃ on 1-5 Days	63	75	81	75±6

Table 4.3 Lifetimes (τ_1 & τ_2), components (B_1 & B_2), and average lifetimes (τ_{avg}) of as-synthesized CsPbCl₃ NCs and DDT-AIX₃ treated CsPbX₃ NCs.

As-syn. NCs	τ_1 (ns)	B_1	τ_2 (ns)	B_2 (ns)	$\tau_{avg.}$ (ns)
CsPbCl ₃ (2 nd Exp Fitted)	0.34	0.17	9.5	0.00073	1.3
Treated NCs					
CsPbCl ₃ (2 nd Exp Fitted)	2.3	0.036	28.8	0.0061	20.3
CsPbCl _{3-x} Br _x (2 nd Exp Fitted)	3.9	0.03	10.3	0.0091	6.8
CsPbBr ₃ (2 nd Exp Fitted)	5.9	0.026	14.9	0.008	9.8
CsPbI ₃ (2 nd Exp Fitted)	13.8	0.016	27.8	0.012	22.2

*Second-exponential model, $F(t) = A + B_1 \exp(-t/\tau_1) + B_2 \exp(-t/\tau_2)$ is used to fit the PL lifetime curve. In this equation, τ_1 & τ_2 represent the time constants and B_1 & B_2 represent the amplitudes of the fast and slow components, respectively.

*Average lifetime is measured as $\tau_{avg.} = \frac{B_1 \tau_1^2 + B_2 \tau_2^2}{B_1 \tau_1 + B_2 \tau_2}$

All of these measurements were taken on a particular NP composition between 1 and 5 days after DDT-AIX₃ treatment, with between 8 and 14 measurements of Φ_{PL} conducted at various times in that window. Violet emitters show even higher average Φ_{PL} of $38 \pm 8\%$ after 10-days of treatment. The time-resolved PL lifetimes of the DDT-AIX₃ treated NCs are 5 to 17 times greater than the as-synthesized CsPbCl₃ nanocubes, as shown in **Figure 4.15b** and **Table 4.3**.

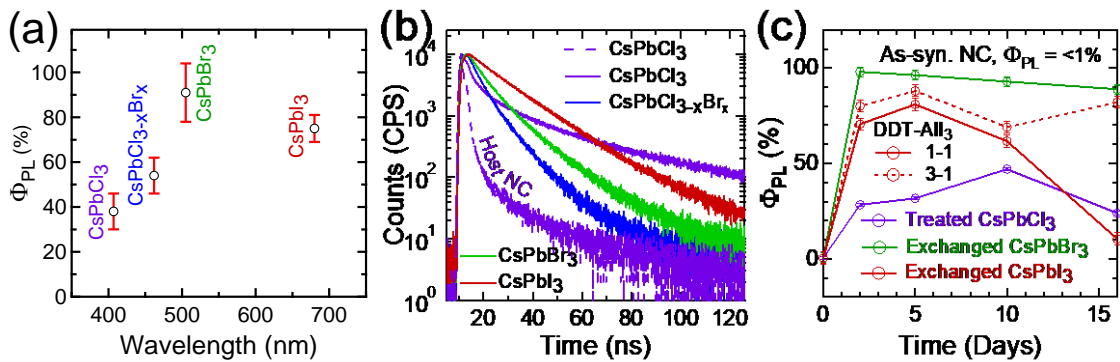


Figure 4.15 (a) Φ_{PL} & (b) time-resolved PL lifetime decays of AIX₃ treated CsPbX₃ NCs (violet dashed line indicates lifetime decay of parent CsPbCl₃ NCs in **4.15b**) and (c) time-dependent Φ_{PL} of treated CsPbX₃ NCs following DDT-AIX₃ treatment. Both Φ_{PL} and PL lifetimes in **4.15a** and **b** were collected within 1-5 days after the DDT-AIX₃ treatment.

In addition to showing high Φ_{PL} , the DDT-AIX₃ treated CsPbX₃ NCs are relatively stable under ambient conditions when stored in capped glass vials, as shown in **Figure 4.16**.

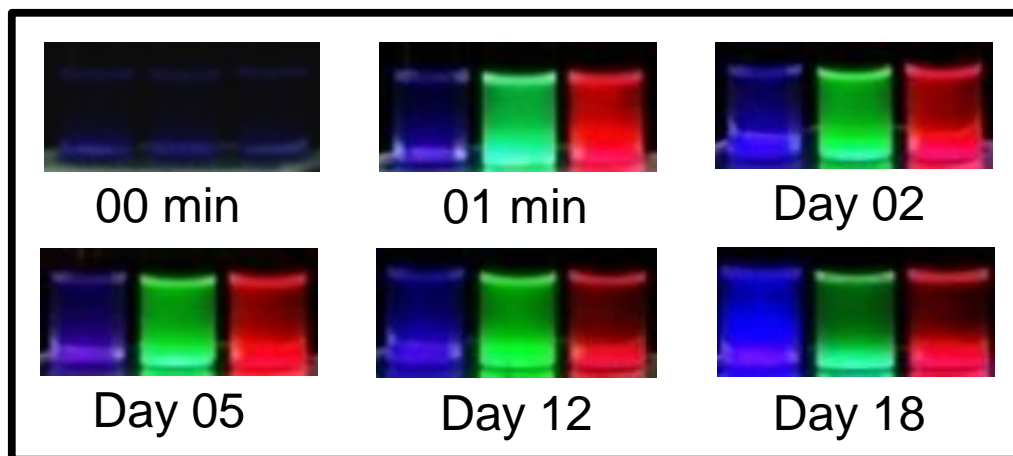


Figure 4.16 Time-dependent optical images of CsPbCl₃ NPs, CsPbBr₃ NPs, and CsPbI₃ NPs synthesized through DDT-AIX₃ treatment of CsPbCl₃ nanocubes.

In this study, most of the DDT-AIX₃ treated NCs retain 80-90% of their maximum Φ_{PL} even after 15-18 days, as shown in **Figure 4.15c and 4.16**, which we attribute primarily to surface passivation of treated NCs by both DDT and AIX₃ derived species. Treated CsPbI₃ NCs are less stable than those of violet and green emitters in terms of retaining Φ_{PL} ; however, the stability of treated CsPbI₃ NCs can be enhanced through varying the concentration of DDT (dotted red line in **Figure 4.15c**).

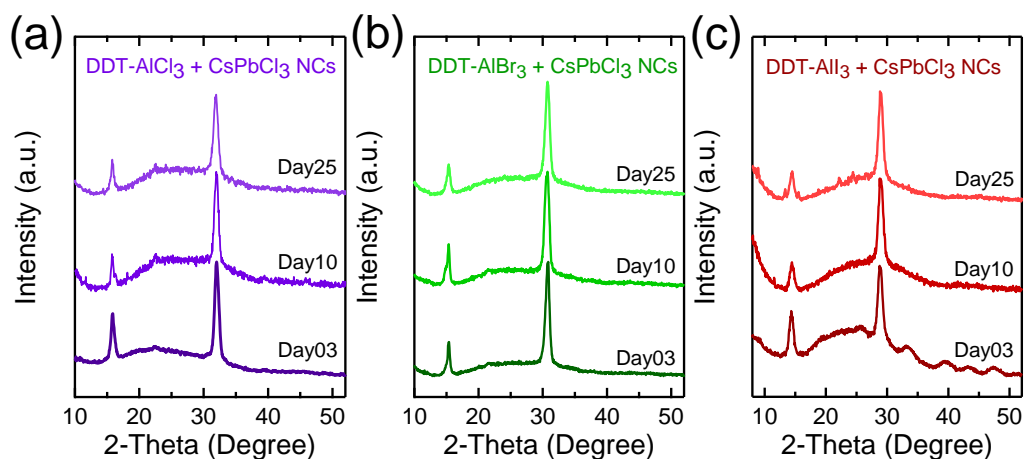


Figure 4.17 Time-dependent XRD patterns of: **(a)** treated CsPbCl_3 NCs, **(b)** exchanged CsPbBr_3 NCs, and **(c)** exchanged CsPbI_3 NCs synthesized through DDT- AlX_3 treatment of CsPbCl_3 NCs. XRD data were collected on the same day of preparation or one day after preparation.

Time-dependent optical images and XRD patterns collected over a 25-day period, as shown in **Figure 4.16 and 4.17**, support the stability observed in the PL measurements, as no change in crystallinity is observed.

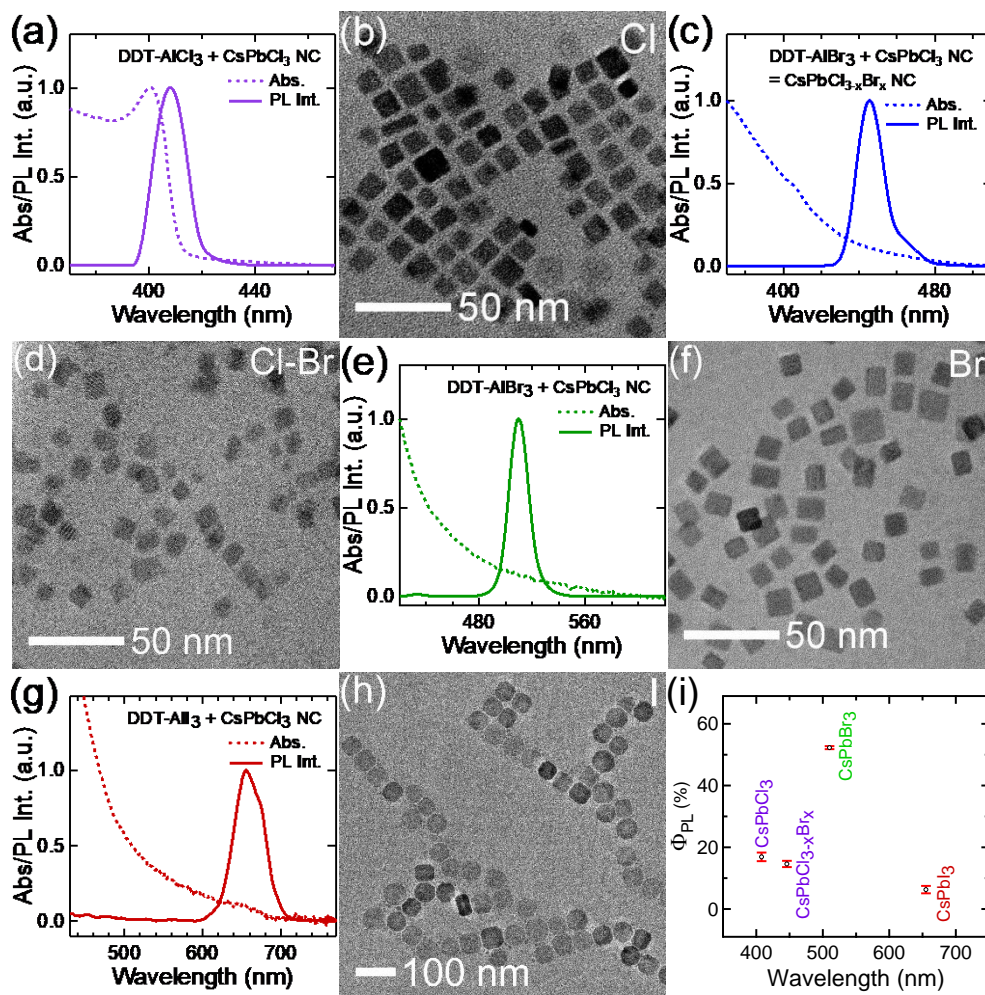


Figure 4.18 Optical absorbance & PL emission spectra and TEM images of more than 6-month old (a, b) treated CsPbCl₃ NCs, (c, d) partially exchanged CsPbCl_{3-x}Br_x NCs, (e, f) exchanged CsPbBr₃ NCs, (g, h) exchanged CsPbI₃ NCs, and (i) λ_{max} vs Φ_{PL} of 6-month old treated CsPbX₃ NCs synthesized through DDT-AlX₃ treatment of CsPbCl₃ NCs.

Interestingly, these treated NCs are even luminescent and maintain similar shape and size after 200-days of storage in capped vials in ambient conditions, as shown by the optical absorbance & PL emission spectra, TEM images, and Φ_{PL} displayed in **Figure 4.18** for 200-day old treated NCs. This new route to synthesize highly stable and highly luminescent CsPbX₃ NCs, along with the fundamental insights obtained, should be of high interest for optoelectronic devices.

4.4 Conclusion

Post-synthesis treatment of CsPbX₃ NCs with AlX₃ and DDT provides a route to produce primarily plate-shaped CsPbX₃ nanocrystals with superior Φ_{PL} and good long-term stability. The resulting violet, green, and red NPs have reproducible lateral size of 13-22 nm with average thicknesses of 4-15 monolayers along {010} facets. In this method AlX₃ acts as the halide source as it undergoes hydrolysis to form Al(OH)_nX_{3-n}, while DDT acts primarily as a surface ligand. We suspect both exfoliation facilitated by ligand penetration and assembly and fusion of the exfoliated NCs lead to these observed NPs. This combined approach of simultaneously adding a halide source and surface ligand provides an attractive route to simultaneously manipulate the optical properties and NC morphology of metal-halide nanocrystals.

CHAPTER 5. EFFECTS OF SULFUR AND SELENIUM-BASED SURFACE LIGANDS ON PHOTOLUMINESCENCE AND PHOTOVOLTAIC PERFORMANCE OF $\text{Cs}_{0.15}\text{FA}_{0.85}\text{PbI}_3$ METAL-HALIDE PEROVSKITES

This work is under study. It still needs some experimental supports to finish this project. I am expecting this work will be done before my final thesis submission date. If not, I continue to work even after my graduation.

5.1 Introduction

Metal-halide perovskites are receiving enormous attention because of soaring power conversion efficiencies in photovoltaic cells from 3.8% in 2009 to more than 25.5% in 2020.^{21,118} Single A-site cation-based MAPbI_3 typically shows higher PCE than other pure A-site APbX_3 perovskites, but they lack stability due to hygroscopic and volatile methylammonium salts and decompose to PbI_2 in presence of humidity,^{234,235} illumination,²³⁶ and annealing temperature above 85 °C.²³⁷ For these reasons, only cesium (Cs), formamidinium-methylammonium (FA-MA),^{133,238} Cs-FA ,^{239–242} or Cs-FA-MA ²⁴³ and/or mixed anion combination of commonly Br-I ^{133,239,240,243,244} are an attractive alternative to MAPbI_3 for practical PV applications. However, none of perovskites, either in nanocrystals (NC) or bulk thin film formats, with these combinations are defect free and shows some drawbacks in terms of poor stability and quality NCs/ films.

To suppress these issues, surface ligand treatment technique can be an alternative engineering pathway to improve perovskite NC/ thin film quality and device performance *via* passivating the defect states within the materials and manipulating interfacial energetics within the device. To date, strategies such as compositional tuning;^{133,238,240,242,244–247} addition of excess salts,^{133,238,243,248–250} ionic liquids,^{251–255} and ligands in the precursor solution;^{256–260} and post-treatment of fabricated thin films by surface ligands have been

shown to reduce cation and/or anion segregation in the thin films.^{85,261–263} Zhou and his coworkers recently used $\text{Cs}_{0.83}\text{FA}_{0.17}\text{PbI}_{3-x}\text{Br}_x$ ($x = 0.8, 1.2, 1.5, \text{ and } 1.8$) composition to fabricate thin films with large grains and minimal defects at grain boundaries, which demonstrate good photostability at both room and elevated temperatures.²⁴⁶ Similarly, Bi and his coworkers showed that a small excess (3% wt) of PbI_2 used in mixed cation and mixed halide perovskite solar cells (PSCs) suppresses nonradiative charge carrier recombination and in turn increases the external electroluminescence quantum efficiency (EQE) to values of about 0.5%,²⁶⁴ whereas Yu and his coworkers showed addition of an optimum amount (0.5 mol%) of $\text{Pb}(\text{SCN})_2$ in the $\text{Cs}_{0.2}\text{FA}_{0.8}\text{PbI}_3$ precursor solution significantly enlarges the grains and enhances the PCE.²⁴⁸ In addition, ionic liquids including 1-butyl-3-methylimidazolium tetrafluoroborate,²⁶² methylammonium formate²⁵¹, etc. and additives including 2,2'-bipyridine and 2,2':6',2''-terpyridine;²⁶¹ mercapto-tetrazolium and phenylammonium iodide;⁸⁵ etc. are used in mixed-cation lead halide ($\text{Cs}_{0.12}\text{FA}_{0.88}\text{PbI}_3$)-based perovskite thin films to suppress open circuit voltage losses and hence enhance the PV performance.

Double cation-based PSCs have already shown promising efficiency as well as good moisture, thermal, and photo-stability. Significant effort has been given to come to this point mostly using solvent, composition, and interface engineering pathways. However, extensive interface and/or further precursor engineering pathways of $\text{Cs}_{0.15}\text{FA}_{0.85}\text{PbI}_3$ perovskite system using surface ligands, such as sulfur and selenium-based ligands is still unexplored. Both individual and combination of DDT and AlX_3 were shown to increase photoluminescence quantum yield (Φ_{PL}) of colloidal CsPbX_3 nanocrystal counterparts in our previous studies.^{14,79} But surface of colloidal nanocrystals

and thin films are very different to the same ligand treatment as performance of the fabricated thin film PV devices depends on interfacial energetic landscapes of the different stacking layers. Thus, effects of these ligands with and without combination aluminum trihalide in the interface of perovskite/carrier transport layers (CTLs) need to be explored.

In fabricating double cation-based hybrid $\text{Cs}_{0.17}\text{FA}_{0.83}\text{PbI}_3$ photovoltaics, 10-20% amount of CsX (CsX+MAI) salts were found to reduce the cation segregation under light illumination and annealing,²⁴⁹ we stick to the 15% CsI additives to fabricate $\text{Cs}_{0.15}\text{FA}_{0.85}\text{PbI}_3$ based photovoltaics as 15% CsI is considered an optimum amount of Cs(Cs-MA)-containing additive reported by other groups.^{239,240,248} In this report, we demonstrate the comparison and enhancement of binding nature of sulfur and selenium-based ligands towards I-based metal-halide perovskites in format of thin films. Effectiveness and performance of both type of ligands are demonstrated through fabrication and modification of $\text{Cs}_{0.15}\text{FA}_{0.85}\text{PbI}_3$ thin films and photovoltaic devices. As surface modification/ composition of $\text{Cs}_{0.15}\text{FA}_{0.85}\text{PbI}_3$ using S and Se-based ligands can be controlled through the amount of ligands included in the precursor, device efficiency can further be boosted up to 18% while maintaining film and device stability. This boost up in efficiency primarily comes from suppressing undercoordinated lead atoms on thin film surface left by excess PbI_2 containing precursor solution. When an excess of PbI_2 is present aluminum halides combined with thiols may serve as an effective surface ligand combination which contributes to reproducible PCE over 17-18% and good device stability.

5.2 Experimental Details

5.2.1 Materials and Chemicals

Ultra-dry CsI (99.99%, Alfa Aesar), formamidinium iodide (FAI, Greatcell Solar), lead(II) iodide (99.99%, TCI), anhydrous N, N-dimethylformamide (DMF, 99.98%, DriSolv[®]), anhydrous dimethyl sulfoxide (DMSO, 99.9%, SeccoSolv[®]), 2-propanol (IPA, 99.5%, Alfa Aesar), toluene (99.8%, Alfa Aesar), indium tin oxide (ITO)-coated glass substrates (15 Ω/\square , Tinwell Technology), poly (triarylamine) (PTAA, Sigma Aldrich), C₆₀ (99.5%, Nano-C), bathocuproine or 2,9-Dimethyl-4,7-diphenyl-1,10-phenanthroline (BCP, >99%, TCI), aluminum (Al, 99.99%, Angstrom Engineering), anhydrous AlX₃ (99.99%, AlCl₃ 99.98%, metal basis, Alfa Aesar), Diethyl ether (DEE, 99.99%, seccoSolv), anhydrous chlorobenzene (99.8%, Acros Organics), 1-dodecanethiol (DDT, >95%, TCI), thiophenol (TP, 99+%, TCI), 4-methoxybenzenethiol (MBT, TCI), phenylselenol (PS, 98%, Acros Organics), phenylselenenyl bromide (PSB, 98%, Alfa Aesar), and Benzeneseleninic acid (BSA, 97%, TCI) are used as received.

5.2.2 Device Fabrication and Characterization

For the Cs_{0.15}FA_{0.85}PbI₃ perovskite photovoltaic devices, 2.0×2.0 cm² patterned ITO-coated glass substrates (15 Ω/\square) were tested each side with the multimeter and were labelled on the glass side. Before depositing perovskite solution on the patterned ITO-coated glass substrates, substrates were cleaned with successive sonication in a detergent solution (sodium dodecyl sulfate, Sigma-Aldrich), deionized (DI) water, acetone, and isopropanol baths for 10 minutes. After drying with compressed air, all the cleaned and dried substrates were then treated with UV-ozone for 10 minutes to remove all the organic

contaminants. Immediately after UV-Ozone treatment, substrates were transferred inside of a N₂-filled glove for depositing hole-transporting and perovskite layers.

Inside of the N₂-filled glove box, 100 μL PTAA solution (1.5 mg PTAA per 1 mL toluene was dissolved and stirred for 2-3 hours at room temperature) was then uniformly drop-cast and spun-cast on the cleaned patterned ITO-coated glass substrates at 6000 rpm for 30 s. After spin-casting of PTAA layer, all the substrates are put on the hot-plate, started annealing at 100 °C from room temperature, and then kept annealing at 100 °C for 10 minutes. PTAA coating and annealing are performed under constant glove purging at 5 and 9 mbar (O₂ and H₂O level were less than 0.1 ppm) while keeping blower off. After 10 minutes of annealing, all the substrates were removed from the hot-plates and were allowed to cool down normally.

While processing and fabricating PTAA layer, Cs_{0.15}FA_{0.85}PbI₃ perovskite precursor solution was prepared by dissolving a mixture of PbI₂ (629.2 mg), FAI (190.0 mg), CsI (50.7 mg), and/or degassed anhydrous pyridine (~7.9 mg, Py, 99.5%, Alfa Aesar) in a 1 mL mixture of DMF and DMSO solution (4:1) under vortex-mixing and mild heating condition at ~70 °C for 50 minutes to assist dissolving without using any magnetic stir bar. Precursor solution was always brought to room temperature normally before spin-casting. On the ITO/PTAA layers, 115-120 μL of Cs_{0.15}FA_{0.85}PbI₃ precursor solution were uniformly drop-cast and spun-cast at 6000 rpm for 20 seconds without any ramp time. 200 μL of anhydrous chlorobenzene was then dropped on the spinning substrate after 10 s of reaching 6000 rpm, resulting in the formation of uniform and brownish transparent films which turn into black upon instantly annealing on a preheated hot plate at 100 °C for 15 minutes. Perovskite layer coating and annealing are performed under constant glove

purging at 5 and 9 mbar (O_2 and H_2O level were less than 0.1 ppm) while keeping blower off (it is very important to keep spin-coater lid open except while spinning). Nitrogen blow inside of the spin-coater was also used in between every film fabrication. After 10 minutes of annealing, all the substrates were removed from the hot-plates and were allowed to cool down normally.

For surface ligand treatments, 200 μ L of surface ligand solution (10 mM solution in either IPA or DEE) was then drop-cast on the dark $CS_{0.15}FA_{0.85}PbI_3$ films and left to sit for 2-3 seconds before spinning at 3000 rpm for 20 seconds without any ramp time. To remove the unbound ligands, 200 μ L of chlorobenzene with no ligand added were drop-cast and rinsed the treated films via spinning at the same speed of 3000 rpm for 20s. The process was repeated for 2 times for every treated samples.

Both control (ITP/PTAA/Perovskite) and treated (ITP/PTAA/Perovskite-Ligands) films were transferred thermal evaporator without air exposure. Over control and treated perovskite light absorbing layer, 30 Å of C_{60} and 80 Å of BCP layers were sequentially deposited at a rate of 1 Å/s and 0.5 Å/s, respectively, at a pressure of *ca.* 2.0×10^{-6} mbar. Similarly, final layer of 1000 Å of Al electrode was thermally deposited through a shadow mask, that defined 12 cells of 0.1 cm^2 per substrate, on top of all the ETLs at *ca.* 2.0×10^{-6} mbar to complete the fabrication photovoltaic devices.

5.2.3 Device Testing and Active Characterization

All the devices were tested inside of the glove box using a solar simulator (ABET technologies, 11002) at 100 mW/cm^2 illumination (AM 1.5G). The solar intensity was adjusted using a calibrated photodiode (Thorlabs, FDS1010-CAL) with a KG3 filter. Thin

films on glass substrates were probed for morphology using scanning electron microscopy (*SEM*), absorbance, photoluminescence, and PDS measurement. On the other hand, thin films on ITO/PTAA were probed for structure using XRD patterns, binding nature of surface ligands using XPS, and energy level measurements using UPS and IPES.

5.2.4 Thin Film Characterization

5.2.4.1 Absorbance

Optical absorption spectra were collected using an Ocean Optics QE pro high-performance spectrometer with 80 ms integration time and 5 micron slit width. Absorbance was obtained using a Thermo Scientific Evolution 201 UV-Visible Spectrophotometer with 50 ms integration time and 2 nm slit widths.

5.2.4.2 Fluorescence

Photoluminescence spectra of $\text{Cs}_{0.15}\text{FA}_{0.85}\text{PbI}_3$ thin films were collected using a 532 nm laser (Thorlabs, CPS532) and an Ocean Optics QE pro high-performance spectrometer with 1100 ms integration time and 100 micron slit width in an open fixed geometry to reduce reabsorption effects.

5.2.4.3 Scanning Electron Microscopy (SEM)

SEM samples were prepared on the (1 x 1 cm²) non-patterned ITO-coated glass substrates in the identical manner as the PV devices except all the ETLs and top contact and probed with a Hitachi S-4300 SEM with an accelerating voltage of 10 kV.

5.2.4.4 X-Ray Diffraction

Samples were prepared in the same manner as described in the SEM section. The X-ray diffraction patterns (θ - 2θ scans) were taken on a Bruker-AXS D8 DISCOVER diffractometer with Cu K α radiation ($\lambda = 1.5418 \text{ \AA}$) operating at 40 kV and 40 mA.

5.2.4.5 Photoelectron Spectroscopic (PES) Measurements

Samples were prepared in the same manner as described in the SEM section. X-ray photoelectron spectroscopy (XPS) spectra were collected with PHI 5600 ultrahigh vacuum system (UHV) with a hemispherical electron energy analyzer, and Al K α source (1486.6 eV, PHI 04-548 dual anode X-ray source) for excitation, and a pass energy of 117.4 eV for survey and 58.7 eV for small region scan.

5.3 Results and Discussion

In our previous studies and this study, reproducibly thiols, specially dodecanethiol (DDT) is found to be effective at passivating CsPbCl₃ and CsPbBr₃ NCs while maintaining PL properties and long-term colloidal stability of both Cl and Br-based colloidal NCs as shown in **Figure 5.1a and b**.^{14,15} However, when we used DDT to modify CsPbI₃ NCs, it was unable to enhance both PL properties and stability of the colloidal NCs as shown in **Figure 5.1c**.

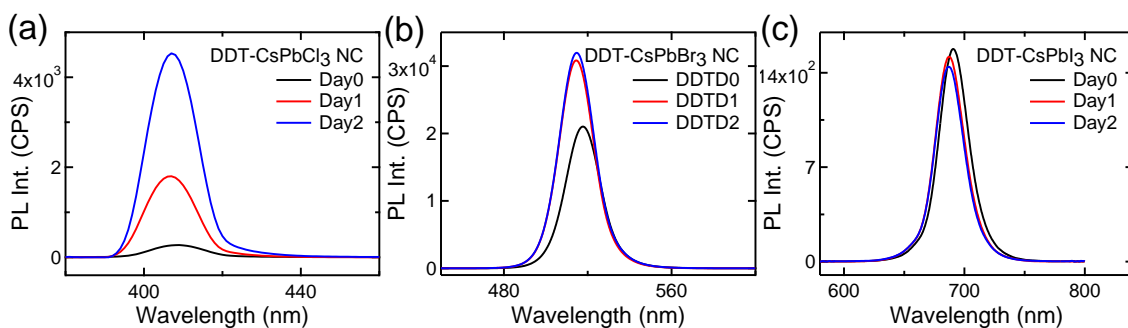


Figure 5.1 Time-dependent PL Spectra of colloidal (a) CsPbCl₃ NCs, (b) CsPbBr₃ NCs, and (c) CsPbI₃ NCs upon addition of dodecanethiol.

As thiols in the form of thiolate ions are suspected to bind the NC surface, it might be suspected that thiolate ions may not passivating the surface enough or penetrating the CsPbI₃ NC surface because of size difference between S and I as depicted in **Figure 5.2a**.^{14,79}

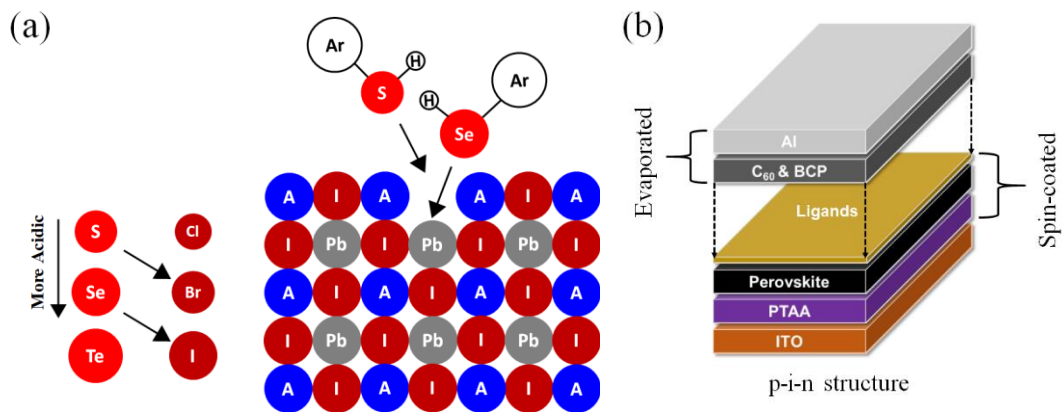


Figure 5.2 Schematics of (a) comparison of S and Se-based ligands and (b) p-i-n structure of fabricated perovskite photovoltaic devices with perovskite layer being modified with both S and Se-based ligands.

Considering the difference in the surface properties of NC and thin films, we also fabricated high quality $\text{Cs}_{0.15}\text{FA}_{0.85}\text{PbI}_3$ thin films and photovoltaic devices in purpose of applying surface modifiers and observing the effectiveness of the surface ligands in enhancing the device performance and stability. To verify the quality of thin films before surface treatments, we fabricated some control devices using the $\text{Cs}_{0.15}\text{FA}_{0.85}\text{PbI}_3$ thin films only. All the fabricated devices show pretty good power PCE with less hysteresis. PCE of the champion control device reaches over 16% as shown in **Figure 5.3a** and **Table 5.1**.

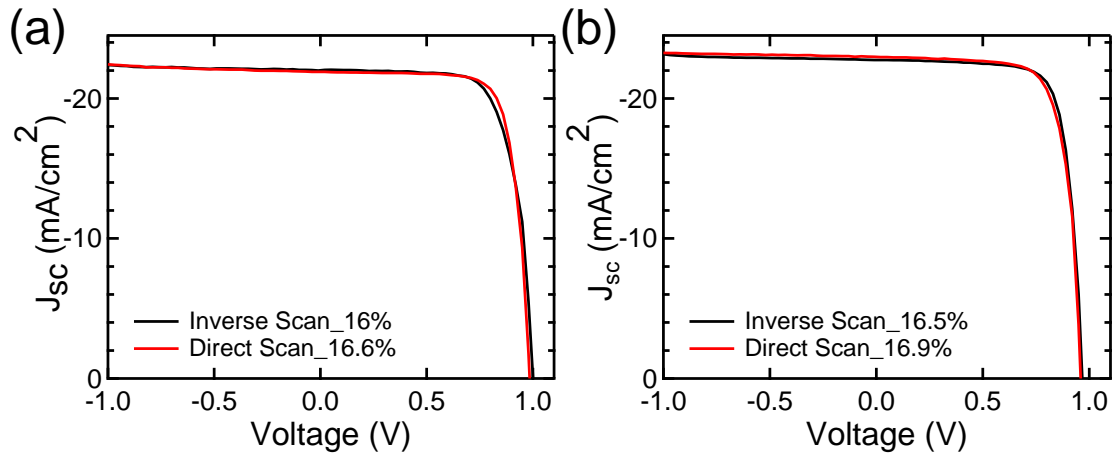


Figure 5.3 Direct and inverse scans of (a) ITO/PTAA/ $\text{Cs}_{0.15}\text{FA}_{0.85}\text{PbI}_3$ +5% PbI_2 /C₆₀/BCP/Al and (b) ITO/PTAA/ $\text{Cs}_{0.15}\text{FA}_{0.85}\text{PbI}_3$ +5% PbI_2 +Pyridine/C₆₀/BCP/Al photovoltaic devices.

Table 5.1 J-V parameters from the devices described in **Figure 5.3a and b** measured from J_{sc} to PCE under 1 sun illumination.

Pyridine Effect	Scan Type	J_{sc} (mA/cm²)	V_{oc} (V)	FF	PCE (%)
w/o	Inverse Scan	-21.9	0.99	0.77	16.6
	Direct Scan	-22.0	1.00	0.73	16.0
w/	Inverse Scan	-23.0	0.96	0.75	16.5
	Direct Scan	-22.7	0.97	0.77	16.9

$CS_{0.15}FA_{0.85}PbI_3$ PV device was fabricated with excess 5% PbI_2 w.r.t to 1.3 M concentration of precursor perovskite solution on the top of glass-ITO/PTAA as depicted in **Figure 5.1b**. As excess PbI_2 in fabrication of other PV devices, specially $CS_{0.05}(FA_{0.83}MA_{0.17})_{0.95}Pb(I_{0.83}Br_{0.17})_3$,²⁴³ $MAPbI_3$,²⁶⁵ and $CS_{0.15}FA_{0.85}PbI_3$ photovoltaics is proved to enhance the efficiency.²⁶⁴ However, devices are found to be unstable, losing 90% of their performance within a day. So, small amount (7.9 mg/mL) of degassed pyridine solution (99.5%, Alfa Aesar) is added in the perovskite precursor solution and fabricated devices shows better device performance, high FF, and J_{sc} with negligible hysteresis as shown in **Figure 5.3b and Table 5.1**. Small amount of pyridine in the perovskite precursor solution provide better film coverage on the hydrophobic PTAA films and high quality perovskite film formation as indicated by the reduction in PbI_2 peak intensity in XRD patterns of perovskite thin films fabricated with and without pyridine as shown in **Figure 5.4**.

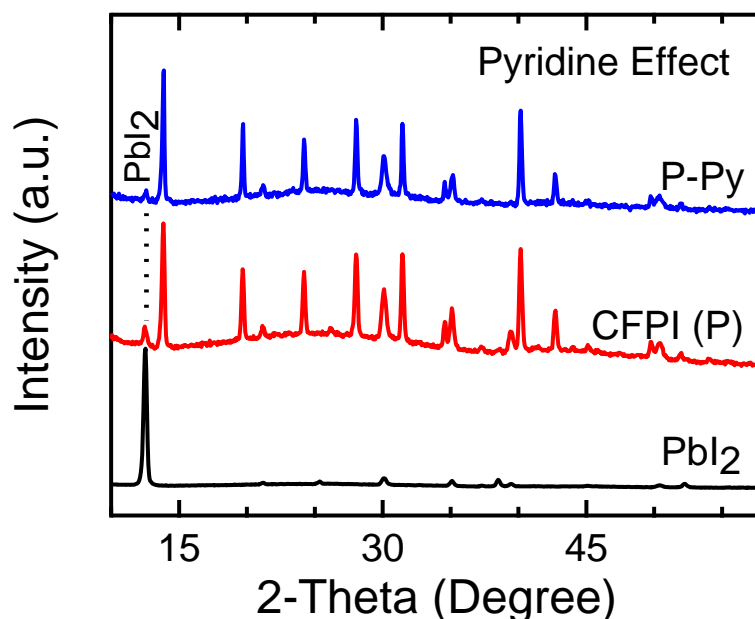


Figure 5.4 Comparison of XRD patterns of perovskite thin films fabricated with and without pyridine. In Figure 5.4, CFPI = $\text{Cs}_{0.15}\text{FA}_{0.85}\text{PbI}_3$, P = perovskite, and Py = pyridine.

After verifying the thin film quality through device fabrication and testing, we modify the thin film surface via application of thiol surface ligands in the HTL/perovskite and perovskite/ETL interfaces. Details of thin film fabrication and surface treatment were carried out following the procedure discussed in the experimental sections. Goal was to further address instability issue and enhance PCE of fabricated devices *via* applications of the surface ligands first between perovskite layer and electron-transporting layers and at the same time, binding nature of S- and Se-based ligands will be compared in terms of difference in acidic nature of both types of ligands. To observe the surface ligand binding nature of both S and Se-based ligands after surface treatment of fabricated thin films of composition of $\text{Cs}_{0.15}\text{FA}_{0.85}\text{PbI}_3$, we probed both pristine and treated perovskite films with

XPS analysis. **Figure 5.5** shows small region scans of C1s, S2p, and Se3d of S and Se-based ligands treated $\text{Cs}_{0.15}\text{FA}_{0.85}\text{PbI}_3$ thin films.

However, from XPS analysis it has been found that thiols are also unable to bind to $\text{Cs}_{0.15}\text{FA}_{0.85}\text{PbI}_3$ thin films as we did not observe any sulfur in the small region XPS scan of S2p orbital as shown in **Figure 5.5a**. Probably, thiolate ions may not be forming and thus unable to passivate the $\text{Cs}_{0.15}\text{FA}_{0.85}\text{PbI}_3$ thin film surface because thiols are unable to deprotonate in absence of any bases.^{14,79}

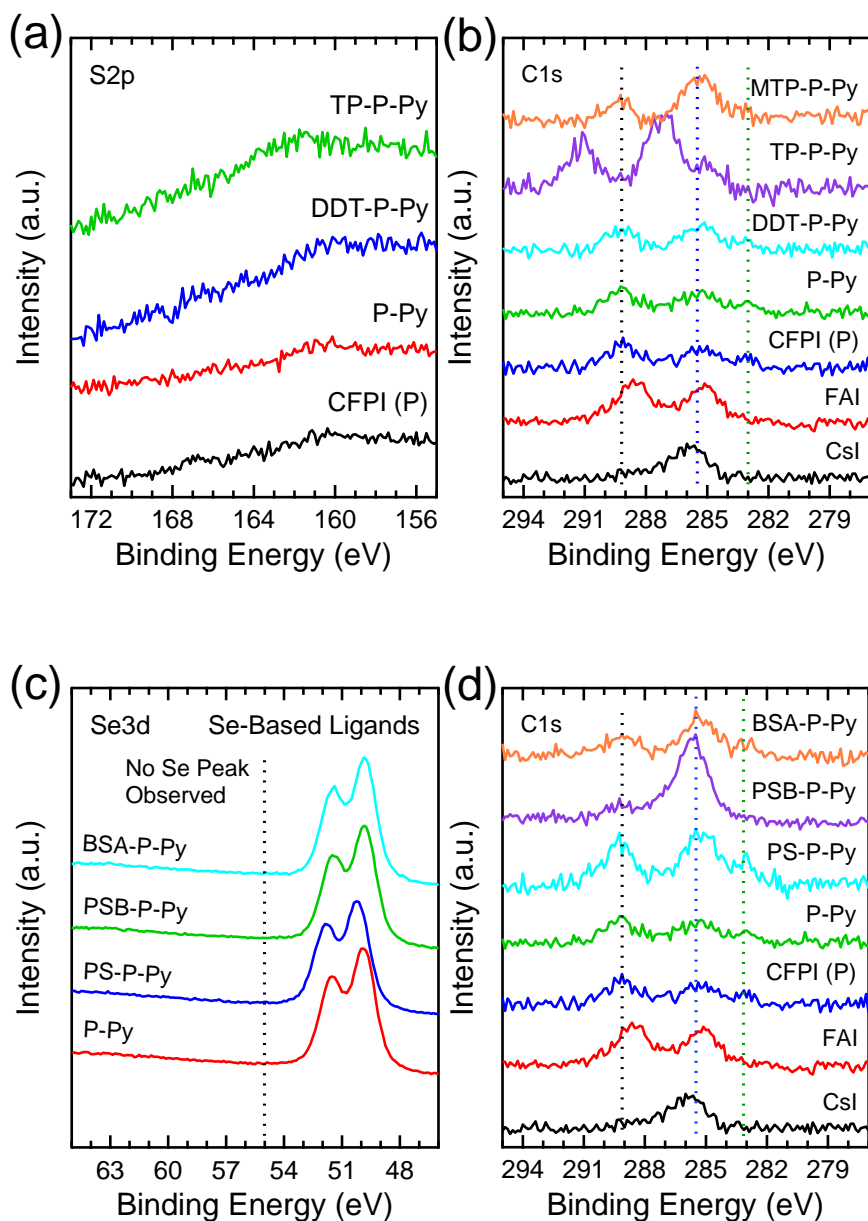


Figure 5.5 High resolution XPS small region scans of **(a and b)** S2p region and C1s region of S-based ligands treated $\text{Cs}_{0.15}\text{FA}_{0.85}\text{PbI}_3$ thin films, **(c and d)** Se3d region and C1s of Se-based ligands treated $\text{Cs}_{0.15}\text{FA}_{0.85}\text{PbI}_3$ thin films. In Figure 5.5a-d, CFPI = $\text{Cs}_{0.15}\text{FA}_{0.85}\text{PbI}_3$, P = perovskite, Py = pyridine, DDT = dodecanethiol, TP = thiophenol, MTP = 4-methoxythiophenol, PS = phenylselenol, PSB = phenylselenenyl bromide, and BSA = benzeneseleninic acid.

As thiolate ions may not passivating the surface enough or penetrating the I-based perovskite surface because of size difference between S and I, selenolate ions in this case

may passivate the I-based perovskite surface because of comparable size of Se and I as well as due to higher reactive nature of Se-based ligands (e.g., phenylselenol) to the metal center because of stronger acidic nature of selenols.²⁶⁶ So, to test this hypothesis, we also apply Se-based ligands to both I-based metal-halide perovskite NCs and thin films. But like S-based ligands, Se-based ligands did not show PL intensity enhancement of NCs (totally quenched the PL intensity) or strong binding to the I-based metal-halide perovskite thin films as indicated by the absence of Se3d peak around 55 eV in the small region scans of Se3d regions as shown in **Figure 5.5c**. But when we analyze C1s region of both S and Se-based ligands, we actually observe some indication of binding of both S and Se-based ligands as indicated by the C1s peak near 285.5 eV, where peaks near 289 eV are due to formamidinium carbons. Meaning, small fraction of both S and Se-based ligands is probably binding to the $\text{Cs}_{0.15}\text{FA}_{0.85}\text{PbI}_3$ thin film surface as supported by the enhancement of PL intensity upon treatment of both S and Se- based ligands to the $\text{Cs}_{0.15}\text{FA}_{0.85}\text{PbI}_3$ thin films as shown in **Figure 5.6b and d**, though we did not observe any noticeable changes in optical absorbance spectra as shown in **Figure 5a and c**.

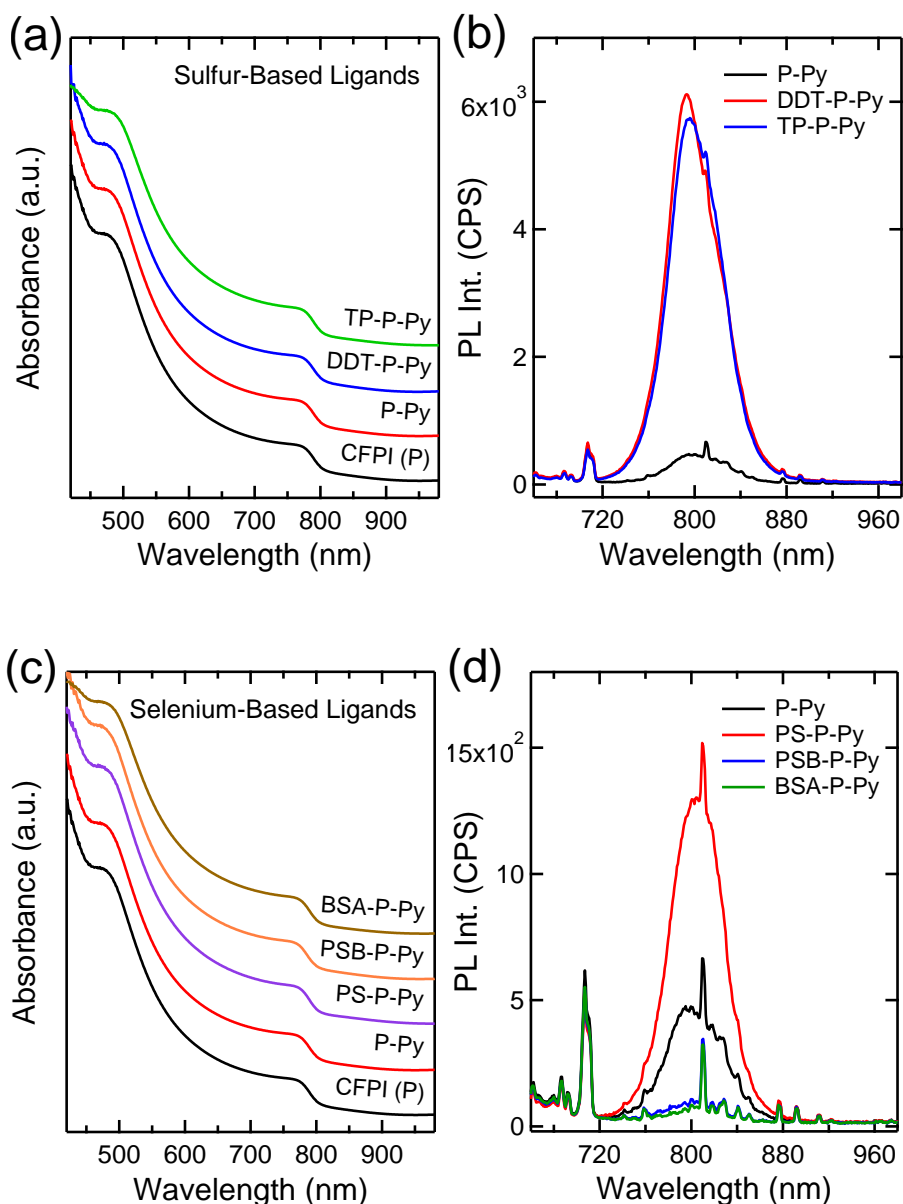


Figure 5.6 Comparison of optical absorbance and PL spectra of **(a and b)** pristine and S-based ligands treated $\text{Cs}_{0.15}\text{FA}_{0.85}\text{PbI}_3$ thin films and **(c and d)** pristine and Se-based ligands treated $\text{Cs}_{0.15}\text{FA}_{0.85}\text{PbI}_3$ thin films. In Figure 5.6a-d, CFPI = $\text{Cs}_{0.15}\text{FA}_{0.85}\text{PbI}_3$, P = perovskite, Py = pyridine, DDT = dodecanethiol, TP = thiophenol, MTP = 4-methoxythiophenol, PS = phenylselenol, PSB = phenylselenenyl bromide, and BSA = benzeneseleninic acid.

In addition, we also do not observe any changes in crystal perovskite structure as indicated by XRD patterns as shown in **Figure 5.7** upon S and Se-based ligand treatment.

However, we see some changes in film morphology upon PSB and BSA treatment. Probably, that is because both PSB and BSA are suspected to be binding through halide (Br) functional group and carboxylic acid functional group as indicated by the presence of higher amount of C1s peaks near 285.5 eV as shown in **Figure 5.5d**.

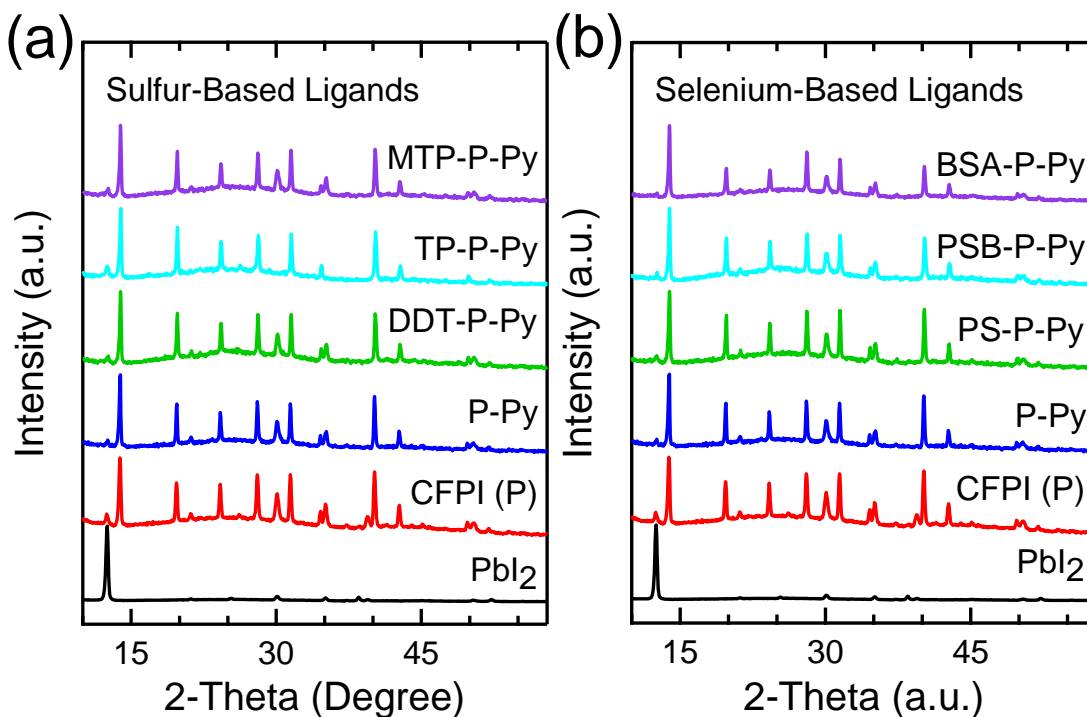


Figure 5.7 Comparison of XRD patterns of (a) pristine and S-based ligands treated $\text{Cs}_{0.15}\text{FA}_{0.85}\text{PbI}_3$ thin films and (b) pristine and Se-based ligands treated $\text{Cs}_{0.15}\text{FA}_{0.85}\text{PbI}_3$ thin films. In Figure 5.7a and b, CFPI = $\text{Cs}_{0.15}\text{FA}_{0.85}\text{PbI}_3$, P = perovskite, Py = pyridine, DDT = dodecanethiol, TP = thiophenol, MTP = 4-methoxythiophenol, PS = phenylselenol, PSB = phenylselenenyl bromide, and BSA = benzeneseleninic acid.

After treatment of thin films with both S and Se-based ligands, film morphology under scanning electron microscopy (SEM) as shown in **Figure 5.8** also support the XPS and XRD data. Pure thiols and selenols did not change the film morphology that much.

However, both PSB and BSA do some changes in film morphology as shown in **Figure 5.8 e and f**.

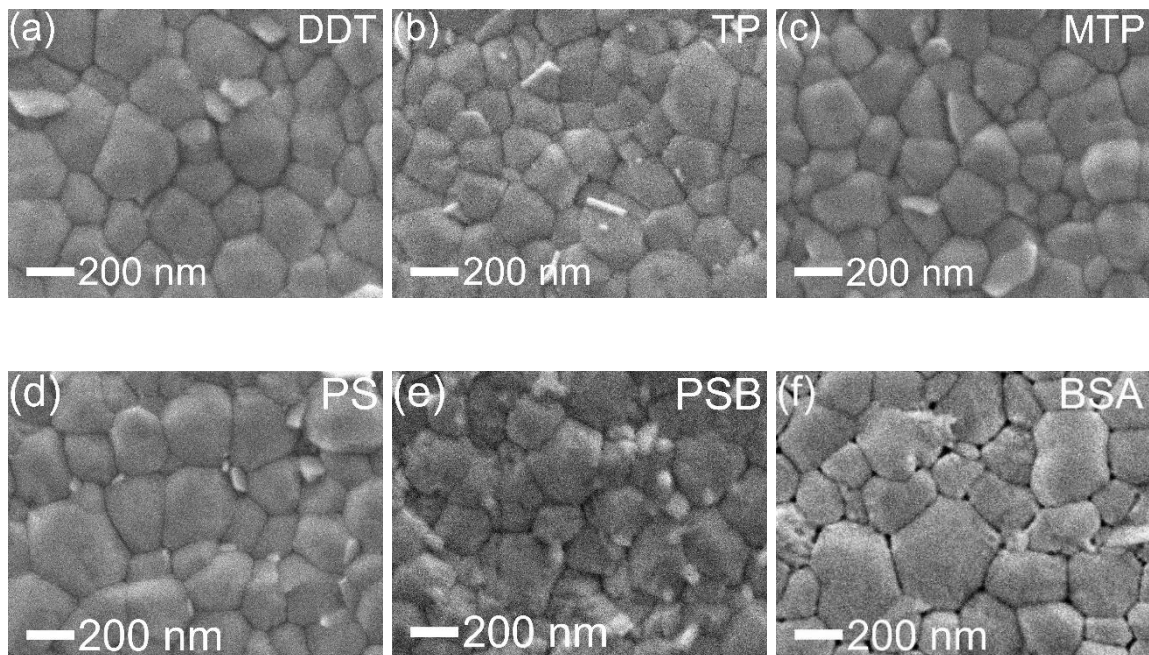


Figure 5.8 **Film morphology**: SEM images of **(a-c)** S-based ligands and **(d-f)** Se-based ligands modified thin films. In Figure 5.8, DDT = dodecanethiol, TP = thiophenol, MTP = 4-methoxythiophenol, PS = phenylselenol, PSB = phenylselenenyl bromide, and BSA = benzeneseleninic acid.

After verifying PL properties and film morphology of both S and Se-based ligands treated thin films, modified bulk thin films were used to fabricate p-i-n structured photovoltaic devices as shown in **Figure 5.2b** to further support the hypothesis if these ligand treatments can enhance the PCE and stability of the devices. However, like S-based ligands, Se-based ligands are to unable to enhance the performance of the devices as shown in **Figure 5.9**.

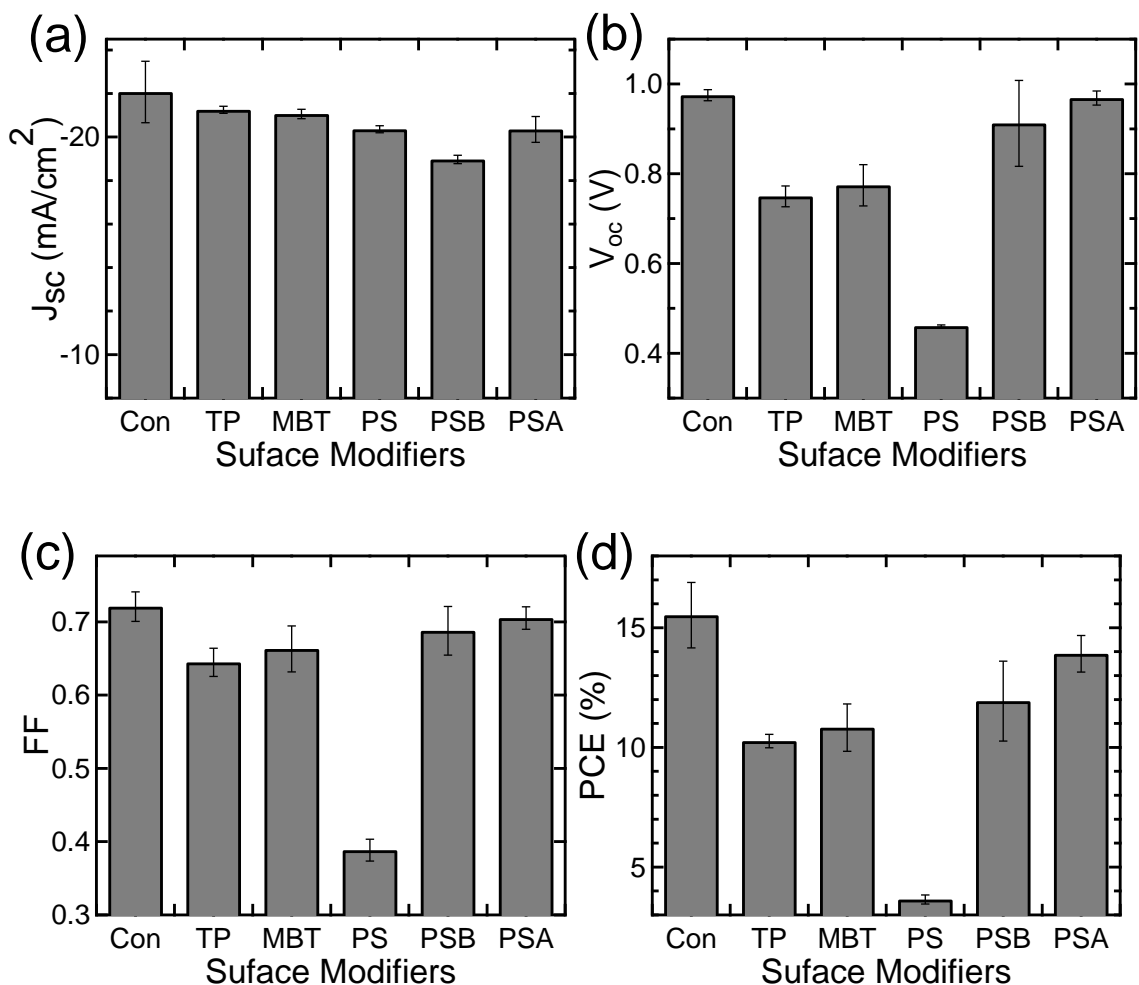


Figure 5.9 **PV Statistics and Stability**: (a-d) performance (J_{sc} , V_{oc} , FF, and PCE) of PVs using different surface ligand treated thin films. In Figure 5.9, Con = $Cs_{0.15}FA_{0.85}PbI_3$, DDT = dodecanethiol, TP = thiophenol, MTP = 4-methoxythiophenol, PS = phenylselenol, PSB = phenylselenenyl bromide, and BSA = benzeneseleninic acid.

Both S and Se-based ligands are unable to bind to the I-based thin films and unable to enhance efficiency of the device from our initial investigations. Thus, our future directions that should be explored is to enhance the reactivity of both thiol and selenol

ligands toward I-based thin films via simple acid-based chemical reactions and fabricate PV devices. If this route does not work out, we will apply surface ligands in-between hole-transporting and perovskite interface instead of in-between perovskite and electron-transporting interface. As it is thought that electron-transporting layer, C₆₀ used in this p-i-n structure might already be passivating the perovskite layer.

5.4 CONCLUSION

Extensive interface engineering of Cs_{0.15}FA_{0.85}PbI₃ perovskite photovoltaics using sulfur and selenium-based surface ligands is explored. We report a simple procedure to modify Cs_{0.15}FA_{0.85}PbI₃ thin films using sulfur and selenium-based surface ligands. But, post-treatment of such a thin film with a small amount of sulfur and selenium-based surface ligands is unable to enhance the device performance and stability. In our future endeavors, applications of thus reactivity enhanced surface ligands might enhance the photoluminescence of Cs_{0.15}FA_{0.85}PbI₃ perovskite thin films, power conversion efficiency, and stability of photovoltaic devices.

CHAPTER 6. SUMMARY AND PERSPECTIVE

6.1 Overall Summary of This Work

In this body of work, we have used facile synthetic methods, simple chemical reactions, tactical ligand engineering techniques, and some routine & state-of-the-art instrumental techniques to advance the frontiers of metal-halide perovskites and their applications. In the first work, we show evolution of very stable and efficient CsPbCl₃ NCs via a facile anion exchange reaction of CsPbBr₃ NCs with alkyltrichlorosilane. Alkyltrichlorosilanes (R-SiCl₃), very hygroscopic materials can be used as Cl-sources for rapid anion exchange with other CsPbBr₃ NCs via simple and room-temperature hydrolysis reactions. This anion exchange reaction via hydrolysis reactions of alkyltrichlorosilanes results in highly dispersible violet emitting NCs coated with siloxane shells. These violet-emitting siloxane coated CsPbCl₃ NCs show significantly improved stability and Φ_{PL} of up to 12% and are even stable in the presence of water, whereas traditional violet-emitting CsPbCl₃ NCs synthesized through other routes rapidly degrade in the presence of water.

In the next work, enhancement of Φ_{PL} and stability of green-emitting CsPbBr₃ NCs with dodecanethiol (DDT) by post-synthetic surface treatments is shown. Traditional green-emitting CsPbBr₃ NCs show relatively poor PL properties (Φ_{PL} of 38±3%) and stability when synthesized with traditional methods. But post-synthetic treatment with reactive dodecanethiol surface ligands reproducibly yields highly stable NCs with near unity Φ_{PL} (~100%) for a range of synthetic conditions and initial Φ_{PL} of the as-synthesized NCs. A mechanistic investigation shows that thiol addition leads to thioether formation *via* the thiol-ene reaction with octadecene, oleic acid, and oleylamine. Both thiolates and thioethers are suspected to bind to undercoordinated Pb atoms on the NC surfaces, and this

surface binding and enhancement of PL properties can be rapidly accelerated through exposure to blue or UV light.

In another work, to advance the frontiers of all the colloidal CsPbX₃ NCs, their PL properties, and morphology, we report a ligand mediated anion exchange reaction that transforms CsPbCl₃ nanocubes into anisotropic CsPbX₃ nanoplates (NPs) through adding a mixture of dodecanethiol (DDT) and AlX₃ (X = Cl, Br, I) to a solution of CsPbCl₃ nanocubes. The anion-exchanged NCs consist of mostly plate-shaped CsPbX₃ NCs along {010} facets. Although DDT or AlX₃ treatment alone results in increased Φ_{PL} , the combination of both DDT and AlX₃ leads to the formation of plate-shaped NCs, higher Φ_{PL} , and improved stability as compared to when only one of these is used. In this process AlX₃ acts as the halide source as it undergoes hydrolysis to form Al(OH)_nX_{3-n}, while DDT acts primarily as a surface ligand. We suspect both exfoliation facilitated by ligand penetration and assembly and fusion of the exfoliated NCs lead to these observed NPs. The NPs are highly emissive and stable due to the introduction of both an anion source and surface ligand. Nanoplates synthesized through DDT-AlX₃ ligand mediated anion exchange show Φ_{PL} of 47 and 65% for violet emitting CsPbCl₃ & blue emitting CsPbCl_{3-x}Br_x, respectively, near 100% for green emitting CsPbBr₃, and 81% for red emitting CsPbI₃, while maintaining good long-term stability over 200 days of treatment.

In my last work, translating the success in NCs to achieve the success in solution-processed perovskite thin films and their fabricated PV devices, mixed-cation Cs_{0.15}FA_{0.85}PbI₃ perovskite thin films are modified using different S- and Se-based surface ligands and effects of these surface ligands are tested *via* fabrication of photovoltaic devices. In this project, goal is to fabricate S- and Se-based surface ligands modified

$\text{Cs}_{0.15}\text{FA}_{0.85}\text{PbI}_3$ perovskite layers while comparing the binding nature of sulfur and selenium-based ligands. Thus, PL properties, morphology, and performance of modified $\text{Cs}_{0.15}\text{FA}_{0.85}\text{PbI}_3$ perovskite thin films as well as the binding nature of both S- and Se-based ligands to both I-based metal-halide perovskite NCs and thin films are investigated. It is found that both S- and Se-based ligands are unable to bind and enhance the efficiency of $\text{Cs}_{0.15}\text{FA}_{0.85}\text{PbI}_3$ perovskite thin films and their devices.

6.2 Future Research Plan

After completing my PhD, I will focus on a couple of areas: (i) improvement of fundamental understanding of degradation processes of metal-halide perovskite materials and their devices and (ii) enhancement of intrinsic material stability and extrinsic device stability through material combinations, material doping, and/or post-treatments with surface materials including surface ligands, counter ionic salts, ionic ligands, etc.

In addition, my goal is to play a role in helping commercialization of metal-halide perovskite-based photovoltaic devices by moving from small-format devices to large-format devices while maintaining the same scale of device performance and stability.

6.3 Career Research Interest

My interest is to work independently on synthesis of novel functional nano & micromaterials, surface chemistry of nanomaterials & solution-processed solid-state thin films, fabrication of thin films & optoelectronic devices, and photocatalysis. Research output I expect here is to synthesize and post-modify semiconducting materials for fine-tuned materials for (cost-)effective optoelectronic and other applications.

To do so, I will investigate the fundamental understanding of structure-property relationship and property-application relationship using the state-of-art instrumental techniques.

REFERENCES

- (1) Yoshikawa, A.; Matsunami, H.; Nanishi, Y. Development and Applications of Wide Bandgap Semiconductors. In *Springer, Berlin, Heidelberg*; 2007; pp 1–24.
- (2) Kittel, C. Introduction to Solid State Physics, 8th Edition. *Wiley Sons, New York, NY* **2004**.
- (3) Frenkel, J. On the Transformation of Light into Heat in Solids. I. *Phys. Rev.* **1931**, *37* (1), 17.
- (4) Wannier, G. H. The Structure of Electronic Excitation Levels in Insulating Crystals. *Phys. Rev.* **1937**, *52* (3), 191.
- (5) Hsiao, Y. C.; Wu, T.; Li, M.; Liu, Q.; Qin, W.; Hu, B. Fundamental Physics behind High-Efficiency Organo-Metal Halide Perovskite Solar Cells. *J. Mater. Chem. A* **2015**, *3* (30), 15372–15385.
- (6) Yang, Z.; Surrente, A.; Galkowski, K.; Bruyant, N.; Maude, D. K.; Haghghirad, A. A.; Snaith, H. J.; Plochocka, P.; Nicholas, R. J. Unraveling the Exciton Binding Energy and the Dielectric Constant in Single-Crystal Methylammonium Lead Triiodide Perovskite. *J. Phys. Chem. Lett.* **2017**, *8* (8), 1851–1855.
- (7) Graef, M. De; Mchenry, M. E. Structure of Materials: An Introduction to Crystallography, Diffraction, and Symmetry. *Cambridge Univ. Press* **2007**.
- (8) Yakunin, S.; Protesescu, L.; Krieg, F.; Bodnarchuk, M. I.; Nedelcu, G.; Humer, M.; De Luca, G.; Fiebig, M.; Heiss, W.; Kovalenko, M. V. Low-Threshold Amplified Spontaneous Emission and Lasing from Colloidal Nanocrystals of Caesium Lead Halide Perovskites. *Nat. Commun.* **2015**, *6*, 1–8.
- (9) Stoumpos, C. C.; Malliakas, C. D.; Peters, J. A.; Liu, Z.; Sebastian, M.; Im, J.; Chasapis, T. C.; Wibowo, A. C.; Chung, D. Y.; Freeman, A. J.; Wessels, B. W.; Kanatzidis, M. G. Crystal Growth of the Perovskite Semiconductor CsPbBr₃: A New Material for High-Energy Radiation Detection. *Cryst. Growth Des.* **2013**, *13* (7), 2722–2727.
- (10) De Roo, J.; Ibáñez, M.; Geiregat, P.; Nedelcu, G.; Walravens, W.; Maes, J.; Martins, J. C.; Van Driessche, I.; Kovalenko, M. V.; Hens, Z. Highly Dynamic Ligand

Binding and Light Absorption Coefficient of Cesium Lead Bromide Perovskite Nanocrystals. *ACS Nano* **2016**, *10* (2), 2071–2081.

- (11) Yettapu, G. R.; Talukdar, D.; Sarkar, S.; Swarnkar, A.; Nag, A.; Ghosh, P.; Mandal, P. Terahertz Conductivity within Colloidal CsPbBr₃ Perovskite Nanocrystals: Remarkably High Carrier Mobilities and Large Diffusion Lengths. *Nano Lett.* **2016**, *16* (8), 4838–4848.
- (12) Protesescu, L.; Yakunin, S.; Bodnarchuk, M. I.; Krieg, F.; Caputo, R.; Hendon, C. H.; Yang, R. X.; Walsh, A.; Kovalenko, M. V. Nanocrystals of Cesium Lead Halide Perovskites (CsPbX₃, X = Cl, Br, and I): Novel Optoelectronic Materials Showing Bright Emission with Wide Color Gamut. *Nano Lett.* **2015**, *15* (6), 3692–3696.
- (13) Wu, L.; Zhong, Q.; Yang, D.; Chen, M.; Hu, H.; Pan, Q.; Liu, H.; Cao, M.; Xu, Y.; Sun, B.; Zhang, Q. Improving the Stability and Size Tunability of Cesium Lead Halide Perovskite Nanocrystals Using Trioctylphosphine Oxide as the Capping Ligand. *Langmuir* **2017**, *33* (44), 12689–12696.
- (14) Uddin, M. A.; Mobley, J. K.; Masud, A. Al; Liu, T.; Calabro, R. L.; Kim, D.-Y.; Richards, C. I.; Graham, K. R. Mechanistic Exploration of Dodecanethiol Treated Colloidal CsPbBr₃ Nanocrystals With Photoluminescence Quantum Yields Reaching Near 100%. *J. Phys. Chem. C* **2019**, *123* (29), 18103–18112.
- (15) Uddin, M. A.; Glover, J. D.; Park, S. M.; Pham, J. T.; Graham, K. R. Growth of Highly Stable and Luminescent CsPbX₃ (X = Cl, Br, and I) Nanoplates via Ligand Mediated Anion Exchange of CsPbCl₃ Nanocubes with AlX₃. *Chem. Mater.* **2020**, *32* (12), 5217–5225.
- (16) Krieg, F.; Ochsenbein, S. T.; Yakunin, S.; Ten Brinck, S.; Aellen, P.; Süess, A.; Clerc, B.; Guggisberg, D.; Nazarenko, O.; Shynkarenko, Y.; Kumar, S.; Shih, C. J.; Infante, I.; Kovalenko, M. V. Colloidal CsPbX₃ (X = Cl, Br, I) Nanocrystals 2.0: Zwitterionic Capping Ligands for Improved Durability and Stability. *ACS Energy Lett.* **2018**, *3* (3), 641–646.
- (17) Koscher, B. A.; Swabeck, J. K.; Bronstein, N. D.; Alivisatos, A. P. Essentially Trap-Free CsPbBr₃ Colloidal Nanocrystals by Postsynthetic Thiocyanate Surface Treatment. *J. Am. Chem. Soc.* **2017**, *139* (19), 6566–6569.
- (18) Dutta, A.; Behera, R. K.; Pal, P.; Baitalik, S.; Pradhan, N. Near-Unity Photoluminescence Quantum Efficiency for All CsPbX₃ (X=Cl, Br, and I) Perovskite Nanocrystals: A Generic Synthesis Approach. *Angew. Chemie - Int. Ed.*

2019, 58 (17), 5552–5556.

- (19) Pan, J.; Shang, Y.; Yin, J.; De Bastiani, M.; Peng, W.; Dursun, I.; Sinatra, L.; El-Zohry, A. M.; Hedhili, M. N.; Emwas, A. H.; Mohammed, O. F.; Ning, Z.; Bakr, O. M. Bidentate Ligand-Passivated CsPbI₃ Perovskite Nanocrystals for Stable Near-Unity Photoluminescence Quantum Yield and Efficient Red Light-Emitting Diodes. *J. Am. Chem. Soc.* **2018**, *140* (2), 562–565.
- (20) Zhong, Q.; Cao, M.; Xu, Y.; Li, P.; Zhang, Y.; Hu, H.; Yang, D.; Xu, Y.; Wang, L.; Li, Y.; Zhang, X.; Zhang, Q. L-Type Ligand-Assisted Acid-Free Synthesis of CsPbBr₃ Nanocrystals with Near-Unity Photoluminescence Quantum Yield and High Stability. *Nano Lett.* **2019**, *xx* (xx), xxx–xxx.
- (21) Kojima, A.; Teshima, K.; Shirai, Y.; Miyasaka, T. Organometal Halide Perovskites as Visible-Light Sensitizers for Photovoltaic Cells. *J. Am. Chem. Soc.* **2009**, *131* (17), 6050–6051.
- (22) Schmidt, L. C.; Pertegás, A.; González-Carrero, S.; Malinkiewicz, O.; Agouram, S.; Mínguez Espallargas, G.; Bolink, H. J.; Galian, R. E.; Pérez-Prieto, J. Nontemplate Synthesis of CH₃NH₃PbBr₃ Perovskite Nanoparticles. *J. Am. Chem. Soc.* **2014**, *136* (3), 850–853.
- (23) Hao, M.; Bai, Y.; Zeiske, S.; Ren, L.; Liu, J.; Yuan, Y.; Zarrabi, N.; Cheng, N.; Ghasemi, M.; Chen, P.; Lyu, M.; He, D.; Yun, J. H.; Du, Y.; Wang, Y.; Ding, S.; Armin, A.; Meredith, P.; Liu, G.; Cheng, H. M.; Wang, L. Ligand-Assisted Cation-Exchange Engineering for High-Efficiency Colloidal Cs_{1-x}FaxPbI₃ Quantum Dot Solar Cells with Reduced Phase Segregation. *Nat. Energy* **2020**, *5* (1), 79–88.
- (24) Sanhira, E. M.; Marshall, A. R.; Christians, J. A.; Harvey, S. P.; Ciesielski, P. N.; Wheeler, L. M.; Schulz, P.; Lin, L. Y.; Beard, M. C.; Luther, J. M. Enhanced Mobility CsPbI₃ Quantum Dot Arrays for Record-Efficiency, High-Voltage Photovoltaic Cells. *Sci. Adv.* **2017**, *3* (10).
- (25) Li, F.; Zhou, S.; Yuan, J.; Qin, C.; Yang, Y.; Shi, J.; Ling, X.; Li, Y.; Ma, W. Perovskite Quantum Dot Solar Cells with 15.6% Efficiency and Improved Stability Enabled by an α -CsPbI₃/FAPbI₃ Bilayer Structure. *ACS Energy Lett.* **2019**, *4* (11), 2571–2578.
- (26) Zhang, X.; Lin, H.; Huang, H.; Reckmeier, C.; Zhang, Y.; Choy, W. C. H.; Rogach, A. L. Enhancing the Brightness of Cesium Lead Halide Perovskite Nanocrystal Based Green Light-Emitting Devices through the Interface Engineering with

Perfluorinated Ionomer. *Nano Lett.* **2016**, *16* (2), 1415–1420.

- (27) Song, J.; Li, J.; Li, X.; Xu, L.; Dong, Y.; Zeng, H. Quantum Dot Light-Emitting Diodes Based on Inorganic Perovskite Cesium Lead Halides (CsPbX₃). *Adv. Mater.* **2015**, *27* (44), 7162–7167.
- (28) Nedelcu, G.; Protesescu, L.; Yakunin, S.; Bodnarchuk, M. I.; Grotevent, M. J.; Kovalenko, M. V. Fast Anion-Exchange in Highly-Luminescent Nanocrystals of Cesium Lead Halide Perovskites (CsPbX₃, X = Cl, Br, I). *Nano Lett.* **2015**, *15* (8), 5635–5640.
- (29) Sheng, X.; Chen, G.; Wang, C.; Wang, W.; Hui, J.; Zhang, Q.; Yu, K.; Wei, W.; Yi, M.; Zhang, M.; Deng, Y.; Wang, P.; Xu, X.; Dai, Z.; Bao, J.; Wang, X. Polarized Optoelectronics of CsPbX₃ (X = Cl, Br, I) Perovskite Nanoplates with Tunable Size and Thickness. *Adv. Funct. Mater.* **2018**, *28* (19), 1–9.
- (30) Seth, S.; Samanta, A. A Facile Methodology for Engineering the Morphology of CsPbX₃ Perovskite Nanocrystals under Ambient Condition. *Sci. Rep.* **2016**, *6* (November), 1–7.
- (31) Li, Z. J.; Hofman, E.; Davis, A. H.; Maye, M. M.; Zheng, W. General Strategy for the Growth of CsPbX₃ (X = Cl, Br, I) Perovskite Nanosheets from the Assembly of Nanorods. *Chem. Mater.* **2018**, *30* (11), 3854–3860.
- (32) Tong, Y.; Bohn, B. J.; Bladt, E.; Wang, K.; Müller-Buschbaum, P.; Bals, S.; Urban, A. S.; Polavarapu, L.; Feldmann, J. From Precursor Powders to CsPbX₃ Perovskite Nanowires: One-Pot Synthesis, Growth Mechanism, and Oriented Self-Assembly. *Angew. Chemie - Int. Ed.* **2017**, *56* (44), 13887–13892.
- (33) Wang, S.; Yu, J.; Zhang, M.; Chen, D.; Li, C.; Chen, R.; Jia, G.; Rogach, A. L.; Yang, X. Stable, Strongly Emitting Cesium Lead Bromide Perovskite Nanorods with High Optical Gain Enabled by an Intermediate Monomer Reservoir Synthetic Strategy. *Nano Lett.* **2019**, *19* (9), 6315–6322.
- (34) Xiao, X.; Li, Y.; Xie, R. J. Blue-Emitting and Self-Assembled Thinner Perovskite CsPbBr₃ Nanoplates: Synthesis and Formation Mechanism. *Nanoscale* **2020**, *12* (16), 9231–9239.
- (35) Brennan, M. C.; Herr, J.; Nguyen-Beck, T. S.; Zinna, J.; Draguta, S.; Rouvimov, S.; Parkhill, J.; Kuno, M. Origin of the Size-Dependent Stokes Shift in CsPbBr₃

Perovskite Nanocrystals. *J. Am. Chem. Soc.* **2017**, jacs.7b05683.

- (36) Ruan, L.; Shen, W.; Wang, A.; Xiang, A.; Deng, Z. Alkyl-Thiol Ligand-Induced Shape- and Crystalline Phase-Controlled Synthesis of Stable Perovskite-Related CsPb₂Br₅ Nanocrystals at Room Temperature. *J. Phys. Chem. Lett.* **2017**, *8* (16), 3853–3860.
- (37) Brennan, M. C.; Forde, A.; Zhukovskyi, M.; Baublis, A. J.; Morozov, Y. V.; Zhang, S.; Zhang, Z.; Kilin, D. S.; Kuno, M. Universal Size-Dependent Stokes Shifts in Lead Halide Perovskite Nanocrystals. *J. Phys. Chem. Lett.* **2020**, *11* (13), 4937–4944.
- (38) Yang, R. X.; Tan, L. Z. Understanding Size Dependence of Phase Stability and Band Gap in CsPbI₃ Perovskite Nanocrystals. *J. Chem. Phys.* **2020**, *152* (3), 034702.
- (39) Zhao, Q.; Hazarika, A.; Schelhas, L. T.; Liu, J.; Gauding, E. A.; Li, G.; Zhang, M.; Toney, M. F.; Sercel, P. C.; Luther, J. M. Size-Dependent Lattice Structure and Confinement Properties in CsPbI₃ Perovskite Nanocrystals: Negative Surface Energy for Stabilization. *ACS Energy Lett.* **2020**, *5* (1), 238–247.
- (40) Du, J. S.; Shin, D.; Stanev, T. K.; Musumeci, C.; Xie, Z.; Huang, Z.; Lai, M.; Sun, L.; Zhou, W.; Stern, N. P.; Dravid, V. P.; Mirkin, C. A. Halide Perovskite Nanocrystal Arrays: Multiplexed Synthesis and Size-Dependent Emission. *Sci. Adv.* **2020**, *6* (39), 1–10.
- (41) Bimberg, D. Quantum Dots for Lasers, Amplifiers and Computing. *J. Phys. D. Appl. Phys.* **2005**, *38* (13), 2055–2058.
- (42) Gao, Y.; Shi, E.; Deng, S.; Shiring, S. B.; Snaider, J. M.; Liang, C.; Yuan, B.; Song, R.; Janke, S. M.; Liebman-Peláez, A.; Yoo, P.; Zeller, M.; Boudouris, B. W.; Liao, P.; Zhu, C.; Blum, V.; Yu, Y.; Savoie, B. M.; Huang, L.; Dou, L. Molecular Engineering of Organic–Inorganic Hybrid Perovskites Quantum Wells. *Nat. Chem.* **2019**, *11* (12), 1151–1157.
- (43) Wang, N.; Cheng, L.; Ge, R.; Zhang, S.; Miao, Y.; Zou, W.; Yi, C.; Sun, Y.; Cao, Y.; Yang, R.; Wei, Y.; Guo, Q.; Ke, Y.; Yu, M.; Jin, Y.; Liu, Y.; Ding, Q.; Di, D.; Yang, L.; Xing, G.; Tian, H.; Jin, C.; Gao, F.; Friend, R. H.; Wang, J.; Huang, W. Perovskite Light-Emitting Diodes Based on Solution-Processed Self-Organized Multiple Quantum Wells. *Nat. Photonics* **2016**, *10* (11), 699–704.

- (44) Ekimov, A. I.; Efros, A. L.; Onushchenko, A. A. Quantum Size Effect in Semiconductor Microcrystals. *Solid State Commun.* **1985**, *56* (11), 921–924.
- (45) Sichert, J. A.; Tong, Y.; Mutz, N.; Vollmer, M.; Fischer, S.; Milowska, K. Z.; García Cortadella, R.; Nickel, B.; Cardenas-Daw, C.; Stolarczyk, J. K.; Urban, A. S.; Feldmann, J. Quantum Size Effect in Organometal Halide Perovskite Nanoplatelets. *Nano Lett.* **2015**, *15* (10), 6521–6527.
- (46) Konstantatos, G.; Sargent, E. H. *Colloidal Quantum Dot Optoelectronics and Photovoltaics*; 2010.
- (47) Li, S.; Liu, G.; Liu, Q.; Nie, L.; Yao, G.; Zeng, F.; He, Y.; Xiang, W. Ultrastable Zero-Dimensional Cs₄PbBr₆ Perovskite Quantum Dot Glass. *ACS Sustain. Chem. Eng.* **2020**, *8* (29), 10646–10652.
- (48) Lee, K. J.; Turedi, B.; Sinatra, L.; Zhumekenov, A. A.; Maity, P.; Dursun, I.; Naphade, R.; Merdad, N.; Alsalloum, A.; Oh, S.; Wehbe, N.; Hedhili, M. N.; Kang, C. H.; Subedi, R. C.; Cho, N.; Kim, J. S.; Ooi, B. S.; Mohammed, O. F.; Bakr, O. M. Perovskite-Based Artificial Multiple Quantum Wells. *Nano Lett.* **2019**, *19* (6), 3535–3542.
- (49) Esaki, L.; Chang, L. L. New Transport Phenomenon in a Semiconductor “Superlattice.” *Phys. Rev. Lett.* **1974**, *33* (8), 495–498.
- (50) Bastard, G.; Mendez, E. E.; Chang, L. L.; Esaki, L. Exciton Binding Energy in Quantum Wells. *Phys. Rev. B* **1982**, *26* (4), 1974–1979.
- (51) Feldmann, J.; Peter, G.; Göbel, E. O.; Dawson, P.; Moore, K.; Foxon, C.; Elliott, R. J. Linewidth Dependence of Radiative Exciton Lifetimes in Quantum Wells. *Phys. Rev. Lett.* **1987**, *59* (20), 2337–2340.
- (52) Blancon, J. C.; Stier, A. V.; Tsai, H.; Nie, W.; Stoumpos, C. C.; Traoré, B.; Pedesseau, L.; Kepenekian, M.; Katsutani, F.; Noe, G. T.; Kono, J.; Tretiak, S.; Crooker, S. A.; Katan, C.; Kanatzidis, M. G.; Crochet, J. J.; Even, J.; Mohite, A. D. Scaling Law for Excitons in 2D Perovskite Quantum Wells. *Nat. Commun.* **2018**, *9* (1), 1–10.
- (53) Teunis, M. B.; Jana, A.; Dutta, P.; Johnson, M. A.; Mandal, M.; Muhoberac, B. B.; Sardar, R. Mesoscale Growth and Assembly of Bright Luminescent Organolead Halide Perovskite Quantum Wires. *Chem. Mater.* **2016**, *28* (14), 5043–5054.

- (54) Ma, C.; Shen, D.; Huang, B.; Li, X.; Chen, W. C.; Lo, M. F.; Wang, P.; Hon-Wah Lam, M.; Lu, Y.; Ma, B.; Lee, C. S. High Performance Low-Dimensional Perovskite Solar Cells Based on a One Dimensional Lead Iodide Perovskite. *J. Mater. Chem. A* **2019**, *7* (15), 8811–8817.
- (55) Nenon, D. P.; Pressler, K.; Kang, J.; Koscher, B. A.; Olshansky, J. H.; Osowiecki, W. T.; Koc, M. A.; Wang, L.-W.; Alivisatos, A. P. Design Principles for Trap-Free CsPbX₃ Nanocrystals: Enumerating and Eliminating Surface Halide Vacancies with Softer Lewis Bases. *J. Am. Chem. Soc.* **2018**, *140* (50), 17760–17772.
- (56) Kang, J.; Wang, L. W. High Defect Tolerance in Lead Halide Perovskite CsPbBr₃. *J. Phys. Chem. Lett.* **2017**, *8* (2), 489–493.
- (57) Guo, Y.; Wang, Q.; Saidi, W. A. Structural Stabilities and Electronic Properties of High-Angle Grain Boundaries in Perovskite Cesium Lead Halides. *J. Phys. Chem. C* **2017**, *121* (3), 1715–1722.
- (58) Yun, J. S.; Ho-Baillie, A.; Huang, S.; Woo, S. H.; Heo, Y.; Seidel, J.; Huang, F.; Cheng, Y. B.; Green, M. A. Benefit of Grain Boundaries in Organic-Inorganic Halide Planar Perovskite Solar Cells. *J. Phys. Chem. Lett.* **2015**, *6* (5), 875–880.
- (59) Li, J. J.; Ma, J. Y.; Ge, Q. Q.; Hu, J. S.; Wang, D.; Wan, L. J. Microscopic Investigation of Grain Boundaries in Organolead Halide Perovskite Solar Cells. *ACS Appl. Mater. Interfaces* **2015**, *7* (51), 28518–28523.
- (60) Ball, J. M.; Petrozza, A. Defects in Perovskite-Halides and Their Effects in Solar Cells. *Nat. Energy* **2016**, *1* (11).
- (61) Huang, H.; Bodnarchuk, M. I.; Kershaw, S. V.; Kovalenko, M. V.; Rogach, A. L. Lead Halide Perovskite Nanocrystals in the Research Spotlight: Stability and Defect Tolerance. *ACS Energy Lett.* **2017**, *2* (9), 2071–2083.
- (62) Brandt, R. E.; Stevanović, V.; Ginley, D. S.; Buonassisi, T. Identifying Defect-Tolerant Semiconductors with High Minority-Carrier Lifetimes: Beyond Hybrid Lead Halide Perovskites. *MRS Commun.* **2015**, *5* (2), 265–275.
- (63) Uddin, M. A.; Calabro, R. L.; Kim, D. Y.; Graham, K. R. Halide Exchange and Surface Modification of Metal Halide Perovskite Nanocrystals with Alkyltrichlorosilanes. *Nanoscale* **2018**, *10* (35), 16919–16927.

- (64) Guhrenz, C.; Benad, A.; Ziegler, C.; Haubold, D.; Gaponik, N.; Eychmüller, A. Solid-State Anion Exchange Reactions for Color Tuning of CsPbX₃ Perovskite Nanocrystals. *Chem. Mater.* **2016**, *28* (24), 9033–9040.
- (65) Abdel-Latif, K.; Epps, R. W.; Kerr, C. B.; Papa, C. M.; Castellano, F. N.; Abolhasani, M. Facile Room-Temperature Anion Exchange Reactions of Inorganic Perovskite Quantum Dots Enabled by a Modular Microfluidic Platform. *Adv. Funct. Mater.* **2019**, *29* (23), 1–13.
- (66) Li, G.; Ho, J. Y. L.; Wong, M.; Kwok, H. S. Reversible Anion Exchange Reaction in Solid Halide Perovskites and Its Implication in Photovoltaics. *J. Phys. Chem. C* **2015**, *119* (48), 26883–26888.
- (67) Zhang, T.; Li, G.; Chang, Y.; Wang, X.; Zhang, B.; Mou, H.; Jiang, Y. Full-Spectra Hyperfluorescence Cesium Lead Halide Perovskite Nanocrystals Obtained by Efficient Halogen Anion Exchange Using Zinc Halogenide Salts. *CrystEngComm* **2017**, *19* (8), 1165–1171.
- (68) Aldakov, D.; Lefrançois, A.; Reiss, P. Ternary and Quaternary Metal Chalcogenide Nanocrystals: Synthesis, Properties and Applications. *J. Mater. Chem. C* **2013**, *1* (24), 3756.
- (69) Ueng, H. Y.; Hwang, H. L. The Defect Structure of CuInS₂. Part I: Intrinsic Defects. *J. Phys. Chem. Solids* **1989**, *50* (12), 1297–1305.
- (70) De Trizio, L.; Prato, M.; Genovese, A.; Casu, A.; Povia, M.; Simonutti, R.; Alcocer, M. J. P.; D'Andrea, C.; Tassone, F.; Manna, L. Strongly Fluorescent Quaternary Cu-In-Zn-S Nanocrystals Prepared from Cu_{1-X}InS₂ Nanocrystals by Partial Cation Exchange. *Chem. Mater.* **2012**, *24* (12), 2400–2406.
- (71) Zhang, W.; Zhong, X. Facile Synthesis of ZnS-CuInS₂-Alloyed Nanocrystals for a Color-Tunable Fluorochrome and Photocatalyst. *Inorg. Chem.* **2011**, *50* (9), 4065–4072.
- (72) Protesescu, L.; Yakunin, S.; Bodnarchuk, M. I.; Bertolotti, F.; Masciocchi, N.; Guagliardi, A.; Kovalenko, M. V. Monodisperse Formamidinium Lead Bromide Nanocrystals with Bright and Stable Green Photoluminescence. *J. Am. Chem. Soc.* **2016**, *138* (43), 14202–14205.
- (73) Pan, A. A. A.; He, B.; Fan, X.; Liu, Z.; Urban, J. J.; Alivisatos, A. P.; He, L.; Liu,

- Y.; Paul, A. Insight into the Ligand-Mediated Synthesis of Colloidal Acid , Base and Cs Precursors. *ACS Nano* **2016**, *10* (8), 7943–7954.
- (74) Rainoì, G.; Nedelcu, G.; Protesescu, L.; Bodnarchuk, M. I.; Kovalenko, M. V.; Mahrt, R. F.; Stöferle, T. Single Cesium Lead Halide Perovskite Nanocrystals at Low Temperature: Fast Single-Photon Emission, Reduced Blinking, and Exciton Fine Structure. *ACS Nano* **2016**, *10* (2), 2485–2490.
- (75) Mizusaki, J.; Arai, K.; Fueki, K. Ionic Conduction of the Perovskite-Type Halides. *Solid State Ionics* **1983**, *11* (3), 203–211.
- (76) Azpiroz, J. M.; Mosconi, E.; Bisquert, J.; De Angelis, F. Defect Migration in Methylammonium Lead Iodide and Its Role in Perovskite Solar Cell Operation. *Energy Environ. Sci.* **2015**, *8* (7), 2118–2127.
- (77) Eames, C.; Frost, J. M.; Barnes, P. R. F.; O'Regan, B. C.; Walsh, A.; Islam, M. S. Ionic Transport in Hybrid Lead Iodide Perovskite Solar Cells. *Nat. Commun.* **2015**, *6* (May), 2–9.
- (78) Pan, A.; He, B.; Fan, X.; Liu, Z.; Urban, J. J.; Alivisatos, A. P.; He, L.; Liu, Y. Insight into the Ligand-Mediated Synthesis of Colloidal CsPbBr₃ Perovskite Nanocrystals: The Role of Organic Acid, Base, and Cesium Precursors. *ACS Nano* **2016**, *10* (8), 7943–7954.
- (79) Uddin, M. A.; Glover, J. D.; Park, S. M.; Pham, J. T.; Graham, K. R. Growth of Highly Stable and Luminescent CsPbX₃ (X = Cl, Br, and I) Nanoplates via Ligand Mediated Anion Exchange of CsPbCl₃ Nanocubes with AlX₃. *Chem. Mater.* **2020**, *32* (12), 5217–5225.
- (80) Ruan, L.; Shen, W.; Wang, A.; Zhou, Q.; Zhang, H.; Deng, Z. Stable and Conductive Lead Halide Perovskites Facilitated by X-Type Ligands. *Nanoscale* **2017**, *9* (21), 7252–7259.
- (81) Liu, Z.; Bekenstein, Y.; Ye, X.; Nguyen, S. C.; Swabeck, J.; Zhang, D.; Lee, S.-T.; Yang, P.; Ma, W.; Alivisatos, A. P. Ligand Mediated Transformation of Cesium Lead Bromide Perovskite Nanocrystals to Lead Depleted Cs₄PbBr₆ Nanocrystals. *J. Am. Chem. Soc.* **2017**, *139* (15), 5309–5312.
- (82) Park, S.; Cho, H.; Choi, W.; Zou, H.; Jeon, D. Y. Correlation of Near-Unity Quantum Yields with Photogenerated Excitons in X-Type Ligand Passivated

CsPbBr₃ Perovskite Quantum Dots. *Nanoscale Adv.* **2019**, *1* (8), 2828–2834.

- (83) Cao, J.; Yin, J.; Yuan, S.; Zhao, Y.; Li, J.; Zheng, N. Thiols as Interfacial Modifiers to Enhance the Performance and Stability of Perovskite Solar Cells. *Nanoscale* **2015**, *7* (21), 9443–9447.
- (84) Chang, C. Y.; Chang, Y. C.; Huang, W. K.; Liao, W. C.; Wang, H.; Yeh, C.; Tsai, B. C.; Huang, Y. C.; Tsao, C. S. Achieving High Efficiency and Improved Stability in Large-Area ITO-Free Perovskite Solar Cells with Thiol-Functionalized Self-Assembled Monolayers. *J. Mater. Chem. A* **2016**, *4* (20), 7903–7913.
- (85) Bi, D.; Li, X.; Milić, J. V.; Kubicki, D. J.; Pellet, N.; Luo, J.; LaGrange, T.; Mettraux, P.; Emsley, L.; Zakeeruddin, S. M.; Grätzel, M. Multifunctional Molecular Modulators for Perovskite Solar Cells with over 20% Efficiency and High Operational Stability. *Nat. Commun.* **2018**, *9* (1), 1–10.
- (86) Baek, S.; Kim, Y.; Kim, S. W. Highly Photo-Stable CsPbI₃ Perovskite Quantum Dots via Thiol Ligand Exchange and Their Polymer Film Application. *J. Ind. Eng. Chem.* **2020**, *83*, 279–284.
- (87) Torun, I.; Altintas, Y.; Yazici, A. F.; Mutlugun, E.; Onses, M. S. Solid-State Encapsulation and Color Tuning in Films of Cesium Lead Halide Perovskite Nanocrystals for White Light Generation. *ACS Appl. Nano Mater.* **2019**, *2* (3), 1185–1193.
- (88) Wang, J.; Xiang, X.; Yao, X.; Xiao, W. J.; Lin, J.; Li, W. S. Efficient Perovskite Solar Cells Using Trichlorosilanes as Perovskite/PCBM Interface Modifiers. *Org. Electron.* **2016**, *39*, 1–9.
- (89) Zhao, S.; Qin, M.; Xiang, Y.; Wang, H.; Xie, J.; Gong, L.; Chen, J.; Lu, X.; Song, J.; Qu, J.; Xu, J.; Yan, K. Bifunctional Effects of Trichloro(Octyl)Silane Modification on the Performance and Stability of a Perovskite Solar Cell via Microscopic Characterization Techniques. *ACS Appl. Energy Mater.* **2020**, *3* (4), 3302–3309.
- (90) Liu, Z.; Zhang, Y.; Fan, Y.; Chen, Z.; Tang, Z.; Zhao, J.; Lv, Y.; Lin, J.; Guo, X.; Zhang, J.; Liu, X. Toward Highly Luminescent and Stabilized Silica-Coated Perovskite Quantum Dots through Simply Mixing and Stirring under Room Temperature in Air. *ACS Appl. Mater. Interfaces* **2018**, *10* (15), 13053–13061.

- (91) Li, S.; Lei, D.; Ren, W.; Guo, X.; Wu, S.; Zhu, Y.; Rogach, A. L.; Chhowalla, M.; Jen, A. K. Y. Water-Resistant Perovskite Nanodots Enable Robust Two-Photon Lasing in Aqueous Environment. *Nat. Commun.* **2020**, *11* (1), 1–8.
- (92) Sun, C.; Zhang, Y.; Ruan, C.; Yin, C.; Wang, X.; Wang, Y.; Yu, W. W. Efficient and Stable White LEDs with Silica-Coated Inorganic Perovskite Quantum Dots. *Adv. Mater.* **2016**, *28* (45), 10088–10094.
- (93) Luo, B.; Pu, Y. C.; Lindley, S. A.; Yang, Y.; Lu, L.; Li, Y.; Li, X.; Zhang, J. Z. Organolead Halide Perovskite Nanocrystals: Branched Capping Ligands Control Crystal Size and Stability. *Angew. Chemie - Int. Ed.* **2016**, *55* (31), 8864–8868.
- (94) Brown, A. A. M.; Hooper, T. J. N.; Veldhuis, S. A.; Chin, X. Y.; Bruno, A.; Vashishtha, P.; Tey, J. N.; Jiang, L.; Damodaran, B.; Pu, S. H.; Mhaisalkar, S. G.; Mathews, N. Self-Assembly of a Robust Hydrogen-Bonded Octylphosphonate Network on Cesium Lead Bromide Perovskite Nanocrystals for Light-Emitting Diodes. *Nanoscale* **2019**, *11* (25), 12370–12380.
- (95) Tan, Y.; Zou, Y.; Wu, L.; Huang, Q.; Yang, D.; Chen, M.; Ban, M.; Wu, C.; Wu, T.; Bai, S.; Song, T.; Zhang, Q.; Sun, B. Highly Luminescent and Stable Perovskite Nanocrystals with Octylphosphonic Acid as a Ligand for Efficient Light-Emitting Diodes. *ACS Appl. Mater. Interfaces* **2018**, *10* (4), 3784–3792.
- (96) Paper, F.; Effects, L.; Xu, K.; Vickers, E. T.; Rao, L.; Lindley, S. A.; Luo, B.; Li, X.; Zhang, J. Z. Synergistic Surface Passivation of CH₃NH₃PbBr₃ Perovskite Quantum Dots with Phosphonic Acid and (3-Aminopropyl) Triethoxysilane. *Chem. Eur. J.* **2019**, *25* (19), 5014–5021.
- (97) Shamsi, J.; Kubicki, D.; Anaya, M.; Liu, Y.; Ji, K.; Frohna, K.; Grey, C. P.; Friend, R. H.; Stranks, S. D. Stable Hexylphosphonate-Capped Blue-Emitting Quantum-Confining CsPbBr₃ Nanoplatelets. *ACS Energy Lett.* **2020**, *5* (6), 1900–1907.
- (98) Zhang, B.; Goldoni, L.; Zito, J.; Dang, Z.; Almeida, G.; Zaccaria, F.; Wit, J. De; Infante, I.; Trizio, L. De; Manna, L. Alkyl Phosphonic Acids Deliver CsPbBr₃ Nanocrystals with High Photoluminescence Quantum Yield and Truncated Octahedron Shape. *Chem. Mater.* **2019**, *31* (21), 9140–9147.
- (99) Wang, H.; Zhang, X.; Wu, Q.; Cao, F.; Yang, D.; Shang, Y.; Ning, Z.; Zhang, W.; Zheng, W.; Yan, Y.; Kershaw, S. V.; Zhang, L.; Rogach, A. L.; Yang, X. Trifluoroacetate Induced Small-Grained CsPbBr₃ Perovskite Films Result in Efficient and Stable Light-Emitting Devices. *Nat. Commun.* **2019**, *10* (1), 665.

- (100) Alpert, M. R.; Niezgodna, J. S.; Chen, A. Z.; Foley, B. J.; Cuthriell, S.; Yoon, L. U.; Choi, J. J. Colloidal Nanocrystals as a Platform for Rapid Screening of Charge Trap Passivating Molecules for Metal Halide Perovskite Thin Films. *Chem. Mater.* **2018**, *30* (14), 4515–4526.
- (101) Liu, Y.; Li, D.; Zhang, L.; Chen, Y.; Geng, C.; Shi, S.; Zhang, Z.; Bi, W.; Xu, S. Amine- and Acid-Free Synthesis of Stable CsPbBr₃ Perovskite Nanocrystals. *Chem. Mater.* **2020**, *32* (5), 1904–1913.
- (102) Park, S. M.; Abtahi, A.; Boehm, A. M.; Graham, K. R. Surface Ligands for Methylammonium Lead Iodide Films: Surface Coverage, Energetics, and Photovoltaic Performance. *ACS Energy Lett.* **2020**, *5* (3), 799–806.
- (103) Boehm, A. M.; Liu, T.; Park, S. M.; Abtahi, A.; Graham, K. R. Influence of Surface Ligands on Energetics at FASnI₃/C60 Interfaces and Their Impact on Photovoltaic Performance. *ACS Appl. Mater. Interfaces* **2019**, *12* (5), 5209–5218.
- (104) Jancik Prochazkova, A.; Demchyshyn, S.; Yumusak, C.; Másilko, J.; Brüggemann, O.; Weiter, M.; Kaltenbrunner, M.; Sariciftci, N. S.; Krajcovic, J.; Salinas, Y.; Kovalenko, A. Proteinogenic Amino Acid Assisted Preparation of Highly Luminescent Hybrid Perovskite Nanoparticles. *ACS Appl. Nano Mater.* **2019**, *2* (7), 4267–4274.
- (105) Shynkarenko, Y.; Bodnarchuk, M. I.; Bernasconi, C.; Berezovska, Y.; Verteletskyi, V.; Ochsenbein, S. T.; Kovalenko, M. V. Direct Synthesis of Quaternary Alkylammonium-Capped Perovskite Nanocrystals for Efficient Blue and Green Light-Emitting Diodes. *ACS Energy Lett.* **2019**, *4* (11), 2703–2711.
- (106) Han, D.; Imran, M.; Zhang, M.; Chang, S.; Wu, X. G.; Zhang, X.; Tang, J.; Wang, M.; Ali, S.; Li, X.; Yu, G.; Han, J.; Wang, L.; Zou, B.; Zhong, H. Efficient Light-Emitting Diodes Based on in Situ Fabricated FAPbBr₃ Nanocrystals: The Enhancing Role of the Ligand-Assisted Reprecipitation Process. *ACS Nano* **2018**, *12* (8), 8808–8816.
- (107) Pan, J.; Quan, L. N.; Zhao, Y.; Peng, W.; Murali, B.; Sarmah, S. P.; Yuan, M.; Sinatra, L.; Alyami, N. M.; Liu, J.; Yassitepe, E.; Yang, Z.; Voznyy, O.; Comin, R.; Hedhili, M. N.; Mohammed, O. F.; Lu, Z. H.; Kim, D. H.; Sargent, E. H.; Bakr, O. M. Highly Efficient Perovskite-Quantum-Dot Light-Emitting Diodes by Surface Engineering. *Adv. Mater.* **2016**, *28* (39), 8718–8725.
- (108) Hoshi, K.; Chiba, T.; Sato, J.; Hayashi, Y.; Takahashi, Y.; Ebe, H.; Ohisa, S.; Kido,

- J. Purification of Perovskite Quantum Dots Using Low-Dielectric-Constant Washing Solvent “Diglyme” for Highly Efficient Light-Emitting Devices. *ACS Appl. Mater. Interfaces* **2018**, *10* (29), 24607–24612.
- (109) Chiba, T.; Hoshi, K.; Pu, Y. J.; Takeda, Y.; Hayashi, Y.; Ohisa, S.; Kawata, S.; Kido, J. High-Efficiency Perovskite Quantum-Dot Light-Emitting Devices by Effective Washing Process and Interfacial Energy Level Alignment. *ACS Appl. Mater. Interfaces* **2017**, *9* (21), 18054–18060.
- (110) Park, J. H.; Lee, A. Y.; Yu, J. C.; Nam, Y. S.; Choi, Y.; Park, J.; Song, M. H. Surface Ligand Engineering for Efficient Perovskite Nanocrystal-Based Light-Emitting Diodes. *ACS Appl. Mater. Interfaces* **2019**, *11* (8), 8428–8435.
- (111) Moyon, E.; Jun, H.; Kim, H.; Jang, J. Surface Engineering of Room Temperature-Grown Inorganic Perovskite Quantum Dots for Highly Efficient Inverted Light-Emitting Diodes. *ACS Appl. Mater. Interfaces* **2018**, *10* (49), 42647–42656.
- (112) Perovskite, H.; Shin, Y. S.; Yoon, Y. J.; Lee, K. T.; Jeong, J.; Park, S. Y.; Kim, G.; Kim, J. Y. Vivid and Fully Saturated Blue Light-Emitting Diodes Based on Ligand-Modified Halide Perovskite Nanocrystals. *ACS Appl. Mater. Interfaces* **2019**, *11* (26), 23401–23409.
- (113) Shin, Y. S.; Yoon, Y. J.; Lee, K. T.; Lee, W.; Kim, H. S.; Kim, J. W.; Jang, H.; Kim, M.; Kim, D. S.; Kim, G. H.; Kim, J. Y. High-Performance Perovskite Light-Emitting Diodes with Surface Passivation of CsPbBr₃-x Nanocrystals via Antisolvent-Triggered Ion-Exchange. *ACS Appl. Mater. Interfaces* **2020**, *12* (28), 31582–31590.
- (114) Ahmed, T.; Seth, S.; Samanta, A. Boosting the Photoluminescence of CsPbX₃ (X = Cl, Br, I) Perovskite Nanocrystals Covering a Wide Wavelength Range by Postsynthetic Treatment with Tetrafluoroborate Salts. *Chem. Mater.* **2018**, *30* (11), 3633–3637.
- (115) Whiteman, A.; Esparrago, J.; Elsayed, S.; Rueda, S.; Arkhipova, I. *Renewable Capacity Statistics*; 2019.
- (116) Schmela, M. Global Market Outlook for Solar Power: 2019-2023. *Sol. Power Eur.* **2019**, 92.
- (117) Lee, M. M.; Teuscher, J.; Miyasaka, T.; Murakami, T. N.; Snaith, H. J. Efficient Hybrid Solar Cells Based on Meso-Superstructured Organometal Halide

Perovskites. *Science* (80-.). **2012**, 338 (6107), 643–647.

- (118) NREL. Best Research-Cell Efficiency Chart, <https://www.nrel.gov/pv/cell-efficiency.html>. NREL. 2019, p accessed 05 May 2020.
- (119) Pang, S.; Hu, H.; Zhang, J.; Lv, S.; Yu, Y.; Wei, F.; Qin, T.; Xu, H.; Liu, Z.; Cui, G. NH₂CH=NH₂PbI₃: An Alternative Organolead Iodide Perovskite Sensitizer for Mesoscopic Solar Cells. *Chem. Mater.* **2014**, 26 (3), 1485–1491.
- (120) Stoumpos, C. C.; Malliakas, C. D.; Kanatzidis, M. G. Semiconducting Tin and Lead Iodide Perovskites with Organic Cations: Phase Transitions, High Mobilities, and near-Infrared Photoluminescent Properties. *Inorg. Chem.* **2013**, 52 (15), 9019–9038.
- (121) Koh, T. M.; Fu, K.; Fang, Y.; Chen, S.; Sum, T. C.; Mathews, N. Formamidinium-Containing Metal-Halide: An Alternative Material for Near-IR Absorption Perovskite Solar Cells. *J. Phys. Chem. C* **2014**, 118 (30), 16458–16462.
- (122) Vega, E.; Mollar, M.; Marí, B. Bandgap Tuning of MAPbI₃-XBr_x Thin Film Perovskites for Photovoltaic Applications. *Renew. Sustain. Energy Conf. (IRSEC), 2015 3rd Int. IEEE* **2015**, 1–5.
- (123) Saliba, M.; Correa-Baena, J. P.; Wolff, C. M.; Stolterfoht, M.; Phung, N.; Albrecht, S.; Neher, D.; Abate, A. How to Make over 20% Efficient Perovskite Solar Cells in Regular (n-i-p) and Inverted (p-i-n) Architectures. *Chem. Mater.* **2018**, 30 (13), 4193–4201.
- (124) Stolterfoht, M.; Caprioglio, P.; Wolff, C. M.; Márquez, J. A.; Nordmann, J.; Zhang, S.; Rothhardt, D.; Hörmann, U.; Amir, Y.; Redinger, A.; Kegelmann, L.; Zu, F.; Albrecht, S.; Koch, N.; Kirchartz, T.; Saliba, M.; Unold, T.; Neher, D. The Impact of Energy Alignment and Interfacial Recombination on the Internal and External Open-Circuit Voltage of Perovskite Solar Cells. *Energy Environ. Sci.* **2019**, 12 (9), 2778–2788.
- (125) Schulz, P.; Cahen, D.; Kahn, A. Halide Perovskites: Is It All about the Interfaces? *Chem. Rev.* **2019**, 119 (5), 3349–3417.
- (126) Yang, J. M.; Luo, Y.; Bao, Q.; Li, Y. Q.; Tang, J. X. Recent Advances in Energetics and Stability of Metal Halide Perovskites for Optoelectronic Applications. *Adv. Mater. Interfaces* **2019**, 6 (3), 1–25.

- (127) Olthof, S. Research Update: The Electronic Structure of Hybrid Perovskite Layers and Their Energetic Alignment in Devices. *APL Mater.* **2016**, *4* (9).
- (128) Correa Baena, J. P.; Steier, L.; Tress, W.; Saliba, M.; Neutzner, S.; Matsui, T.; Giordano, F.; Jacobsson, T. J.; Srimath Kandada, A. R.; Zakeeruddin, S. M.; Petrozza, A.; Abate, A.; Nazeeruddin, M. K.; Grätzel, M.; Hagfeldt, A. Highly Efficient Planar Perovskite Solar Cells through Band Alignment Engineering. *Energy Environ. Sci.* **2015**, *8* (10), 2928–2934.
- (129) Oliveti, G.; Marletta, L.; Arcuri, N.; De Simone, M.; Bruno, R.; Evola, G. Solar Energy. *Delft Univ. Technol.* **2014**, 101–112.
- (130) Swarnkar, A.; Chulliyil, R.; Ravi, V. K.; Irfanullah, M.; Chowdhury, A.; Nag, A. Colloidal CsPbBr₃ Perovskite Nanocrystals: Luminescence beyond Traditional Quantum Dots. *Angew. Chemie* **2015**, *127* (51), 15644–15648.
- (131) Huang, S.; Li, Z.; Kong, L.; Zhu, N.; Shan, A.; Li, L. Enhancing the Stability of CH₃NH₃PbBr₃ Quantum Dots by Embedding in Silica Spheres Derived from Tetramethyl Orthosilicate in “Waterless” Toluene. *J. Am. Chem. Soc.* **2016**, *138* (18), 5749–5752.
- (132) Liu, M.; Johnston, M. B.; Snaith, H. J. Efficient Planar Heterojunction Perovskite Solar Cells by Vapour Deposition. *Nature* **2013**, *501* (7467), 395–398.
- (133) Jeon, N. J.; Noh, J. H.; Yang, W. S.; Kim, Y. C.; Ryu, S.; Seo, J.; Seok, S. Il. Compositional Engineering of Perovskite Materials for High-Performance Solar Cells. *Nature* **2015**, *517* (7535), 476–480.
- (134) Kulbak, M.; Gupta, S.; Kedem, N.; Levine, I.; Bendikov, T.; Hodes, G.; Cahen, D. Cesium Enhances Long-Term Stability of Lead Bromide Perovskite-Based Solar Cells. *J. Phys. Chem. Lett.* **2016**, *7* (1), 167–172.
- (135) Akkerman, Q. A.; Gandini, M.; Stasio, F. Di; Rastogi, P.; Palazon, F.; Bertoni, G.; Ball, J. M.; Prato, M.; Petrozza, A. Strongly Emissive Perovskite Nanocrystal Inks for High-Voltage Solar Cells. *Nat. Energy* **2016**, *2* (2), 16194.
- (136) Wang, J.; Wang, N.; Jin, Y.; Si, J.; Tan, Z. K.; Du, H.; Cheng, L.; Dai, X.; Bai, S.; He, H.; Ye, Z.; Lai, M. L.; Friend, R. H.; Huang, W. Interfacial Control toward Efficient and Low-Voltage Perovskite Light-Emitting Diodes. *Adv. Mater.* **2015**, *27* (14), 2311–2316.

- (137) Zhang, L.; Yang, X.; Jiang, Q.; Wang, P.; Yin, Z.; Zhang, X.; Tan, H.; Yang, Y. M.; Wei, M.; Sutherland, B. R.; Sargent, E. H.; You, J. Ultra-Bright and Highly Efficient Inorganic Based Perovskite Light-Emitting Diodes. *Nat. Commun.* **2017**, *8*, 1–8.
- (138) Xu, Y.; Chen, Q.; Zhang, C.; Wang, R.; Wu, H.; Zhang, X.; Xing, G.; Yu, W. W.; Wang, X.; Zhang, Y.; Xiao, M. Two-Photon-Pumped Perovskite Semiconductor Nanocrystal Lasers. *J. Am. Chem. Soc.* **2016**, *138* (11), 3761–3768.
- (139) Fu, Y.; Zhu, H.; Stoumpos, C. C.; Ding, Q.; Wang, J.; Kanatzidis, M. G.; Zhu, X.; Jin, S. Broad Wavelength Tunable Robust Lasing from Single-Crystal Nanowires of Cesium Lead Halide Perovskites (CsPbX₃, X = Cl, Br, I). *ACS Nano* **2016**, *10* (8), 7963–7972.
- (140) Deschler, F.; Price, M.; Pathak, S.; Klintberg, L. E.; Jarausch, D. D.; Hügler, R.; Hüttner, S.; Leijtens, T.; Stranks, S. D.; Snaith, H. J.; Atatüre, M.; Phillips, R. T.; Friend, R. H. High Photoluminescence Efficiency and Optically Pumped Lasing in Solution-Processed Mixed Halide Perovskite Semiconductors. *J. Phys. Chem. Lett.* **2014**, *5* (8), 1421–1426.
- (141) Dou, L.; Yang, Y. M.; You, J.; Hong, Z.; Chang, W. H.; Li, G.; Yang, Y. Solution-Processed Hybrid Perovskite Photodetectors with High Detectivity. *Nat. Commun.* **2014**, *5*, 1–6.
- (142) Ramasamy, P.; Lim, D.-H.; Kim, B.; Lee, S.-H.; Lee, M.-S.; Lee, J.-S. All-Inorganic Cesium Lead Halide Perovskite Nanocrystals for Photodetector Applications. *Chem. Commun.* **2016**, *52* (10), 2067–2070.
- (143) Sutherland, B. R.; Johnston, A. K.; Ip, A. H.; Xu, J.; Adinolfi, V.; Kanjanaboos, P.; Sargent, E. H. Sensitive, Fast, and Stable Perovskite Photodetectors Exploiting Interface Engineering. *ACS Photonics* **2015**, *2* (8), 1117–1123.
- (144) Dong, R.; Fang, Y.; Chae, J.; Dai, J.; Xiao, Z.; Dong, Q.; Yuan, Y.; Centrone, A.; Zeng, X. C.; Huang, J. High-Gain and Low-Driving-Voltage Photodetectors Based on Organolead Triiodide Perovskites. *Adv. Mater.* **2015**, *27* (11), 1912–1918.
- (145) Li, M.; Zhang, X.; Lu, S.; Yang, P. Phase Transformation, Morphology Control, and Luminescence Evolution of Cesium Lead Halide Nanocrystals in the Anion Exchange Process. *RSC Adv.* **2016**, *6* (105), 103382–103389.
- (146) Akkerman, Q. A.; D’Innocenzo, V.; Accornero, S.; Scarpellini, A.; Petrozza, A.;

- Prato, M.; Manna, L. Tuning the Optical Properties of Cesium Lead Halide Perovskite Nanocrystals by Anion Exchange Reactions. *J. Am. Chem. Soc.* **2015**, *137* (32), 10276–10281.
- (147) Parobek, D.; Dong, Y.; Qiao, T.; Rossi, D.; Son, D. H. Photoinduced Anion Exchange in Cesium Lead Halide Perovskite Nanocrystals. *J. Am. Chem. Soc.* **2017**, *139* (12), 4358–4361.
- (148) Shirayama, M.; Kato, M.; Miyadera, T.; Sugita, T.; Fujiseki, T.; Hara, S.; Kadowaki, H.; Murata, D.; Chikamatsu, M.; Fujiwara, H. Degradation Mechanism of CH₃NH₃PbI₃ Perovskite Materials upon Exposure to Humid Air. *J. Appl. Phys.* **2016**, *119* (11), 115501.
- (149) Yang, J.; Siempelkamp, B. D.; Liu, D.; Kelly, T. L. Investigation of CH₃NH₃PbI₃ Degradation Rates and Mechanisms in Controlled Humidity Environments Using in Situ Techniques. *ACS Nano* **2015**, *9* (2), 1955–1963.
- (150) Zhang, L.; Ju, M.-G.; Liang, W. The Effect of Moisture on the Structures and Properties of Lead Halide Perovskites: A First-Principles Theoretical Investigation. *Phys. Chem. Chem. Phys.* **2016**, *18* (33), 23174–23183.
- (151) Niu, G.; Guo, X.; Wang, L. Review of Recent Progress in Chemical Stability of Perovskite Solar Cells. *J. Mater. Chem. A* **2015**, *3* (17), 8970–8980.
- (152) Wang, S.; Jiang, Y.; Juarez-Perez, E. J.; Ono, L. K.; Qi, Y. Accelerated Degradation of Methylammonium Lead Iodide Perovskites Induced by Exposure to Iodine Vapour. *Nat. Energy* **2017**, *2* (1), 2009–2014.
- (153) Luo, B.; Pu, Y. C.; Lindley, S. A.; Yang, Y.; Lu, L.; Li, Y.; Li, X.; Zhang, J. Z. Organolead Halide Perovskite Nanocrystals: Branched Capping Ligands Control Crystal Size and Stability. *Angew. Chemie - Int. Ed.* **2016**, *55* (31), 8864–8868.
- (154) Meyns, M.; Perálvarez, M.; Heuer-Jungemann, A.; Hertog, W.; Ibáñez, M.; Nafria, R.; Genç, A.; Arbiol, J.; Kovalenko, M. V.; Carreras, J.; Cabot, A.; Kanaras, A. G. Polymer-Enhanced Stability of Inorganic Perovskite Nanocrystals and Their Application in Color Conversion LEDs. *ACS Appl. Mater. Interfaces* **2016**, *8* (30), 19579–19586.
- (155) Huang, H.; Chen, B.; Wang, Z.; Hung, T. F.; Susha, A. S.; Zhong, H.; Rogach, A. L. Water Resistant CsPbX₃ Nanocrystals Coated with Polyhedral Oligomeric

Silsesquioxane and Their Use as Solid State Luminophores in All-Perovskite White Light-Emitting Devices. *Chem. Sci.* **2016**, 7 (9), 5699–5703.

- (156) Cattley, C. A.; Stavrinadis, A.; Beal, R.; Moghal, J.; Cook, A. G.; Grant, P. S.; Smith, J. M.; Assender, H.; Watt, A. A. R. Colloidal Synthesis of Lead Oxide Nanocrystals for Photovoltaics. *Chem. Commun.* **2010**, 46 (16), 2802.
- (157) Gonzalez-Carrero, S.; Francés-Soriano, L.; González-Béjar, M.; Agouram, S.; Galian, R. E.; Pérez-Prieto, J. The Luminescence of CH₃NH₃PbBr₃ Perovskite Nanoparticles Crests the Summit and Their Photostability under Wet Conditions Is Enhanced. *Small* **2016**, No. 38, 5245–5250.
- (158) Pohanish, R. P. *Sittig's Handbook of Toxic and Hazardous Chemicals and Carcinogens*, 6th ed.; Elsevier Inc.: 225 Wyman Street, Waltham, MA 02451, USA, 2012.
- (159) Nedelcu, G.; Protesescu, L.; Yakunin, S.; Bodnarchuk, M. I.; Grotevent, M. J.; Kovalenko, M. V. Fast Anion-Exchange in Highly Luminescent Nanocrystals of Cesium Lead Halide Perovskites (CsPbX₃, X = Cl, Br, I). *Nano Lett.* **2015**, 15 (8), 5635–5640.
- (160) Kim, Y.; Yassitepe, E.; Voznyy, O.; Comin, R.; Walters, G.; Gong, X.; Kanjanaboos, P.; Nogueira, A. F.; Sargent, E. H. Efficient Luminescence from Perovskite Quantum Dot Solids. *ACS Appl. Mater. Interfaces* **2015**, 7 (45), 25007–25013.
- (161) Cao, W.; Liu, P.; Chen, W.; Wang, W.; Xu, B.; Wu, D.; Hao, J.; Cao, W.; Fang, F.; Li, Y.; Zeng, Y.; Pan, R.; Chen, S.; Sun, X. W.; Wang, K. Halide-Rich Synthesized Cesium Lead Bromide Perovskite Nanocrystals for Light-Emitting Diodes with Improved Performance. *Chem. Mater.* **2017**, 29 (12), 5168–5173.
- (162) Rossi, D.; Parobek, D.; Dong, Y.; Son, D. H. Dynamics of Exciton-Mn Energy Transfer in Mn-Doped CsPbCl₃ Perovskite Nanocrystals. *J. Phys. Chem. C* **2017**, 121 (32), 17143–17149.
- (163) Das Adhikari, S.; Dutta, S. K.; Dutta, A.; Guria, A. K.; Pradhan, N. Chemically Tailoring the Dopant Emission in Manganese-Doped CsPbCl₃ Perovskite Nanocrystals. *Angew. Chemie - Int. Ed.* **2017**, 56 (30), 8746–8750.
- (164) Parobek, D.; Roman, B. J.; Dong, Y.; Jin, H.; Lee, E.; Sheldon, M.; Son, D. H.

Exciton-to-Dopant Energy Transfer in Mn-Doped Cesium Lead Halide Perovskite Nanocrystals. *Nano Lett.* **2016**, *16* (12), 7376–7380.

- (165) Hu, F.; Zhang, H.; Sun, C.; Yin, C.; Lv, B.; Zhang, C.; Yu, W. W.; Wang, X.; Zhang, Y.; Xiao, M. Superior Optical Properties of Perovskite Nanocrystals as Single Photon Emitters. *ACS Nano* **2015**, *9* (12), 12410–12416.
- (166) Li, X.; Wu, Y.; Zhang, S.; Cai, B.; Gu, Y.; Song, J.; Zeng, H. CsPbX₃ Quantum Dots for Lighting and Displays: Room-temperature Synthesis, Photoluminescence Superiorities, Underlying Origins and White Light-Emitting Diodes. *Adv. Funct. Mater.* **2016**, *26* (15), 2435–2445.
- (167) Han, Q.; Wu, W.; Liu, W.; Yang, Y. The Peak Shift and Evolution of Upconversion Luminescence from CsPbBr₃ Nanocrystals under Femtosecond Laser Excitation. *RSC Adv.* **2017**, *7* (57), 35757–35764.
- (168) Wang, Y.; Zhi, M.; Chan, Y. Delayed Exciton Formation Involving Energetically Shallow Trap States in Colloidal CsPbBr₃ Quantum Dots. *J. Phys. Chem. C* **2017**, *121* (51), 28498–28505.
- (169) Guo, B.; Tay, S. W.; Liu, Z.; Hong, L. Embedding of Hollow Polymer Microspheres with Hydrophilic Shell in Nafion Matrix as Proton and Water Micro-Reservoir. *Polymers (Basel)*. **2012**, *4* (3), 1499–1516.
- (170) Gardelis, S.; Nassiopoulou, A. G.; Mahdouani, M.; Bourguiga, R.; Jaziri, S. Enhancement and Red Shift of Photoluminescence (PL) of Fresh Porous Si under Prolonged Laser Irradiation or Ageing: Role of Surface Vibration Modes. *Phys. E Low-Dimensional Syst. Nanostructures* **2009**, *41* (6), 986–989.
- (171) Rajput, D.; Costa, L.; Terekhov, A.; Lansford, K.; Hofmeister, W. Silica Coating of Polymer Nanowires Produced via Nanoimprint Lithography from Femtosecond Laser Machined Templates. *Nanotechnology* **2012**, *23* (10).
- (172) Wang, Y.; Li, X.; Song, J.; Xiao, L.; Zeng, H.; Sun, H. All-Inorganic Colloidal Perovskite Quantum Dots: A New Class of Lasing Materials with Favorable Characteristics. *Adv. Mater.* **2015**, *27* (44), 7101–7108.
- (173) Di Stasio, F.; Christodoulou, S.; Huo, N.; Konstantatos, G. Near-Unity Photoluminescence Quantum Yield in CsPbBr₃ Nanocrystal Solid-State Films via Postsynthesis Treatment with Lead Bromide. *Chem. Mater.* **2017**, *29* (18), 7663–

7667.

- (174) Correa-Baena, J.-P.; Abate, A.; Saliba, M.; Tress, W.; Jesper Jacobsson, T.; Grätzel, M.; Hagfeldt, A. The Rapid Evolution of Highly Efficient Perovskite Solar Cells. *Energy Environ. Sci.* **2017**, *10* (3), 710–727.
- (175) Park, S. M.; Mazza, S. M.; Liang, Z.; Abtahi, A.; Boehm, A. M.; Parkin, S. R.; Anthony, J. E.; Graham, K. R. Processing Dependent Influence of the Hole Transport Layer Ionization Energy on Methylammonium Lead Iodide Perovskite Photovoltaics. *ACS Appl. Mater. Interfaces* **2018**, *10* (18), 15548–15557.
- (176) Li, Y.; Shi, Z. F.; Li, S.; Lei, L. Z.; Ji, H. F.; Wu, D.; Xu, T. T.; Tian, Y. T.; Li, X. J. High-Performance Perovskite Photodetectors Based on Solution-Processed All-Inorganic CsPbBr₃ Thin Films. *J. Mater. Chem. C* **2017**, *5* (33), 8355–8360.
- (177) Amgar, D.; Aharon, S.; Etgar, L. Inorganic and Hybrid Organo-Metal Perovskite Nanostructures: Synthesis, Properties, and Applications. *Adv. Funct. Mater.* **2016**, *26* (47), 8576–8593.
- (178) Li, X.; Wu, Y.; Zhang, S.; Cai, B.; Gu, Y.; Song, J.; Zeng, H. CsPbX₃ Quantum Dots for Lighting and Displays: Room-Temperature Synthesis, Photoluminescence Superiorities, Underlying Origins and White Light-Emitting Diodes. *Adv. Funct. Mater.* **2016**, *26* (15), 2435–2445.
- (179) Burgt, J. S. Van Der; Geuchies, J. J.; Meer, B. Van Der; Zanaga, D.; Zhang, Y.; Albrecht, W.; Andrei, V. Cuboidal Supraparticles Self-Assembled from Cubic CsPbBr₃ Perovskite Nanocrystals. *J. Phys. Chem. C* **2018**, *122* (27), 15706–15712.
- (180) Shi, H.; Du, M. H. Shallow Halogen Vacancies in Halide Optoelectronic Materials. *Phys. Rev. B* **2014**, *90* (17), 1–6.
- (181) Imran, M.; Caligiuri, V.; Wang, M.; Goldoni, L.; Prato, M.; Krahne, R.; De Trizio, L.; Manna, L. Benzoyl Halides as Alternative Precursors for the Colloidal Synthesis of Lead-Based Halide Perovskite Nanocrystals. *J. Am. Chem. Soc.* **2018**, *140* (7), 2656–2664.
- (182) Wei, S.; Yang, Y.; Kang, X.; Wang, L.; Huang, L.; Pan, D. Room-Temperature and Gram-Scale Synthesis of CsPbX₃ (X = Cl, Br, I) Perovskite Nanocrystals with 50–85% Photoluminescence Quantum Yields. *Chem. Commun.* **2016**, *52* (45), 7265–7268.

- (183) Zhu, J.; Zhu, Y.; Huang, J.; Gong, Y.; Shen, J.; Li, C. Synthesis of CsPbBr₃ Perovskite Nanocrystals with the Sole Ligand of Protonated (3-Aminopropyl)Triethoxysilane. *J. Mater. Chem. C* **2019**, xx (xx), xxx–xxx.
- (184) Alpert, M. R.; Niezgoda, J. S.; Chen, A. Z.; Foley, B. J.; Cuthriell, S.; Yoon, L. U.; Choi, J. J. Colloidal Nanocrystals as a Platform for Rapid Screening of Charge Trap Passivating Molecules for Metal Halide Perovskite Thin Films. *Chem. Mater.* **2018**, 30 (14), 4515–4526.
- (185) González-Pedro, V.; Veldhuis, S. A.; Begum, R.; Bañuls, M. J.; Bruno, A.; Mathews, N.; Mhaisalkar, S.; Maquieira, Á. Recovery of Shallow Charge-Trapping Defects in CsPbX₃ Nanocrystals through Specific Binding and Encapsulation with Amino-Functionalized Silanes. *ACS Energy Lett.* **2018**, 3 (6), 1409–1414.
- (186) Pan, J.; Quan, L. N.; Zhao, Y.; Peng, W.; Murali, B.; Sarmah, S. P.; Yuan, M.; Sinatra, L.; Alyami, N. M.; Liu, J.; Yassitepe, E.; Yang, Z.; Voznyy, O.; Comin, R.; Hedhili, M. N.; Mohammed, O. F.; Lu, Z. H.; Kim, D. H.; Sargent, E. H.; Bakr, O. M. Highly Efficient Perovskite-Quantum-Dot Light-Emitting Diodes by Surface Engineering. *Adv. Mater.* **2016**, 28 (39), 8718–8725.
- (187) Begum, R.; Parida, M. R.; Abdelhady, A. L.; Murali, B.; Alyami, N. M.; Ahmed, G. H.; Hedhili, M. N.; Bakr, O. M.; Mohammed, O. F. Engineering Interfacial Charge Transfer in CsPbBr₃ Perovskite Nanocrystals by Heterovalent Doping. *J. Am. Chem. Soc.* **2017**, 139 (2), 731–737.
- (188) Yu, Y.; Zhang, D.; Kisielowski, C.; Dou, L.; Kornienko, N.; Bekenstein, Y.; Wong, A. B.; Alivisatos, A. P.; Yang, P. Atomic Resolution Imaging of Halide Perovskites. *Nano Lett.* **2016**, 16 (12), 7530–7535.
- (189) Wu, W.-B.; Wong, Y.-C.; Tan, Z.-K.; Wu, J. Photo-Induced Thiol Coupling and C–H Activation Using Nanocrystalline Lead-Halide Perovskite Catalysts. *Catal. Sci. Technol.* **2018**, 8 (16), 4257–4263.
- (190) Hoyle, C. E.; Bowman, C. N. Thiol-Ene Click Chemistry. *Angew. Chemie Int. Ed.* **2010**, 49 (9), 1540–1573.
- (191) Zhang, M.; Li, H.; Jing, Q.; Lu, Z.; Wang, P. Atomic Characterization of Byproduct Nanoparticles on Cesium Lead Halide Nanocrystals Using High-Resolution Scanning Transmission Electron Microscopy. *Crystals* **2017**, 8 (1), 2.

- (192) Zhao, J.; Liu, M.; Fang, L.; Jiang, S.; Zhou, J.; Ding, H.; Huang, H.; Wen, W.; Luo, Z.; Zhang, Q.; Wang, X.; Gao, C. Great Disparity in Photoluminescence Quantum Yields of Colloidal CsPbBr₃ Nanocrystals with Varied Shape: The Effect of Crystal Lattice Strain. *J. Phys. Chem. Lett.* **2017**, *8* (13), 3115–3121.
- (193) Dang, Z.; Shamsi, J.; Palazon, F.; Imran, M.; Akkerman, Q. A.; Park, S.; Bertoni, G.; Prato, M.; Brescia, R.; Manna, L. In Situ Transmission Electron Microscopy Study of Electron Beam-Induced Transformations in Colloidal Cesium Lead Halide Perovskite Nanocrystals. *ACS Nano* **2017**, *11* (2), 2124–2132.
- (194) Shkrob, I. A.; Marin, T. W. Charge Trapping in Photovoltaically Active Perovskites and Related Halogenoplumbate Compounds. *J. Phys. Chem. Lett.* **2014**, *5* (7), 1066–1071.
- (195) Society, R.; Sciences, P. The Photodecomposition of Lead Iodide. *Proc. R. Soc. Lond. A. Math. Phys. Sci.* **2017**, *193* (1032), 1–24.
- (196) Steirer, K. X.; Schulz, P.; Teeter, G.; Stevanovic, V.; Yang, M.; Zhu, K.; Berry, J. J. Defect Tolerance in Methylammonium Lead Triiodide Perovskite. *ACS Energy Lett.* **2016**, *1* (2), 360–366.
- (197) Alberti, A.; Deretzis, I.; Pellegrino, G.; Bongiorno, C.; Smecca, E.; Mannino, G.; Giannazzo, F.; Condorelli, G. G.; Sakai, N.; Miyasaka, T.; Spinella, C.; La Magna, A. Similar Structural Dynamics for the Degradation of CH₃NH₃PbI₃ in Air and in Vacuum. *ChemPhysChem* **2015**, *16* (14), 3064–3071.
- (198) Kerner, R. A.; Schloemer, T. H.; Schulz, P.; Berry, J. J.; Schwartz, J.; Sellinger, A.; Rand, B. P. Amine Additive Reactions Induced by the Soft Lewis Acidity of Pb²⁺ in Halide Perovskites. Part II: Impacts of Amido Pb Impurities in Methylammonium Lead Triiodide Thin Films. *J. Mater. Chem. C* **2018**, *7* (18), 5244–5250.
- (199) Zu, F. S.; Amsalem, P.; Salzmann, I.; Wang, R. Bin; Ralaiarisoa, M.; Kowarik, S.; Duhm, S.; Koch, N. Impact of White Light Illumination on the Electronic and Chemical Structures of Mixed Halide and Single Crystal Perovskites. *Adv. Opt. Mater.* **2017**, *5* (9), 1700139.
- (200) Wu, Y.; Chen, Q.; Takeguchi, M.; Furuya, K. High-Resolution Transmission Electron Microscopy Study on the Anomalous Structure of Lead Nanoparticles with UHV-MBE-TEM System. *Surf. Sci.* **2000**, *462* (1), 203–210.

- (201) Udayabhaskararao, T.; Kazes, M.; Houben, L.; Lin, H.; Oron, D. Nucleation, Growth, and Structural Transformations of Perovskite Nanocrystals. *Chem. Mater.* **2017**, *29* (3), 1302–1308.
- (202) Ravi, V. K.; Santra, P. K.; Joshi, N.; Chugh, J.; Singh, S. K.; Rensmo, H.; Ghosh, P.; Nag, A. Origin of the Substitution Mechanism for the Binding of Organic Ligands on the Surface of CsPbBr₃ Perovskite Nanocubes. *J. Phys. Chem. Lett.* **2017**, *8* (20), 4988–4994.
- (203) Jiang, D.; Wang, G.; Zheng, F.; Han, J.; Wu, X. Novel Thermo-Sensitive Hydrogels Containing Polythioether Dendrons: Facile Tuning of LCSTs, Strong Absorption of Ag Ions, and Embedment of Smaller Ag Nanocrystals. *Polym. Chem.* **2015**, *6* (4), 625–632.
- (204) Zhao, Q.; Hazarika, A.; Chen, X.; Harvey, S. P.; Larson, B. W.; Teeter, G. R.; Liu, J.; Song, T.; Xiao, C.; Shaw, L.; Zhang, M.; Li, G.; Beard, M. C.; Luther, J. M. High Efficiency Perovskite Quantum Dot Solar Cells with Charge Separating Heterostructure. *Nat. Commun.* **2019**, *10* (1), 2842.
- (205) Creutz, S. E.; Crites, E. N.; De Siena, M. C.; Gamelin, D. R. Anion Exchange in Cesium Lead Halide Perovskite Nanocrystals and Thin Films Using Trimethylsilyl Halide Reagents. *Chem. Mater.* **2018**, *30* (15), 4887–4891.
- (206) Yong, Z. J.; Guo, S. Q.; Ma, J. P.; Zhang, J. Y.; Li, Z. Y.; Chen, Y. M.; Zhang, B. Bin; Zhou, Y.; Shu, J.; Gu, J. L.; Zheng, L. R.; Bakr, O. M.; Sun, H. T. Doping-Enhanced Short-Range Order of Perovskite Nanocrystals for Near-Unity Violet Luminescence Quantum Yield. *J. Am. Chem. Soc.* **2018**, *140* (31), 9942–9951.
- (207) Qi, Z.; Fu, X.; Yang, T.; Li, D.; Fan, P.; Li, H.; Jiang, F.; Li, L.; Luo, Z.; Zhuang, X.; Pan, A. Highly Stable Lead-Free Cs₃Bi₂I₉ Perovskite Nanoplates for Photodetection Applications. *Nano Res.* **2019**, *12* (1), 1–6.
- (208) Liang, D.; Peng, Y.; Fu, Y.; Shearer, M. J.; Zhang, J.; Zhai, J.; Zhang, Y.; Hamers, R. J.; Andrew, T. L.; Jin, S. Color-Pure Violet-Light-Emitting Diodes Based on Layered Lead Halide Perovskite Nanoplates. *ACS Nano* **2016**, *10* (7), 6897–6904.
- (209) Yang, D.; Zou, Y.; Li, P.; Liu, Q.; Wu, L.; Hu, H.; Xu, Y.; Sun, B.; Zhang, Q.; Lee, S. T. Large-Scale Synthesis of Ultrathin Cesium Lead Bromide Perovskite Nanoplates with Precisely Tunable Dimensions and Their Application in Blue Light-Emitting Diodes. *Nano Energy* **2018**, *47* (January), 235–242.

- (210) Hu, X.; Zhou, H.; Jiang, Z.; Wang, X.; Yuan, S.; Lan, J.; Fu, Y.; Zhang, X.; Zheng, W.; Wang, X.; Zhu, X.; Liao, L.; Xu, G.; Jin, S.; Pan, A. Direct Vapor Growth of Perovskite CsPbBr₃ Nanoplate Electroluminescence Devices. *ACS Nano* **2017**, *11* (10), 9869–9876.
- (211) Si, J.; Liu, Y.; He, Z.; Du, H.; Du, K.; Chen, D.; Li, J.; Xu, M.; Tian, H.; He, H.; Di, D.; Lin, C.; Cheng, Y.; Wang, J.; Jin, Y. Efficient and High-Color-Purity Light-Emitting Diodes Based on in Situ Grown Films of CsPbX₃ (X = Br, I) Nanoplates with Controlled Thicknesses. *ACS Nano* **2017**, *11* (11), 11100–11107.
- (212) Schlaus, A. P.; Spencer, M. S.; Miyata, K.; Liu, F.; Wang, X.; Datta, I.; Lipson, M.; Pan, A.; Zhu, X. Y. How Lasing Happens in CsPbBr₃ Perovskite Nanowires. *Nat. Commun.* **2019**, *10* (1), 1–8.
- (213) Weidman, M. C.; Goodman, A. J.; Tisdale, W. A. Colloidal Halide Perovskite Nanoplatelets: An Exciting New Class of Semiconductor Nanomaterials. *Chem. Mater.* **2017**, *29* (12), 5019–5030.
- (214) Shamsi, J.; Dang, Z.; Bianchini, P.; Canale, C.; Stasio, F. Di; Brescia, R.; Prato, M.; Manna, L. Colloidal Synthesis of Quantum Confined Single Crystal CsPbBr₃ Nanosheets with Lateral Size Control up to the Micrometer Range. *J. Am. Chem. Soc.* **2016**, *138* (23), 7240–7243.
- (215) Bekenstein, Y.; Koscher, B. A.; Eaton, S. W.; Yang, P.; Alivisatos, A. P. Highly Luminescent Colloidal Nanoplates of Perovskite Cesium Lead Halide and Their Oriented Assemblies. *J. Am. Chem. Soc.* **2015**, *137* (51), 16008–16011.
- (216) Pan, Q.; Hu, H.; Zou, Y.; Chen, M.; Wu, L.; Yang, D.; Yuan, X.; Fan, J.; Sun, B.; Zhang, Q. Microwave-Assisted Synthesis of High-Quality “All-Inorganic” CsPbX₃ (X = Cl, Br, I) Perovskite Nanocrystals and Their Application in Light Emitting Diodes. *J. Mater. Chem. C* **2017**, *5* (42), 10947–10954.
- (217) Chen, D.; Chen, X.; Li, J.; Li, X.; Zhong, J. Ultrathin CsPbX₃ (X = Cl, Br, I) Nanoplatelets: Solvothermal Synthesis and Optical Spectroscopic Properties. *Dalt. Trans.* **2018**, *47* (29), 9845–9849.
- (218) Akkerman, Q. A.; Motti, S. G.; Srimath Kandada, A. R.; Mosconi, E.; D’Innocenzo, V.; Bertoni, G.; Marras, S.; Kamino, B. A.; Miranda, L.; De Angelis, F.; Petrozza, A.; Prato, M.; Manna, L. Solution Synthesis Approach to Colloidal Cesium Lead Halide Perovskite Nanoplatelets with Monolayer-Level Thickness Control. *J. Am. Chem. Soc.* **2016**, *138* (3), 1010–1016.

- (219) Liang, Z.; Zhao, S.; Xu, Z.; Qiao, B.; Song, P.; Gao, D.; Xu, X. Shape-Controlled Synthesis of All-Inorganic CsPbBr₃ Perovskite Nanocrystals with Bright Blue Emission. *ACS Appl. Mater. Interfaces* **2016**, *8* (42), 28824–28830.
- (220) Bohn, B. J.; Tong, Y.; Gramlich, M.; Lai, M. L.; Döblinger, M.; Wang, K.; Hoye, R. L. Z.; Müller-Buschbaum, P.; Stranks, S. D.; Urban, A. S.; Polavarapu, L.; Feldmann, J. Boosting Tunable Blue Luminescence of Halide Perovskite Nanoplatelets through Postsynthetic Surface Trap Repair. *Nano Lett.* **2018**, *18* (8), 5231–5238.
- (221) Bertolotti, F.; Nedelcu, G.; Vivani, A.; Cervellino, A.; Masciocchi, N.; Guagliardi, A.; Kovalenko, M. V. Crystal Structure, Morphology and Surface Termination of Cyan-Emissive, 6-Monolayers-Thick CsPbBr₃ Nanoplatelets from X-Ray Total Scattering. *ACS Nano* **2019**, *13* (12), 14294–14307.
- (222) Chakrabarty, A.; Satija, S.; Gangwar, U.; Sapra, S. Precursor-Mediated Synthesis of Shape-Controlled Colloidal CsPbBr₃ Perovskite Nanocrystals and Their Nanofiber-Directed Self-Assembly. *Chem. Mater.* **2020**, *32* (2), 721–733.
- (223) Coughlin, J. P. Heats of Formation and Hydration of Anhydrous Aluminum Chloride. *J. Phys. Chem.* **1958**, *62* (4), 419–421.
- (224) Dong, X.; Acheampong Tsiwah, E.; Li, T.; Hu, J.; Li, Z.; Ding, Y.; Deng, Z.; Chen, W.; Xu, L.; Gao, P.; Zhao, X.; Xie, Y. Trivalent Ion Mediated Abnormal Growth of All-Inorganic Perovskite Nanocrystals and Their Divergent Emission Properties. *Nanoscale* **2019**, *11* (16), 7903–7912.
- (225) Liu, M.; Zhong, G.; Yin, Y.; Miao, J.; Li, K.; Wang, C.; Xu, X.; Shen, C.; Meng, H. Aluminum-Doped Cesium Lead Bromide Perovskite Nanocrystals with Stable Blue Photoluminescence Used for Display Backlight. *Adv. Sci.* **2017**, *4* (11), 1–8.
- (226) Nagaoka, Y.; Hills-Kimball, K.; Tan, R.; Li, R.; Wang, Z.; Chen, O. Nanocube Superlattices of Cesium Lead Bromide Perovskites and Pressure-Induced Phase Transformations at Atomic and Mesoscale Levels. *Adv. Mater.* **2017**, *29* (18), 1606666.
- (227) Wang, Z.; Schliehe, C.; Wang, T.; Nagaoka, Y.; Cao, Y. C.; Bassett, W. A.; Wu, H.; Fan, H.; Weller, H. Deviatoric Stress Driven Formation of Large Single-Crystal PbS Nanosheet from Nanoparticles and in Situ Monitoring of Oriented Attachment. *J. Am. Chem. Soc.* **2011**, *133* (37), 14484–14487.

- (228) Yun, S.; Kirakosyan, A.; Yoon, S. G.; Choi, J. Scalable Synthesis of Exfoliated Organometal Halide Perovskite Nanocrystals by Ligand-Assisted Ball Milling. *ACS Sustain. Chem. Eng.* **2018**, *6* (3), 3733–3738.
- (229) Hintermayr, V. A.; Richter, A. F.; Ehrat, F.; Döblinger, M.; Vanderlinden, W.; Sichert, J. A.; Tong, Y.; Polavarapu, L.; Feldmann, J.; Urban, A. S. Tuning the Optical Properties of Perovskite Nanoplatelets through Composition and Thickness by Ligand-Assisted Exfoliation. *Adv. Mater.* **2016**, *28* (43), 9478–9485.
- (230) Myneni, S. C. B.; Traina, S. J.; Waychunas, G. A.; Logan, T. J. Vibrational Spectroscopy of Functional Group Chemistry and Arsenate Coordination in Ettringite. *Geochim. Cosmochim. Acta* **1998**, *62* (21–22), 3499–3514.
- (231) Su, C.; Suarez, D. L. In Situ Infrared Speciation of Adsorbed Carbonate on Aluminium and Iron Oxides. *Clays Clay Miner.* **1997**, *45* (6), 814–825.
- (232) Xie, M.; Liu, H.; Chun, F.; Deng, W.; Luo, C.; Zhu, Z.; Yang, M. Aqueous Phase Exfoliating Quasi-2D CsPbBr₃ Nanosheets with Ultrahigh Intrinsic Water Stability. *Small* **2019**, *15* (34), 1901994.
- (233) Akkerman, Q. A.; Motti, S. G.; Srimath Kandada, A. R.; Mosconi, E.; D’Innocenzo, V.; Bertoni, G.; Marras, S.; Kamino, B. A.; Miranda, L.; De Angelis, F.; Petrozza, A.; Prato, M.; Manna, L. Solution Synthesis Approach to Colloidal Cesium Lead Halide Perovskite Nanoplatelets with Monolayer-Level Thickness Control. *J. Am. Chem. Soc.* **2016**, *138* (3), 1010–1016.
- (234) Noh, J. H.; Im, S. H.; Heo, J. H.; Mandal, T. N.; Seok, S. II. Chemical Management for Colorful, Efficient, and Stable Inorganic-Organic Hybrid Nanostructured Solar Cells. *Nano Lett.* **2013**, *13* (4), 1764–1769.
- (235) Yang, J.; Siempelkamp, B. D.; Liu, D.; Kelly, T. L. Investigation of CH₃NH₃PbI₃ Degradation Rates and Mechanisms in Controlled Humidity Environments Using in Situ Techniques. *ACS Nano* **2015**, *9* (2), 1955–1963.
- (236) Misra, R. K.; Aharon, S.; Li, B.; Mogilyansky, D.; Visoly-Fisher, I.; Etgar, L.; Katz, E. A. Temperature- and Component-Dependent Degradation of Perovskite Photovoltaic Materials under Concentrated Sunlight. *J. Phys. Chem. Lett.* **2015**, *6* (3), 326–330.
- (237) Conings, B.; Drijkoningen, J.; Gauquelin, N.; Babayigit, A.; D’Haen, J.;

- D'Olieslaeger, L.; Ethirajan, A.; Verbeeck, J.; Manca, J.; Mosconi, E.; De Angelis, F.; Boyen, H. G. Intrinsic Thermal Instability of Methylammonium Lead Trihalide Perovskite. *Adv. Energy Mater.* **2015**, 5 (15), 1–8.
- (238) Pellet, N.; Gao, P.; Gregori, G.; Yang, T.; Nazeeruddin, M. K.; Maier, J.; Grätzel, M. Mixed-Organic-Cation Perovskite Photovoltaics for Enhanced Solar- Light Harvesting ** *Angewandte. Angew. Chemie - Int. Ed.* **2014**, 53 (12), 3151–3157.
- (239) Mcmeehin, D. P.; Sadoughi, G.; Rehman, W.; Eperon, G. E.; Saliba, M.; Hörantner, M. T.; Haghighirad, A.; Sakai, N.; Korte, L.; Rech, B.; Johnston, M. B.; Herz, L. M.; Snaith, H. J. A Mixed-Cation Lead Mixed-Halide Perovskite Absorber for Tandem Solar Cells. *Science (80-.)*. **2016**, 351 (6269), 151–156.
- (240) Gra, C.; Zakeeruddin, S. M.; Ro, U.; Gra, M. Entropic Stabilization of Mixed A-Cation ABX₃ Metal Halide Perovskites for High Performance Perovskite Solar Cells. *Energy Environ. Sci.* **2016**, 9 (2), 656–662.
- (241) Liu, T.; Zong, Y.; Zhou, Y.; Yang, M.; Li, Z.; Game, O. S.; Zhu, K.; Zhu, R.; Gong, Q.; Padture, N. P. High-Performance Formamidinium-Based Perovskite Solar Cells via Microstructure-Mediated δ - to - α Phase Transformation. *Chem. Mater.* **2017**, 29 (7), 3246–3250.
- (242) Lee, J.; Kim, D.; Kim, H.; Seo, S.; Cho, S. M.; Park, N. Formamidinium and Cesium Hybridization for Photo- and Moisture-Stable Perovskite Solar Cell. *Adv. Energy Mater.* **2015**, 5 (20), 1501310.
- (243) Saliba, M.; Matsui, T.; Seo, J. Y.; Domanski, K.; Correa-Baena, J. P.; Nazeeruddin, M. K.; Zakeeruddin, S. M.; Tress, W.; Abate, A.; Hagfeldt, A.; Grätzel, M. Cesium-Containing Triple Cation Perovskite Solar Cells: Improved Stability, Reproducibility and High Efficiency. *Energy Environ. Sci.* **2016**, 9 (6), 1989–1997.
- (244) Eperon, G. E.; Stranks, S. D.; Menelaou, C.; Johnston, M. B.; Herz, L. M.; Snaith, H. J. Formamidinium Lead Trihalide: A Broadly Tunable Perovskite for Efficient Planar Heterojunction Solar Cells. *Energy Environ. Sci.* **2014**, 7 (3), 982–988.
- (245) Jiang, Y.; Leyden, M. R.; Qiu, L.; Wang, S.; Ono, L. K.; Wu, Z.; Juarez-Perez, E. J.; Qi, Y. Combination of Hybrid CVD and Cation Exchange for Upscaling Cs-Substituted Mixed Cation Perovskite Solar Cells with High Efficiency and Stability. *Adv. Funct. Mater.* **2018**, 28 (1), 1703835.

- (246) Zhou, Y.; Jia, Y.; Fang, H.; Loi, M. A.; Xie, F. Composition-Tuned Wide Bandgap Perovskites : From Grain Engineering to Stability and Performance Improvement. *Adv. Funct. Mater.* **2018**, *28* (35), 1803130.
- (247) Luo, L.; Zhang, Y.; Chai, N.; Deng, X.; Zhong, J.; Huang, F.; Peng, Y.; Ku, Z.; Cheng, Y. B. Large-Area Perovskite Solar Cells with Cs_xFA_{1-x}PbI₃-yBr_y Thin Films Deposited by a Vapor-Solid Reaction Method. *J. Mater. Chem. A* **2018**, *6* (42), 21143–21148.
- (248) Yu, Y.; Wang, C.; Grice, C. R.; Shrestha, N.; Chen, J.; Zhao, D.; Liao, W.; Cimaroli, A. J.; Roland, P. J.; Ellingson, R. J.; Yan, Y. Improving the Performance of Formamidinium and Cesium Lead Triiodide Perovskite Solar Cells Using Lead Thiocyanate Additives. *ChemSusChem* **2016**, *9* (23), 3288–3297.
- (249) Huang, J.; Xu, P.; Liu, J.; You, X. Sequential Introduction of Cations Deriving Large-Grain Cs_xFA_{1-x}PbI₃ Thin Film for Planar Hybrid Solar Cells : Insight into Phase-Segregation and Thermal-Healing Behavior. *Small* **2017**, *13* (10), 1603225.
- (250) Luo, P.; Zhou, S.; Zhou, Y.; Xia, W.; Sun, L.; Cheng, J.; Xu, C.; Lu, Y. Fabrication of Cs_xFA_{1-x}PbI₃ Mixed-Cation Perovskites via Gas-Phase-Assisted Compositional Modulation for Efficient and Stable Photovoltaic Devices. *ACS Appl. Mater. Interfaces* **2017**, *9* (49), 42708–42716.
- (251) Seo, J.; Matsui, T.; Luo, J.; Giordano, F.; Saliba, M.; Schenk, K.; Ummadisingu, A.; Domanski, K.; Hadadian, M.; Hagfeldt, A.; Zakeeruddin, S. M.; Steiner, U.; Grätzel, M.; Abate, A. Ionic Liquid Control Crystal Growth to Enhance Planar Perovskite Solar Cells Efficiency. *Adv. Energy Mater.* **2016**, *6* (20), 1600767.
- (252) Ali, N.; Liang, C.; Ji, C.; Zhang, H.; Sun, M.; Li, D.; You, F.; He, Z. Enlarging Crystal Grains with Ionic Liquid to Enhance the Performance of Perovskite Solar Cells. *Org. Electron.* **2020**, 105805.
- (253) Chao, L.; Niu, T.; Gu, H.; Yang, Y.; Wei, Q.; Xia, Y.; Hui, W.; Zuo, S.; Zhu, Z.; Pei, C.; Li, X.; Zhang, J.; Fang, J.; Xing, G.; Li, H.; Huang, X.; Gao, X.; Ran, C.; Song, L.; Fu, L.; Chen, Y.; Huang, W. Origin of High Efficiency and Long-Term Stability in Ionic Liquid Perovskite Photovoltaic. *Research* **2020**, *2020*, 1–13.
- (254) Luo, C.; Li, G.; Chen, L.; Dong, J.; Yu, M.; Xu, C.; Yao, Y.; Wang, M.; Song, Q.; Zhang, S. Passivation of Defects in Inverted Perovskite Solar Cells Using an Imidazolium-Based Ionic Liquid. *Sustain. Energy Fuels* **2020**, *4* (8), 3971–3978.

- (255) Li, M.; Zhao, C.; Wang, Z. K.; Zhang, C. C.; Lee, H. K. H.; Pockett, A.; Barbé, J.; Tsoi, W. C.; Yang, Y. G.; Carnie, M. J.; Gao, X. Y.; Yang, W. X.; Durrant, J. R.; Liao, L. S.; Jain, S. M. Interface Modification by Ionic Liquid: A Promising Candidate for Indoor Light Harvesting and Stability Improvement of Planar Perovskite Solar Cells. *Adv. Energy Mater.* **2018**, *8* (24), 1–8.
- (256) Wang, H.; Wang, Z.; Yang, Z.; Xu, Y.; Ding, Y.; Tan, L.; Yi, C.; Zhang, Z.; Meng, K.; Chen, G.; Zhao, Y.; Luo, Y.; Zhang, X.; Hagfeldt, A.; Luo, J. Ligand-Modulated Excess PbI₂ Nanosheets for Highly Efficient and Stable Perovskite Solar Cells. *Adv. Mater.* **2020**, *32* (21), 1–8.
- (257) Wu, Z.; Jiang, M.; Liu, Z.; Jamshaid, A.; Ono, L. K.; Qi, Y. Highly Efficient Perovskite Solar Cells Enabled by Multiple Ligand Passivation. *Adv. Energy Mater.* **2020**, *10* (10), 1–5.
- (258) Wei, F.; Jiao, B.; Dong, H.; Xu, J.; Lei, T.; Zhang, J.; Yu, Y.; Ma, L.; Wang, D.; Chen, J.; Hou, X.; Wu, Z. Bifunctional π -Conjugated Ligand Assisted Stable and Efficient Perovskite Solar Cell Fabrication: Via Interfacial Stitching. *J. Mater. Chem. A* **2019**, *7* (27), 16533–16540.
- (259) Wu, W. Q.; Rudd, P. N.; Ni, Z.; Van Brackle, C. H.; Wei, H.; Wang, Q.; Ecker, B. R.; Gao, Y.; Huang, J. Reducing Surface Halide Deficiency for Efficient and Stable Iodide-Based Perovskite Solar Cells. *J. Am. Chem. Soc.* **2020**, *142* (8), 3989–3996.
- (260) Zheng, X.; Hou, Y.; Bao, C.; Yin, J.; Yuan, F.; Huang, Z.; Song, K.; Liu, J.; Troughton, J.; Gasparini, N.; Zhou, C.; Lin, Y.; Xue, D.-J.; Chen, B.; Johnston, A. K.; Wei, N.; Hedhili, M. N.; Wei, M.; Alsalloum, A. Y.; Maity, P.; Turedi, B.; Yang, C.; Baran, D.; Anthopoulos, T. D.; Han, Y.; Lu, Z.-H.; Mohammed, O. F.; Gao, F.; Sargent, E. H.; Bakr, O. M. Managing Grains and Interfaces via Ligand Anchoring Enables 22.3%-Efficiency Inverted Perovskite Solar Cells. *Nat. Energy* **2020**, *5* (2), 131–140.
- (261) Chen, J.; Kim, S. G.; Ren, X.; Jung, H. S.; Park, N. G. Effect of Bidentate and Tridentate Additives on the Photovoltaic Performance and Stability of Perovskite Solar Cells. *J. Mater. Chem. A* **2019**, *7* (9), 4977–4987.
- (262) Bai, S.; Da, P.; Li, C.; Wang, Z.; Yuan, Z.; Fu, F.; Kawecki, M.; Liu, X.; Sakai, N.; Wang, J. T.; Huettner, S.; Buecheler, S.; Fahlman, M.; Gao, F.; Snaith, H. J. Planar Perovskite Solar Cells with Long-Term Stability Using Ionic Liquid Additives. *Nature* **2019**, *571* (7764), 245–250.

- (263) Xie, F.; Chen, C. C.; Wu, Y.; Li, X.; Cai, M.; Liu, X.; Yang, X.; Han, L. Vertical Recrystallization for Highly Efficient and Stable Formamidinium-Based Inverted-Structure Perovskite Solar Cells. *Energy Environ. Sci.* **2017**, *10* (9), 1942–1949.
- (264) Bi, D.; Tress, W.; Dar, M. I.; Gao, P.; Luo, J.; Renevier, C.; Schenk, K.; Abate, A.; Giordano, F.; Baena, J. C.; Decoppet, J.; Zakeeruddin, S. M.; Nazeeruddin, M. K.; Grätzel, M.; Hagfeldt, A. Efficient Luminescent Solar Cells Based on Tailored Mixed-Cation Perovskites. *Sci. Adv.* **2016**, *2* (1), e1501170.
- (265) Cao, D. H.; Stoumpos, C. C.; Malliakas, C. D.; Katz, M. J.; Farha, O. K.; Hupp, J. T.; Kanatzidis, M. G. Remnant PbI₂, an Unforeseen Necessity in High-Efficiency Hybrid Perovskite-Based Solar Cells? *APL Mater.* **2014**, *2* (9), 091101.
- (266) Roman, M. *Selenium: Properties and Determination*, 1st ed.; Elsevier Ltd., 2015.

VITA

Md Aslam Uddin

EDUCATION	YEAR
MS in Physical Chemistry (2012), University of Dhaka (DU), Dhaka, Bangladesh	2010-2012

BS in Chemistry (2010), University of Dhaka (DU), Dhaka, Bangladesh	2005-2010
---	-----------

APPOINTMENTS	YEAR
Graduate Assistant, University of Kentucky, USA	2015-2020
Senior Chemistry Teacher, Bangladesh International Tutorial (BIT), Dhaka, Bangladesh	2012-2015

PEER-REVIEWED PUBLICATIONS	YEAR
7. Joy, S. R.; Uddin, M. A. ; et al. <i>Fabricating Transparent Electrodes Using Inkjet-printed Metal Nanowire/Polymer Composite for Perovskite Photovoltaics.</i>	Expecting in 2021
6. Liu, T.*; Uddin, M. A.* ; et al. <i>A Review Based on Performance of Metal-halide Perovskite-based Devices.</i>	Expecting in 2021
5. Park, S. M.; Uddin, M. A. ; et al. <i>Designing Surface Ligands to Form Surface Segregated Monolayers.</i>	Expecting in 2021
4. Uddin, M.A. ; et al. <i>Enhancing Durability of Mixed Inorganic-organic Based Perovskite ($Cs_{0.15}FA_{0.85}PbI_3$) Photovoltaics by Application of Surface Ligands.</i>	Expecting in 2021
3. Uddin, M. A. ; Glover, J. D.; Park, S. M.; Pham, J. T.; Graham, K. R. <i>Growth of Highly Stable and Luminescent $CsPbX_3$ ($X = Cl, Br, \text{ and } I$) Nanoplates via Ligand Mediated Anion Exchange of $CsPbCl_3$ Nanocubes with AlX_3. <i>Chem. Mater.</i> 2020, 32, 12, 5217–5225. https://doi.org/10.1021/acs.chemmater.0c01325.</i>	2020
2. Uddin, M. A. ; Mobley, J. K.; Masud, A. Al; Liu, T.; Calabro, R. L.; Kim, D.-Y.; Richards, C. I.; Graham, K. R. <i>Mechanistic Exploration of Dodecanethiol-Treated Colloidal $CsPbBr_3$ Nanocrystals with Photoluminescence Quantum Yields Reaching Near 100%. <i>J. Phys. Chem. C</i> 2019, 123 (29), 18103–18112. https://doi.org/10.1021/acs.jpcc.9b05612.</i>	2019
1. Uddin, M. A. ; Calabro, R. L.; Kim, D. Y.; Graham, K. R. <i>Halide exchange and surface modification of metal halide perovskite nanocrystals</i>	2018

with alkyltrichlorosilanes. Nanoscale **2018**, *10* (35), 16919–16927.
<https://doi.org/10.1039/c8nr04763d>.

HONORS & AWARDS	YEAR
Nominee of Dean's Competitive Fellowships (<i>UK</i>)	2018
Outstanding Oral Qualifier Award (<i>UK</i>)	2017
Chair's Scholarship (<i>UK</i>)	2015
Selected Lecturer of Chemistry (<i>NTRCA, BD</i>)	2010